

# Impact of Gallium on the Defect Landscape of Sulfur-Based Chalcopyrite Solar Cells

Von der Fakultät für Mathematik und Naturwissenschaften der  
Carl von Ossietzky Universität Oldenburg zur Erlangung des Grades  
und Titels eines

Doktors der Naturwissenschaften (Dr. rer. nat.)

angenommene

## Dissertation

von Frau Dipl.-Phys. Julia Riediger  
geboren am 2. April 1983  
in Papenburg (Deutschland)

Gutachter: Prof. Dr. Jürgen Parisi

Zweitgutachterin: Prof. Dr. Małgorzata Igalson

Tag der Disputation: 12.08.2013

# Zusammenfassung

Aufgrund ihrer nah am Schockley-Queisser Optimum gelegenen Bandlücke von 1.5 eV stellen Solarzellen basierend auf Cu(In,Ga)S<sub>2</sub> eine vielversprechende Alternative zu Cu(In,Ga)Se<sub>2</sub> Solarzellen dar. Allerdings liegt an der Grenzfläche zwischen CdS und Schwefel-basierten Absorberschichten ein negativer Leitungsband-Offset vor. Durch diesen werden Rekombinationsverluste über Grenzflächendefekte begünstigt, welche die Leerlaufspannung ( $V_{oc}$ ) dieser Solarzellen limitieren. Erhöhte  $V_{oc}$ -Werte können durch Dotierung des Absorbers mit Ga erzielt werden, was eine Aufweitung der Bandlücke zur Folge hat. Von Selen-basierten Absorbieren ist bekannt, dass Ga maßgeblich die energetische Position des Leitungsbandminimums anhebt. Hingegen weiß man bisher wenig über den Einfluss von Ga auf die Energiebänder in Schwefel-basierten Materialien. In dieser Arbeit werden Cu(In,Ga)S<sub>2</sub> Solarzellen mit unterschiedlichen Ga-Konzentrationen nahe der Puffer/Absorber Grenzfläche mit Hinblick auf den Einfluss von Ga auf Solarzellenparameter und Defekteigenschaften untersucht. Absorberschichten mit verschiedenen Ga-Tiefenprofilen wurden durch variierte Temperaturen und Haltezeiten während der Sulfurisierung der metallischen Cu:Ga/In Vorläuferschichten realisiert. Als integrale Messgröße der Ga-Konzentration an der Grenzfläche wird die minimale Bandlücke  $E_{g,min}$  herangezogen, welche anhand von Spektren der externen Quanteneffizienz ( $EQE$ ) bestimmt wird. Ein linearer Anstieg mit  $E_{g,min}$  wurde sowohl für die Aktivierungsenergie  $E_A$  der Sättigungsstromdichte als auch für die Aktivierungsenergie  $E_a$  eines mit thermischer Admittanz Spektroskopie (TAS) ermittelten tiefen Volumendefekts im Absorber festgestellt. Darüber hinaus wurden mit TAS Defekte in Ga-freien und Ga-dotierten Proben nachgewiesen, welche den in Se-basierten Solarzellen auftretenden Signaturen N1 und N2 zugeordnet werden können. Da N1 von mehreren Wissenschaftlern mit einem Grenzflächendefekt in Zusammenhang gebracht wurde, könnte dieser Defekt in den Schwefel-basierten Solarzellen aufgrund ihrer  $V_{oc}$ -Limitierung durch Grenzflächendefekte eine wichtige Rolle spielen. In der Literatur wurden Ergebnisse unterschiedlicher Untersuchungen gezeigt, welche die Interpretation von N1 als Grenzflächendefekt befürworten. Diese Versuche umfassten Kapazitäts-Spannungs-Messungen bei verschiedenen Frequenzen und Experimente, bei denen die Proben in Umgebungsluft geheizt wurden. Letztere verfolgten das Ziel, die Passivierung von Grenzflächendefekten mit Sauerstoff nachzuweisen. Im Rahmen dieser Arbeit konnte durch Anwendung analoger Methoden auf eine Auswahl an Solarzellen mit CuInS<sub>2</sub> und Cu(In,Ga)S<sub>2</sub> Absorbieren für eine Signatur einer Ga-freien Probe ein Zusammenhang mit N1 nachgewiesen werden. Da diese Signatur mit einem Grenzflächendefekt assoziiert werden kann, könnte dieser Defekt zu Rekombinationsmechanismen an der Grenzfläche beitragen und somit für das auffällig niedrige  $V_{oc}$  in diesen Proben verantwortlich sein.

## Abstract

Wide band gap  $\text{CuInS}_2$  solar cells are an attractive alternative to devices based on  $\text{Cu}(\text{In,Ga})\text{Se}_2$  due to their absorber band gap of 1.5 eV which is close to the Shockley-Queisser optimum [1]. However, a negative conduction band offset at the heterojunction between CdS and sulfur-based absorber films promotes recombination losses via interface defect states which in consequence limits the  $V_{oc}$ . An increase of the  $V_{oc}$  can be achieved by widening the interface band gap via Ga-incorporation. While Ga is known to act mainly on the position of the conduction band edge in the selenide compounds, less is known about the impact of Ga on the the energy band positions in sulfur based devices. In this work  $\text{Cu}(\text{In,Ga})\text{S}_2$  solar cells with different Ga-concentrations at the buffer/absorber interface are discussed with regard to the influence of Ga on the device and defect parameters. Absorber layers with different Ga depth profiles were achieved by variation of the temperature-time-progress during the high-temperature sulfurization of the metallic  $\text{Cu}:\text{Ga}/\text{In}$ -precursors. An integral measure of the Ga-concentration at the interface is given by the minimum band gap energy  $E_{g,min}$  derived from  $EQE$  spectra. The activation energy  $E_A$  of the saturation current density and the activation energy  $E_a$  of a deep bulk acceptor obtained from thermal admittance spectroscopy (TAS) were found to increase linearly with  $E_{g,min}$ , respectively. These results suggest that in sulfide compounds the Ga mainly lowers the valence band energy and leaves the conduction band rather unaffected which is in contrast to the influence of Ga observed for the selenide chalcopyrites. Furthermore, TAS revealed defects in Ga-free and Ga-doped samples that are proposed to be related to the prominent features N1 and N2 which are often observed in selenide based chalcopyrites. Since the N1 level has been assigned to interface defects in  $\text{Cu}(\text{In,Ga})\text{Se}_2$ -based devices by several authors, this defect could be of high relevance in the  $\text{Cu}(\text{In,Ga})\text{S}_2$  solar cells which are limited by interface recombination. Experimental results have been presented in literature that support the interpretation of N1 as an interface-related signature. These were derived from capacitance-voltage measurements at different test frequencies and air annealing experiments that aim to demonstrate a passivation of interface defects by oxygen. Applying these methods on selected solar cells based on  $\text{CuInS}_2$  and  $\text{Cu}(\text{In,Ga})\text{S}_2$  absorbers, one signature found in the Ga-free samples could be assigned to N1. Since this signature can be interpreted as an interface defect, it may be involved in recombination processes at the interface which account for the especially low  $V_{oc}$  of these devices.

# Contents

<b>1</b>	<b>Introduction</b>	<b>7</b>
<b>2</b>	<b>Wide-Gap Cu(In,Ga)S<sub>2</sub> Solar Cells</b>	<b>11</b>
2.1	General Design of Chalcopyrite Solar Cells . . . . .	11
2.2	Crystal Structure of Cu(In,Ga)S <sub>2</sub> . . . . .	12
2.3	Native Defect States in Cu(In,Ga)S <sub>2</sub> . . . . .	14
2.4	The High Voltage Limit . . . . .	17
2.5	RTP-Processed Cu(In,Ga)S <sub>2</sub> Samples . . . . .	20
<b>3</b>	<b>Defect States and the Space Charge Capacitance</b>	<b>23</b>
3.1	Carrier Capture and Emission . . . . .	23
3.1.1	Thermodynamics of Carrier Emission . . . . .	27
3.1.2	The Poole-Frenkel Effect . . . . .	28
3.2	The p-n Junction . . . . .	29
3.3	Space Charge Capacitance . . . . .	31
3.4	Contribution of Defects to the Space Charge Capacitance . . . . .	33
<b>4</b>	<b>Capacitance Measurement and Analytical Methods</b>	<b>35</b>
4.1	Equivalent Circuits . . . . .	35
4.2	Admittance Spectroscopy . . . . .	37
4.3	The Meyer-Neldel Rule . . . . .	38
4.4	Capacitance-Voltage Profiling . . . . .	39
<b>5</b>	<b>Investigated Samples</b>	<b>43</b>
5.1	Overview of Investigated Samples . . . . .	43
5.2	Sample Contacting . . . . .	45
<b>6</b>	<b>Results and Discussion</b>	<b>47</b>
6.1	Basic Characterization . . . . .	47
6.1.1	EQE Spectra and IV Characteristics . . . . .	48
6.1.2	Temperature-Dependent IV Characteristics . . . . .	55
6.1.3	Conclusions I . . . . .	59
6.2	Thermal Admittance Spectroscopy . . . . .	61
6.2.1	Defects in HZB Samples with Varied Ga Depth Profiles . . . . .	63
6.2.2	Defects in Ga-doped and Ga-free Solteature Samples . . . . .	70
6.2.3	Defect Mapping with the Meyer-Neldel Rule . . . . .	72
6.2.4	Conclusions II . . . . .	75

*Contents*

6.3	Detailed Investigation of N1-indicative Characteristics . . . . .	76
6.3.1	Influence of the CV Test Frequency on Apparent Doping Distributions . . . . .	77
6.3.2	Air Annealing Experiments . . . . .	81
6.3.3	Conclusions III . . . . .	88
<b>7</b>	<b>Conclusions and Outlook</b>	<b>91</b>
	<b>List of Frequently Used Symbols</b>	<b>95</b>
	<b>Bibliography</b>	<b>104</b>

# 1 Introduction

Global warming due to emission of CO<sub>2</sub> and the health risks arising from nuclear fuels pose a challenge to the future energy supply while the demand for energy rises, especially in the industrial nations but also in the emerging economies. The use and development of alternative energy sources is therefore indispensable and has become a political goal. In 2007 the European Union committed itself to increase the renewable energy portion of final energy to 20 % until 2020 [2]. The involvement of photovoltaics becomes obvious by the fact that our sun provides  $1.5 \cdot 10^{18}$  kWh per year to the earth's surface [3] which is 10 000 times higher than the actual world energy consumption [4].

The major task consists in the cost reduction of photovoltaic systems on a competitive level supported by an increase of module efficiencies. An alternative to the market dominating silicon modules is given by thin film modules which benefit from the use of direct semiconductors as light absorbing materials. An absorber layer thickness of about 1  $\mu\text{m}$  is needed compared to the roughly 100 times larger thickness which is necessary for the application of the indirect semiconductor silicon. Besides the lowering of material quantity, the thin layers reduce the requirements for crystallinity and purity of the material because the distance to be covered by the minority carriers is decreased. This results in faster production processes compared to silicon technologies. Furthermore, the thin layers can be deposited on large areas where a monolithic interconnection of single solar cells can be integrated in the production process by mechanical scribing and laser structuring of the deposited layers [5]. These are essential advantages resulting in material savings and reduction of process steps.

Photovoltaic thin film devices based on Cu-chalcopyrite compounds as absorber material have been studied since 1981, when the first thin film CuInSe<sub>2</sub>/CdS solar cell with an efficiency of 9.4 % was announced by Mickelsen and Chen [6]. Today they present the highest efficiencies among thin film technologies [7] on laboratory scale as well as on module scale with record values of 20.4 % and 15.7 %, respectively [8, 9]. By variation of the  $[\text{Ga}]/([\text{Ga}]+[\text{In}])$  and the  $[\text{S}]/([\text{S}]+[\text{Se}])$  content in Cu(In,Ga)(Se,S)<sub>2</sub> the optical band gap of the semiconductor compound can be tuned from 1.0 eV (CuInSe<sub>2</sub>) to 2.4 eV (CuGaS<sub>2</sub>). This offers the adjustment to the optimum band gap for reaching maximum efficiencies which is assumed to amount to 1.2–1.4 eV [1]. However, the best conversion efficiencies have been reached by absorbers with optical band gap energies around  $E_g = 1.1 - 1.2$  eV [10]. It has been shown that an optimum in crystallinity of the chalcopyrite material exists at a Ga content  $[\text{Ga}]/([\text{Ga}]+[\text{In}]) = 0.2$  corresponding to these values of  $E_g$  [11]. Electronic properties that are influenced by the Ga content, such as the band alignment at the buffer/absorber interface and at the back contact, may also account for the achieved optimum efficiencies at  $E_g = 1.1 - 1.2$  eV.

The solar cells investigated in this work are based on the absorber material Cu(In,Ga)S<sub>2</sub>.

## 1 Introduction

Due to an absorber band gap wider than 1.5 eV these devices yield higher open circuit voltages compared to devices applying low-band gap selenide and sulfo-selenide compounds. Unfortunately, the practical open circuit voltage values resulting from wide-gap absorber materials are far below the theoretically predicted values [12]. As a consequence, the efficiencies of Cu(In,Ga)S<sub>2</sub> heterojunction solar cells did not exceed 12.9 % so far [13]. Recombination via defect states at the heterojunction between the absorber layer and the CdS buffer layer has been evaluated to be the predominant loss mechanism in these solar cells [13, 14]. This is in contrast to Cu(In,Ga)Se<sub>2</sub> solar cells with typical band gap energies in the range of 1.2 to 1.3 eV which are commonly limited by recombination in the bulk [15, 16]. The dominance of interface recombination in Cu(In,Ga)S<sub>2</sub> solar cells is enhanced by a disadvantageous band alignment at the buffer/absorber interface due to the widened absorber band gap as compared to Cu(In,Ga)Se<sub>2</sub> [5, 17]. Additionally, the Cu-rich growth conditions used for the deposition of Cu(In,Ga)S<sub>2</sub> absorbers may support interface recombination [18].

While defects in Cu(In,Ga)Se<sub>2</sub> and their influence on the performance of devices based on this absorber material have been intensively investigated and discussed in literature, much less is known about defects and their specific characteristics in Cu(In,Ga)S<sub>2</sub> devices. One majority defect could be identified by Siemer [19] to be responsible for the limitation of the open circuit voltage ( $V_{oc}$ ). However, this study was restricted to solar cells based on pure CuInS<sub>2</sub> so that the influence of Ga on the loss mechanisms and the defect characteristics still has to be clarified. Therefore, this work focuses on the investigation of the predominant loss mechanisms in Cu(In,Ga)S<sub>2</sub> solar cells and defect states which may be involved with special regard to the influence of Ga.

The thesis is organized as follows:

In Chapter 2, specific properties of Cu(In,Ga)S<sub>2</sub> and solar cells based on this material are introduced and differences between these devices and those based on Cu(In,Ga)Se<sub>2</sub> are explained. An overview of the present knowledge regarding defects in Cu(In,Ga)S<sub>2</sub> is given and the specific challenges in achieving higher open circuit voltages for Cu(In,Ga)S<sub>2</sub> solar cells are demonstrated. A brief description is given of the rapid thermal process (RTP) which was applied by the manufacturers to process the solar cells investigated in this work. Especially the influence of the RTP parameters on the Ga depth profile within the absorber layer is explained.

The measurement of the space charge capacitance offers nondestructive approaches for the characterization of defects in the space charge region of completed solar cells. Defect characterization by capacitive methods represents an essential part of this work. Therefore, the fundamentals needed for the interpretation of the measured space charge capacitance are outlined in Chapter 3 with special regard to the influence of defects on the space charge capacitance. With this background knowledge the thermal admittance spectroscopy (TAS) and the capacitance-voltage ( $CV$ ) profiling are introduced in Chapter 4 since both methods provide valuable information about the properties of the defects on which this thesis is focused. An overview of the samples investigated in this work and experimental details concerning the electrical contacting of the samples is given in Chapter 5.

In Chapter 6 the experimental results are presented and discussed. First, the influence

of gallium at the absorber surface on standard device characteristics is investigated. For this purpose, current-voltage ( $IV$ ) measurements, external quantum efficiency ( $EQE$ ) spectra and energy-dispersive X-ray spectroscopy (EDX) were used. The results demonstrate the impact of the RTP process parameters chosen for the absorber recrystallization on the performance characteristics. Furthermore, temperature-dependent current-voltage ( $IVT$ ) measurements confirm recombination at the buffer/absorber interface as the  $V_{oc}$ -limiting loss mechanism for the samples investigated in this work. While this is a commonly observed result for  $\text{Cu(In,Ga)S}_2$  devices [13, 14], the systematic analysis of samples with absorbers exhibiting different depth profiles of the band gap energy enables valuable conclusions regarding the influence of Ga on the band structure in  $\text{Cu(In,Ga)S}_2$ . These findings are finally supported by a systematic study of defect activation energies by means of TAS on numerous samples with different Ga concentration at the interface. Additionally, TAS reveals signatures that are considered to be related to the prominent signature N1 which is frequently observed in defect spectra of  $\text{Cu(In,Ga)Se}_2$  devices. Minority interface defects were regarded as a possible origin for N1 by some authors [20, 21]. These defects are possibly of minor importance in  $\text{Cu(In,Ga)Se}_2$  solar cells since their performance is limited by recombination losses in the bulk of the absorber. In contrast, similar interface defects occurring in  $\text{Cu(In,Ga)S}_2$  could play an important role in the  $V_{oc}$ -limiting recombination mechanisms at the interface. Following an approach presented by Cwil *et al.* in [20], apparent doping depth profiles derived from capacitance-voltage measurements performed at varied frequencies are consulted to check if the signatures in question may be evoked by interface defects. In addition, device and defect characteristics before and after air annealing of  $\text{Cu(In,Ga)S}_2$  samples are compared. The results serve to verify effects that are comparable to those reported for air annealing of  $\text{Cu(In,Ga)Se}_2$  devices in relation with the N1 signature and which prompted the authors to assume interface defects as the origin of N1 [21].

Chapter 7 summarizes the most important findings gained from this work and suggests approaches for future investigations that could complement the results.



## 2 Wide-Gap $\text{Cu}(\text{In,Ga})\text{S}_2$ Solar Cells

In this chapter the fundamental properties of  $\text{Cu}(\text{In,Ga})\text{S}_2$  solar cells are described. The general structure of these devices and the absorber material are shortly introduced in Sections 2.1 and 2.2, respectively. A summary of the actual knowledge of native defects in  $\text{Cu}(\text{In,Ga})\text{S}_2$  is given in Section 2.3. The challenge of reaching high open circuit voltages ( $V_{oc}$ ) with solar cells based on this absorber material is illuminated in Section 2.4. As appropriate, the distinctive features of  $\text{Cu}(\text{In,Ga})\text{S}_2$  solar cells are compared to selenium-based chalcopyrite solar cells. The rapid thermal process (RTP), by which the samples investigated in this work were processed, is described in Section 2.5.

### 2.1 General Design of Chalcopyrite Solar Cells

The typical structure of a solar cell based on a  $\text{Cu}(\text{In,Ga})(\text{S,Se})_2$  compound semiconductor is presented in Fig. 2.1. In the following, the individual layers and their particular function will be outlined. Even though solar cells manufactured on flexible stainless steel or polymer foils achieve high efficiencies on laboratory scale today [8], most solar cells and modules are still deposited on soda-lime glass. From this glass sodium diffuses into the absorber layer during the process. Its beneficial effects on the growth conditions facilitate the implementation of optimum performance characteristics. To form a back contact, a  $0.5 - 1 \mu\text{m}$  thick molybdenum layer is sputtered on the glass substrate. For the deposition of the absorber layer two different kinds of established processes exist. During the co-evaporation process the elements are deposited from different sources simultaneously on the heated substrate. The adjustment of the individual rates enables to optimize the growth mechanism and to induce gradients of single constituents.

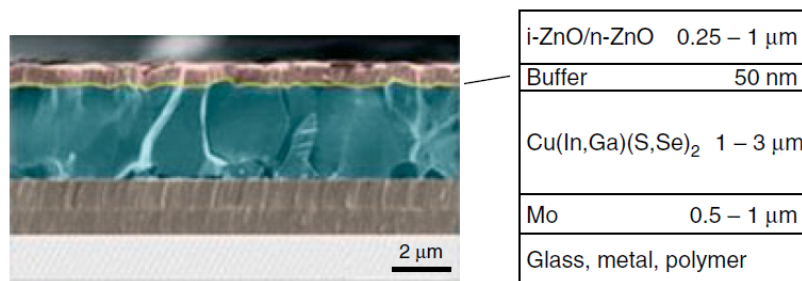


**Fig. 2.1:** Cross section and schematic representation of a thin film solar cell based on the absorber material  $\text{Cu}(\text{In,Ga})(\text{S,Se})_2$ . From [5].

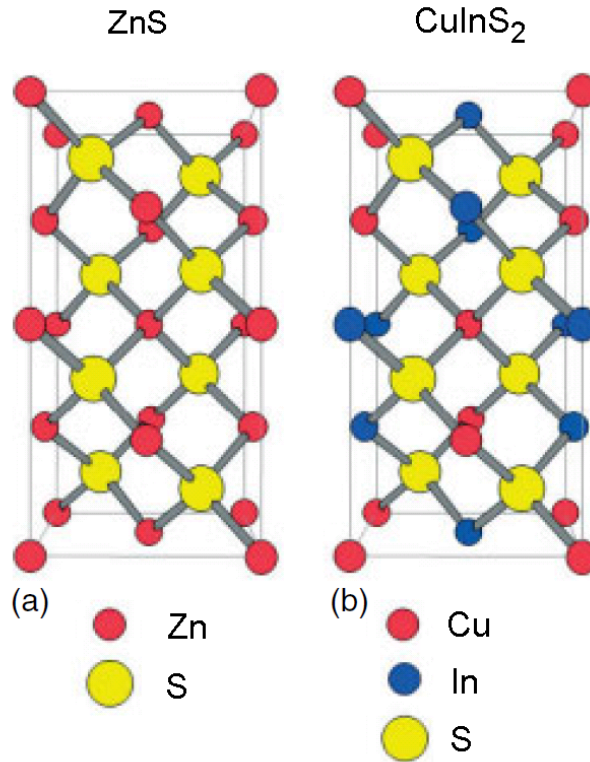


**Fig. 2.2:** The zinc blende structure of the binary compound  $\text{ZnS}$  (a) and the ternary chalcopyrite compound  $\text{CuInS}_2$  (b). The reduced symmetry of the  $\text{CuInS}_2$  lattice doubles the size of the unit cell relative to the unit cell of  $\text{ZnS}$ . From [5].

Another approach is given by the sequential selenization/sulfurization process in which the metallic precursors from Cu, In and Ga are deposited on the substrate. In a second step they are annealed within  $\text{H}_2\text{Se}/\text{H}_2\text{S}$  or Se/S atmosphere to build the chalcopyrite. The absorber layer thickness is adopted to the penetration depth of the sunlight and commonly amounts to 1 – 3  $\mu\text{m}$ . Chemical bath deposition is applied to form a thin CdS layer ( $\approx 50$  nm) on top of the absorber. It acts as a buffer layer by preventing shunting paths between the absorber and the ZnO layer which serves as front contact of the device. The ZnO layer is optically transparent and mostly split into an intrinsic and a highly n-doped part.

## 2.2 Crystal Structure of $\text{Cu}(\text{In,Ga})\text{S}_2$

$\text{CuInS}_2$  belongs to the ternary chalcopyrite compounds whose crystal structure is based on the zinc blende structure which is a modification of the diamond cubic crystal structure. The diamond crystal structure may be adopted by group IV elements such as carbon, silicon and germanium. It is built up of two face centered cubic lattices, displaced from each other by one quarter of the diagonal. Each of the atoms is tetrahedrally bound to three neighboring atoms. According to the Grimm-Sommerfeld rule [22], a tetrahedral structure can also be formed if the average density of valence

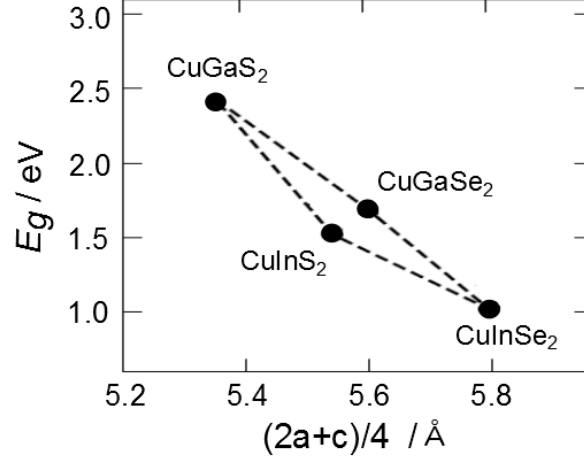


**Fig. 2.3:** Direct band gap energy  $E_g$  versus lattice parameter  $(2a+c)/4$  for ternary copper chalcopyrite compound semiconductors. Dashed lines represent miscibilities within the  $\text{Cu}(\text{In,Ga})(\text{S,Se})_2$  system. From [5], modified.

electrons per atom amounts to four. Consequently, the tetrahedral structure is preserved in the zinc blende structure, where group IV elements of the diamond lattice are substituted by group III and group V elements such as gallium and arsenic (GaAs) or by group II and group VI elements such as zinc and sulfur (ZnS). Thereby one of the deferred lattices is occupied by cations (e.g. Zn) and the other lattice is occupied by anions (e.g. S), as demonstrated in Fig. 2.2 (a). In a ternary chalcopyrite compound the cations of the zinc blende structure are substituted by cations of both lower and higher valency, that is  $\text{CuInS}_2$  is obtained by replacing zinc in ZnS by copper and indium, which still conforms to the Grimm-Sommerfeld rule.

In the  $\text{CuInS}_2$  lattice, the tetrahedron consisting of the sulfur atom surrounded by four cations is irregular due to the different bond length of Cu-S and In-S. As illustrated in Fig. 2.2 (b) the reduced symmetry results in a body centered tetrahedral structure with a larger primitive cell built up of eight atoms compared to four atoms in case of the zinc blende structure. If the cations In and S are distributed randomly, it is referred to as sphalerite structure. As a result of a shorter bond length of Cu-S versus that of In-S, the primitive cell is stretched along the crystal  $c$ -axis resulting in an increased  $c/a$  ratio relative to the ideal value of  $c/a = 2.0$ . In contrast, the primitive cell is compressed in case of  $\text{CuGaS}_2$  due to an oppositional relation of the bond lengths. By an isovalent replacement of a part of the In atoms by Ga atoms in  $\text{CuInS}_2$ , the quaternary chalcopyrite compound  $\text{Cu}(\text{In,Ga})\text{S}_2$  is built without violating the Grimm-Sommerfeld rule.

While the electronic properties of these solid solutions remain the same for different compositions, the lattice constants and the band gap energy  $E_g$  vary approximately linear with the atomic ratios of the constituents between the values of the pure ternary chalcopyrite compounds, following Vegard's law [23]. Fig. 2.3 demonstrates how the modification of the  $[\text{S}]/([\text{S}]+[\text{Se}])$  and the  $[\text{Ga}]/([\text{Ga}]+[\text{In}])$  ratios in

the Cu(In,Ga)(S,Se)<sub>2</sub> system varies the lattice constants and thereby the band gap energy of the respective material.

## 2.3 Native Defect States in Cu(In,Ga)S<sub>2</sub>

One conventional classification of defects is to distinguish between "shallow states" and "deep states". Shallow states exhibit a low ionization energy which can be described by a modified hydrogenic model described in [24]. In the energy band model shallow states are located close to their corresponding band edges (valence band for acceptors and conduction band for donors). Due to their weak binding energy they can be thermally ionized at room temperature. While in an n-type semiconductor the shallow donor states dominate which are positively charged when ionized, a p-type semiconductor contains a superior number of shallow acceptor states being negatively charged when ionized [24]. Deep states are located deeper in the energy gap and have a larger ionization energy. In the strong potential the charge carrier is tightly bound to the site of the defect contrary to the diffuse character of shallow states. The high localization in position space corresponds to a delocalization in the momentum space. As a consequence of the strong lattice coupling, recombination via deep states is likely to be non-radiative making the observation of photoluminescence from transitions via deep defect states rather improbable. An adequate alternative to investigate the properties of deep states is provided by capacitance methods which will be utilized in this work [24].

In the ternary compound CuInS<sub>2</sub> 12 intrinsic defects are possible. These are the vacancies  $V_{\text{Cu}}$ ,  $V_{\text{In}}$ ,  $V_{\text{S}}$ , the interstitials  $\text{Cu}_i$ ,  $\text{In}_i$ ,  $\text{S}_i$  and the antisite positions  $\text{Cu}_{\text{In}}$ ,  $\text{Cu}_{\text{S}}$ ,  $\text{In}_{\text{Cu}}$ ,  $\text{In}_{\text{S}}$ ,  $\text{S}_{\text{In}}$ ,  $\text{S}_{\text{Cu}}$ . Additionally, some of these defects may form defect complexes like  $V_{\text{Cu}}\text{-In}_{\text{Cu}}$  [25]. The probability for the occurrence of a defect is determined by its formation energy which has been calculated for CuInS<sub>2</sub> by several authors [26–29]. Due to their low formation energy, acceptor-like Cu vacancies are held responsible for the intrinsic p-type doping of CuInS<sub>2</sub> [27]. Depending on the growth conditions the p-type doping may be compensated more or less by donor-like defect states. For instance, the donor-like sulfur vacancy  $V_{\text{S}}$  is assumed to cause a semi-insulating character of CuInS<sub>2</sub> if the material is grown under Cu-poor conditions [30]. Therefore, CuInS<sub>2</sub> films have to be prepared under Cu-excess which induces a secondary Cu-S phase being beneficial for the incorporation of sulfur [31]. A list of experimentally detected defects in CuInS<sub>2</sub> taken from literature is given in Table 2.1. From this listing it can be seen, that since the 1980s the photoluminescence (PL) technique is one of the most frequently used methods to study defects in CuInS<sub>2</sub>. This method is only suitable for the detection of radiative recombination which is likely to occur within transitions involving shallow defect states and less probable via deep defect states. Nevertheless Lewerenz and Dietz [32] postulated two deep defect states at 350 meV and 625 meV above the valence band maximum (VBM) by combining their results from Brewster angle spectroscopy (BAS) with PL-data from literature. These values are similar to those from Siemer [19] and Kneisel *et al.* [33] measured by means of thermal admittance spectroscopy (TAS) and deep level transient spectroscopy (DLTS). It should be noted that

the material investigated by Lewerenz and Dietz was an n-type crystal (grown under sulfur- and indium-excess) whereas the authors of references [19] and [33] investigated complete solar cell devices with a p-type  $\text{CuInS}_2$  layer. The authors Kneisel *et al.* [33] and Siemer [19] observed both of the deep defects as majority defects<sup>1</sup> in the DLTS spectrum in most of the investigated samples which were prepared under different growth conditions. In one sample from a rapid thermal process (RTP) a minority defect signature with an activation energy of 300 meV occurred. The open circuit voltage of the investigated solar cells was found to decrease with increasing concentration of the deeper defect at 500 meV. Because recombination at the interface was identified via temperature-dependent current-voltage *IVT* measurements as the predominant recombination process in these solar cells, the detrimental defect was supposed to be an interface defect.

In addition to the defects occurring in pure  $\text{CuInS}_2$ , the defect spectrum is expected to change with the incorporation of gallium into the compound. Aside from the formation of additional defects or saturation of defects by Ga, the band gap widening is likely to increase the energetic distances of particular defect states to the valence and conduction band edges which also potentially changes the influence of these defects on other electrical characteristics of a  $\text{Cu}(\text{In},\text{Ga})\text{S}_2$  solar cell device. Hitherto deep defects in  $\text{Cu}(\text{In},\text{Ga})\text{S}_2$  solar cells especially in consideration of the influence of Ga have rarely been investigated. Turcu *et al.* [37] performed TAS and DLTS on solar cells based on  $\text{Cu}(\text{In}_{1-x}\text{Ga}_x)(\text{Se}_{1-y}\text{S}_y)_2$  absorbers with  $0 < y < 0.7$  for two series with  $x = 0$  and  $x \approx 0.3$ , respectively. They observed the systematic increase of the activation energy of two defect levels with increasing band gap energy due to the addition of gallium and sulfur. The authors related these defects to the signatures N1 and N2 which are frequently observed in selenium-based chalcopyrite solar cells. It was already known that the concentration of the trap level N2, which had been assigned to a bulk acceptor level [38, 39] with activation energies between 200 and 600 meV, correlates with the  $V_{oc}$  in  $\text{Cu}(\text{In},\text{Ga})\text{Se}_2$  samples [40, 41]. In their study, Turcu *et al.* demonstrated that the variation of the activation energies of N1 and N2 could be used to establish the band lineups of  $\text{Cu}(\text{In},\text{Ga})(\text{Se},\text{S})_2$  compounds: The activation energies of both N1 and N2 were found to increase with increasing  $[\text{S}]/([\text{S}]+[\text{Se}])$  ratio, whereas the  $[\text{Ga}]/([\text{Ga}]+[\text{In}])$  ratio only correlated with the activation energy of N1. They concluded, that sulfur widens the band gap by shifting both energy bands to approximately equal parts while Ga mainly acts on the conduction band in devices with moderate sulfur-concentrations.

In contrast to the reports concerning N2, the nature of N1 whose activation energy ranges from 30 to 200 meV is a controversial subject up to date. Up to now, the discussions on N1 are basically restricted to selenium-based compounds. The interpretations include N1 in the role of a minority defect at or close to the CdS/chalcopyrite interface [21, 42–44], N1 as an acceptor in the bulk [45, 46] or donor in the bulk [47–49], whereas recent studies consider a non-ohmic back contact barrier [50] or a thermal activated hopping conduction [51] to evoke the N1 signature in TAS and DLTS spectra. A clear attribution of N1 to a defect level is complicated by the fact that up to four different peaks associated with N1 are observed in DLTS spectra whose contributions depend on

---

<sup>1</sup>The classifications "minority defect" and "majority defect" will be explained in Section 3.1.

**Table 2.1:** Defect energies taken from literature for intrinsic defects in CuInS<sub>2</sub> by various measurement techniques (PL = photoluminescence, P-H = Pauw-Hall, BAS = Brewster angle spectroscopy, MS = Mössbauer spectroscopy) and some not assigned defect levels which have been detected by thermal admittance spectroscopy (TAS), deep level transient spectroscopy (DLTS) or have been postulated as a consequence of specific PL results. D and A denote the assignment of a defect level to a donor or acceptor state, respectively.

assignment	defect energy	defect type	detection method	reference
In <sub>i</sub>	66 meV, 70 meV	D	PL	[34]
	70 meV	D	PL, P-H	[27]
V <sub>Cu</sub>	100 meV	A	PL	[27, 34, 35]
	80 meV	A	BAS	[32]
In <sub>Cu</sub>	125 meV	D	PL	[34]
	145 meV	D	PL, P-H	[27]
	110 meV	D	BAS	[32]
(?)	35 meV	D	MS	[36]
V <sub>S</sub>	150 meV	D	PL	[34]
	35 meV	D	PL, P-H	[27]
S <sub>i</sub>	170 meV	A	PL	[34]
	150-180 meV	A	PL, BAS	[32]
V <sub>In</sub> (?)	150 meV	A	PL	[35]
	150 meV	A	MS	[36]
Cu <sub>In</sub> (?)	150 meV	A	PL	[35]
	150 meV	A	MS	[36]
S <sub>Cu</sub>	300 meV	D	PL	[34]
In <sub>S</sub>	330 meV	D	PL	[34]
S <sub>In</sub>	390 meV	A	PL	[34]
?	350 meV	A	postulated	[32]
?	625 meV	A	postulated	[32]
?	300 meV	A/D	TAS, DLTS	[19, 33]
?	500 meV	A	TAS, DLTS	[19, 33]

the pretreatment of the samples and the measurement conditions [52]. In the interpretation as an interface defect the increase in activation energy of N1 in DLTS and TAS spectra after annealing under oxygen atmosphere has been explained by an increase of the distance between the conduction band minimum (CBM) and the Fermi level position at the CdS/Cu(In,Ga)Se<sub>2</sub> interface due to saturation of the interface defects by oxygen [21, 44]. As reported in [44] the changes of the activation energy were ac-

accompanied by a broadening of the space charge region coming along with a reduction of the surface-near doping concentration and a reduction of the  $V_{oc}$ . The inconsistency of a decrease in doping concentration with the saturation of compensating donors close to the interface was explained by copper migration from the surface in the direction of the bulk. Dirnstorfer *et al.* discovered an increase in charge carrier concentration upon air annealing of In-rich grown  $\text{Cu}(\text{In,Ga})\text{Se}_2$  thin films and explained the phenomenon by the reaction  $2\text{In}_{\text{Cu}} + \text{O}_2 \rightarrow 2\text{V}_{\text{Cu}} + 2\text{InO}$  or by saturation of  $\text{V}_{\text{Se}}$  donors with oxygen [53]. The latter interpretation was also proposed in [54] and [55] where a reduced donor concentration and reduced  $\text{V}_{\text{Se}}$  concentration was observed after air annealing of  $\text{Cu}(\text{In,Ga})\text{Se}_2$  thin films.

However, it is not clarified if N1 and N2 do also exist in solar cells based on selenium-free chalcopyrite solar cells. Even if related defects exist in sulfur-based solar cells, they may have different influences on the device characteristics compared to the effect of N1 and N2 in selenium-based devices. N1 in the role of a defect at or close to the interface can be expected to be harmless regarding the performance of  $\text{Cu}(\text{In,Ga})\text{Se}_2$  solar cells, because recombination in the bulk is generally assumed to limit the  $V_{oc}$  in these devices [15, 16]. By contrast, in  $\text{Cu}(\text{In,Ga})\text{S}_2$  solar cells recombination at the interface is impeding the optimization of the  $V_{oc}$ , as will be discussed in Section 2.4. Therefore, the identification of N1 and the investigation of its properties in the  $\text{Cu}(\text{In,Ga})\text{S}_2$  samples studied in this work will play a decisive role in Section 6.3.

## 2.4 The High Voltage Limit

One approach to improve the performance of  $\text{Cu}(\text{In,Ga})\text{Se}_2$  solar cells is to tune their absorber band gap close to the optimum value of about 1.2 to 1.4 eV, which has been calculated by Shockley and Queisser [1]. Many attempts have been made concerning this matter by modification of the gallium and the sulfur content of the absorber to widen the band gap related to that of pure  $\text{CuInSe}_2$ . Unfortunately, the increase of the band gap energy was only accompanied by a linear increase in the open circuit voltage up to band gap values of 1.2 eV [12, 56]. Fig. 2.4 demonstrates how the wide-gap materials remain beyond the predicted values of the conversion efficiency due to shortcomings in the  $V_{oc}$ . In particular the total replacement of Se by S, which corresponds to the materials investigated in this study, appears to be detrimental.

To identify the origin of the  $V_{oc}$  losses the absorber material has to be considered in the framework of the complete solar cell device. In Fig. 2.5 the band alignments at the heterojunction between absorber and emitter material resulting from wide-gap (a) and low-gap (b) materials are shown. In case (a) the band gap of the absorber is widened by lifting up the CBM and lowering down the VBM relative to the band positions in case (b). For the  $\text{Cu}(\text{In,Ga})(\text{Se,S})_2$  solar cells the sulfur content is known to influence both bands to equal parts whereas the amount of Ga has been found experimentally by means of defect spectroscopy to affect mainly the CBM in  $\text{Cu}(\text{In,Ga})\text{Se}_2$  [37]. In contrast, there are indications of an impact of Ga on the VBM in  $\text{Cu}(\text{In,Ga})\text{S}_2$  devices given directly by experimental results [37] but also by logical consequences derived from the observed impact of Ga on the  $V_{oc}$  [17].

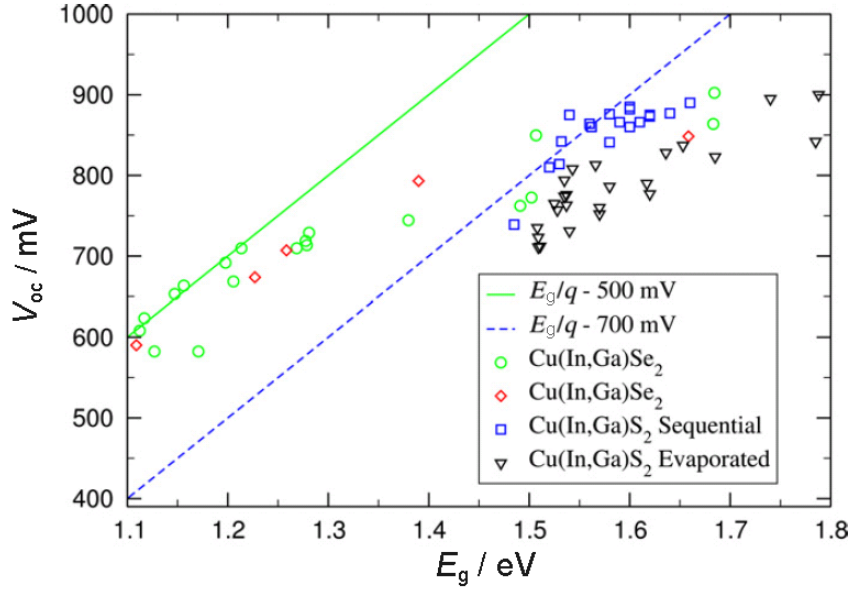


**Fig. 2.4:**  $V_{oc}$  versus  $E_g$  for Cu(In,Ga)Se<sub>2</sub> and Cu(In,Ga)S<sub>2</sub> based solar cells. From [12] (green and red symbols represent data taken from [57] and [58], respectively). The straight green line and the dashed blue line serve to demonstrate the non-linear trend of the  $V_{oc}$  values related to  $E_g$  for  $E_g > 1.3$  eV.

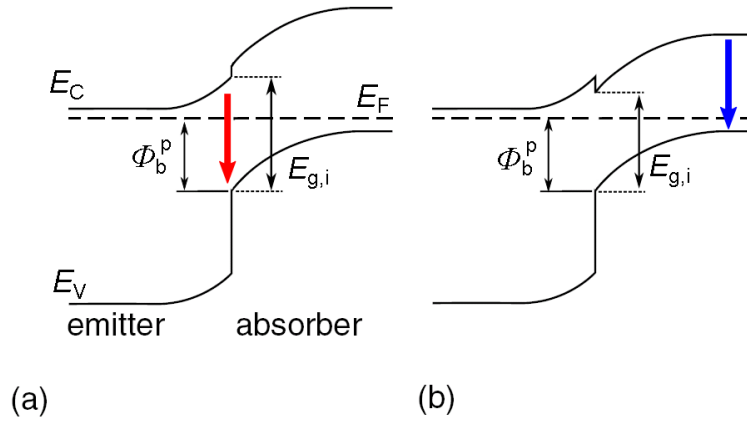


**Fig. 2.5:** Simplified energy band gap diagrams for (a) a negative (cliff)(b) a positive (spike) band offset at the interface between absorber and emitter material.  $E_{g,i}$  denotes the interface band gap and  $\Phi_b^p$  the recombination barrier for holes at the heterointerface. The red and the blue arrow indicate the recombination paths at the interface and in the absorber bulk, respectively. From [5], modified.

As demonstrated in Fig. 2.5 (a) an increase of the CBM results in a negative conduction band offset ("cliff") in the band alignment at the heterojunction contrary to the presence of a positive conduction band offset ("spike") indicated in Fig. 2.5 (b). The changeover from a spike to a cliff in the conduction band results in an interface band gap  $E_{g,i}$  that is smaller than the absorber band gap. Thereby, the recombination of electrons and holes at the interface (red arrow) is facilitated compared to that in the bulk (blue arrow). In addition, an unfavorable Fermi level position closer to mid gap at the heterojunction rather than close to the CBM is expected. Such a "reduced type inversion" furthermore enhances interface recombination. The increased impact of recombination losses at the interface versus recombination mechanisms in the depletion region<sup>2</sup> or in the neutral bulk has therefore been proposed to be responsible for the losses in  $V_{oc}$  in devices with cliff-like heterojunctions [59, 60].

Malmström *et al.* showed by means of recombination characteristics and activation energy of the saturation current density  $J_0$  that in solar cells based on the absorber material CuGaSe<sub>2</sub> recombination at the interface represents the predominant recombination mechanism [58]. On the other hand it could be shown that under Cu-poor growth conditions not the recombination at the interface but the recombination in the depletion region is the dominant loss process in pure CuGaSe<sub>2</sub> [61]. Turcu *et al.* studied the relationship between Cu-rich/ Cu-poor growth and the recombination characteristics and suggested that Cu-poor growth suppresses interface recombination [18]. A widened band gap at the surface of Cu-poor grown absorbers has been assumed to result from a surface defect layer (SDL), arising from a phase segregation of Cu(In,Ga)<sub>3</sub>Se<sub>5</sub> [18, 56]. It seems to improve the type inversion at the interface either by pinning the Fermi level close to the CBM or by inhibiting an n-type character [56]. Such a surface defect layer is unlikely to occur in Cu(In,Ga)S<sub>2</sub> absorbers because this chalcopyrite material can only be grown under Cu-rich conditions [30]. Therefore, the beneficial effect of the SDL on the type inversion at the interface, which is assumed to prohibit losses in  $V_{oc}$  via interface recombination in Cu(In,Ga)Se<sub>2</sub> devices, is unlikely to be present in Cu(In,Ga)S<sub>2</sub> solar cells. Indeed, interface recombination has been identified as the predominant recombination mechanism in these devices by several authors [13, 14, 62, 63] even if a wide-gap buffer layer is used [63]. Moreover, recombination at the interface is promoted by a negative conduction band offset [5, 17] which is estimated to amount to about 300 meV in Cu(In,Ga)S<sub>2</sub>/CdS junctions [64, 65]. Besides the minimization of defects at the interface, an increase of the recombination barrier by lowering the VBM may support the reduction of interface recombination. Due to the cliff in the conduction band alignment, an increase of the absorber CBM is not expected to increase the  $V_{oc}$  as long as recombination at the interface dominates the recombination losses [17, 56]. Consequently, it is of special interest to verify to which parts an increased Ga content shifts the CBM and VBM in Cu(In,Ga)S<sub>2</sub>. In order to answer this question, Johnson investigated CdS/Cu(In,Ga)S<sub>2</sub> junctions with various Ga-concentrations at the heterocontact by means of X-ray photoelectron spectroscopy (XPS) and ultraviolet photoelectron spectroscopy [66]. The author found no influence of Ga on the valence band offset but an up-shift in the CBM with increasing Ga-content. However,

---

<sup>2</sup>The terms "depletion region" and "space charge region" will be used in the same context in this work.

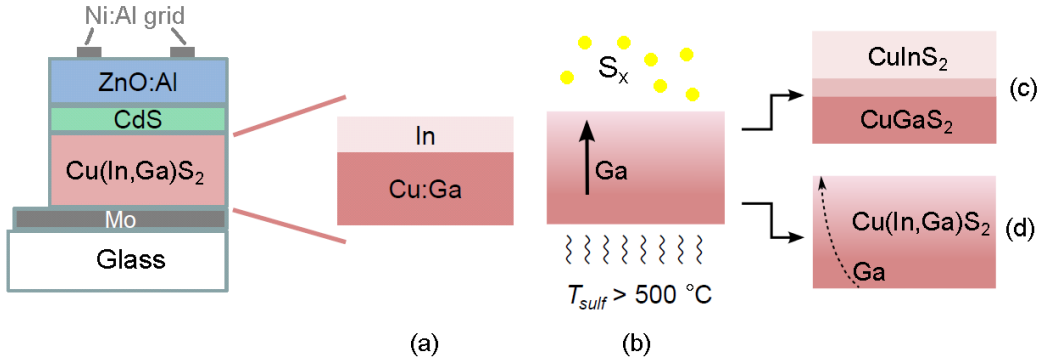


**Fig. 2.6:** Principle of the RTP process for the deposition of a  $\text{Cu}(\text{In,Ga})\text{S}_2$  absorber: Stacked layers are sputtered from In and Cu:Ga targets (a) and afterwards sulfurized by annealing the precursor in sulfur atmosphere (b). Too low annealing temperature and too short annealing duration may result in a top-bottom segregation of  $\text{CuInS}_2$  and  $\text{CuGaS}_2$  (c). Appropriate annealing temperatures support Ga-diffusion from the back towards the surface of the absorber (d).

the measurement error of the applied methods amounts to about 200 meV. Within this error range, it may be difficult to definitely ascribe the band gap widening of about 100... 150 meV to the shift of one of the bands.

## 2.5 RTP-Processed $\text{Cu}(\text{In,Ga})\text{S}_2$ Samples

For the commercial fabrication of modules based on chalcopyrite absorber materials a low cost process is required which delivers homogeneous layers on large scale in short periods of time. These conditions are met by the rapid thermal process (RTP) which was used by the manufacturers Soltecture and the Helmholtz-Zentrum Berlin (HZB) to process the samples investigated in this work. The RTP process is a sequential process performed in two steps. Within the first step stacked metal or alloy precursors are sputtered on the molybdenum coated glass substrate. To obtain pure  $\text{CuInS}_2$  one layer is sputtered from a target of copper and a second one of elemental indium. For achieving  $\text{Cu}(\text{In,Ga})\text{S}_2$  the Cu layer is replaced by a Cu:Ga layer as illustrated in Fig. 2.6 (a). The samples are processed under Cu-excess with a  $[\text{Cu}]/([\text{In}]+[\text{Ga}])$  atomic ratio of 1.5 to provide a  $\text{Cu}_x\text{S}$  phase during the growth process. In a second step the sulfurization process is performed by heating the precursors and elemental sulfur simultaneously with halogen lamps in a reaction chamber at temperatures  $T_{sulf} > 500^\circ\text{C}$  (Fig. 2.6 (b)). During this process step a  $\text{Cu}_x\text{S}$  phase segregates on top of the absorber which is removed by a KCN etch prior to the deposition of the CdS buffer, the ZnO:Al/i-ZnO layer and the Ni:Al contact grid.

To increase the open circuit voltage compared to pure  $\text{CuInS}_2$ , the band gap needs to be widened by Ga at the surface of the absorber. This is required to enable an enhanced quasi-Fermi level splitting which raises the upper limit for the  $V_{oc}$ . It has been shown that longer annealing duration and higher annealing temperatures lead to higher

minimum band gap energies  $E_{g,min}$  and  $V_{oc}$  [67, 68]. In RTP processed Cu(In,Ga)S<sub>2</sub> samples  $E_{g,min}$  is typically located at the absorber surface due to a decreasing Ga-concentration from the back contact towards the surface<sup>3</sup>. The selection of adequate sulfurization parameters is therefore of high relevance to prevent a top-bottom segregation of CuInS<sub>2</sub> and CuGaS<sub>2</sub> as depicted in Fig. 2.6 (c) and (d). Details on the specific process parameters of the samples investigated in this work will be given in Section 5.1.

---

<sup>3</sup> $E_{g,min}$  can be derived from the onset of the external quantum efficiency (EQE) at low photon energies



# 3 Defect States and the Space Charge Capacitance

As outlined in Sections 2.3 and 2.4, defects in the absorber material of a solar cell are of high relevance regarding the performance characteristics of the device. On the one hand, shallow defects which account for doping represent a basic requirement for the semiconductors to be suitable absorbers. These defects are also responsible for the space charge which builds up between the n- and the p-side of a solar cell. Additionally, charge implemented by defects at a proper location within a heterojunction of a solar cell may exhibit a beneficial effect in preventing recombination losses. On the other hand, especially deep defects can be detrimental by acting as recombination centers and thereby limiting the open circuit voltage of the device. The fundamentals of defect physics with special regard to their contribution to the space charge are the matter of this chapter. For a detailed description, the reader is referred to reference [69] which provides the main source for this chapter and reference [70] on which the content of Section 3.4 relies.

## 3.1 Carrier Capture and Emission

The dynamic electronic behavior of a deep state of density  $N_t$  can be described by the emission and capture processes for electrons and holes as depicted in Fig. 3.1. For electrons the capture rate  $c_n$  is defined by the capture cross section  $\sigma_n$ , the thermal velocity  $v_n$  and the concentration of free electrons  $n$ :

$$c_n = \sigma_n \langle v_n \rangle n \quad (3.1)$$

where the average thermal velocity for electrons is given by

$$\langle v_n \rangle = \sqrt{\frac{3kT}{m_e^*}} \quad (3.2)$$

with the Boltzmann constant  $k$ , the temperature  $T$  and the electron effective mass  $m_e^*$ . Analogous expressions can be written for the capture rate  $c_p$  and the thermal velocity  $\langle v_p \rangle$  for holes.

As illustrated in Fig. 3.1, electrons are emitted and holes are captured at the  $n_t$  states occupied by electrons whereas holes are emitted and electrons captured at the  $p_t$  states not occupied by electrons. These processes can be described by the generation rates  $G$

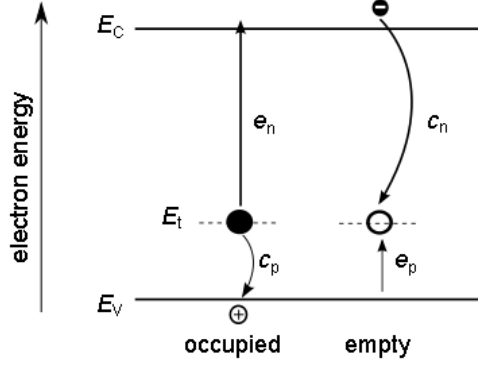


**Fig. 3.1:** Band diagram of a semiconductor depicting the carrier capture and emission processes of an occupied and an empty trap.

and recombination rates  $R$  for electrons and holes, respectively:

$$\left. \begin{array}{l} G_n = e_n n_t \\ R_n = c_n p_t \end{array} \right\} \text{ for electrons} \quad (3.3)$$

$$\left. \begin{array}{l} G_p = e_p p_t \\ R_p = c_p n_t \end{array} \right\} \text{ for holes} \quad (3.4)$$

where  $e_n$  and  $e_p$  denote the emission rate for electrons and holes, respectively. Using these expressions for the recombination and generation mechanisms, the change in the free electron and hole densities can be described by the following continuity equations:

$$\frac{dn}{dt} = G_n - R_n = e_n n_t - c_n p_t \quad (3.5)$$

$$\frac{dp}{dt} = G_p - R_p = e_p p_t - c_p n_t \quad (3.6)$$

All of these competing capture and emission processes influence the electron occupation of the defect state. Accordingly, the change in the occupation of the defect by electrons is given by

$$\frac{dn_t}{dt} = \frac{dp}{dt} - \frac{dn}{dt} = (c_n + e_p)(N_t - n_t) - (c_p + e_n)n_t \quad (3.7)$$

where the defect concentration  $N_t$  is introduced by the relation  $p_t = N_t - n_t$ .

The temperature dependence of the emission rates for electrons and holes can be derived from the principle of detailed balance. The latter claims that in thermal equilibrium

the generation rate and the recombination rate for electrons must be equal and the generation and recombination rates for holes must be equal. Using Equations (3.3) and (3.4) this is expressed by

$$e_n n_t = c_n (N_t - n_t) \quad (3.8)$$

and

$$e_p (N_t - n_t) = c_p n_t \quad (3.9)$$

resulting in the thermal equilibrium occupancy

$$\frac{n_t}{N_t} = \frac{c_n}{c_n + e_n} = \frac{e_p}{e_p + c_p} \quad (3.10)$$

Furthermore, the occupation of the trap level at energy  $E_t$  can be described using the Fermi-Dirac distribution function. Taking into account the degeneracy factors  $g_0$  for a trap state being empty of electrons and  $g_1$  for a trap state being occupied by one electron, the occupation of the state is given by

$$\frac{n_t}{N_t} = \left[ 1 + \frac{g_0}{g_1} \exp\left(\frac{E_t - E_F}{kT}\right) \right]^{-1} \quad (3.11)$$

where  $E_F$  is the Fermi energy. For steady state conditions where the thermal equilibrium is disturbed (irradiation, bias voltage in p-n junctions) the occupation probability is no longer described by the equilibrium Fermi statistics. The distribution function of electrons and holes is then given by their quasi-Fermi statistics with the quasi-Fermi level  $E_{Fn}$  for electrons and  $E_{Fp}$  for holes, respectively. However, in thermal equilibrium combining Equations (3.11) and (3.10) gives

$$\frac{e_n}{c_n} = \frac{g_0}{g_1} \exp\left(\frac{E_t - E_F}{kT}\right) \quad (3.12)$$

for electron emission and

$$\frac{e_p}{c_p} = \frac{g_1}{g_0} \exp\left(\frac{E_F - E_t}{kT}\right) \quad (3.13)$$

for hole emission. Equations (3.12) and (3.13) indicate that the energetic position of the trap level relative to the Fermi energy determines whether the capture rate or the emission rate for each type of charge carrier dominates. Assuming  $(g_1/g_0) \approx 1$  the relation between  $E_t$  and  $E_F$  allows the following conclusions regarding the occupation of a defect state:

- $E_t < E_F$ : The state is mainly occupied by electrons.
- $E_t > E_F$ : The state is mainly empty.
- $E_t = E_F$ : 50 % of the state is occupied.

### 3 Defect States and the Space Charge Capacitance

The relationship between the ratios  $e_n/c_n$  and  $e_p/c_p$  and the Fermi level position originates from the dependence of the capture rates on the free electron density  $n$  and the free hole density  $p$ , respectively (see equation (3.1) for electron capture). These are functions of the Fermi level position to the corresponding band edge:

$$n = N_C \exp\left(-\frac{E_C - E_F}{kT}\right) \quad (3.14)$$

$$p = N_V \exp\left(-\frac{E_F - E_V}{kT}\right) \quad (3.15)$$

where  $E_C$  and  $E_V$  represent the energy of the conduction band minimum and the valence band maximum, respectively, and  $N_C$  and  $N_V$  the corresponding densities of states.

The capture rates  $c_n$  and  $c_p$  therefore depend on the doping density of the material. In contrast, the capture cross sections  $\sigma_n$  and  $\sigma_p$  as well as the emission rates  $e_n$  and  $e_p$  are specific properties of the deep state. Equations (3.1) and (3.14) combined with equation (3.12) deliver the temperature dependence of the emission rate  $e_n$  for electrons:

$$e_n(T) = \sigma_n \langle v_n \rangle \frac{g_0}{g_1} N_C \exp\left(-\frac{E_C - E_t}{kT}\right) \quad (3.16)$$

The analogous expression for the hole emission rate  $e_p$  is

$$e_p(T) = \sigma_p \langle v_p \rangle \frac{g_1}{g_0} N_V \exp\left(-\frac{E_t - E_V}{kT}\right) \quad (3.17)$$

By using the ratio of the thermal emission rates  $e_p(T)$  and  $e_n(T)$  defects are often categorized into minority and majority defect states:

For a p-type semiconductor where electrons are considered as minority carriers, a defect is called minority defect if  $e_n > e_p$ . This is the case when  $(E_C - E_t) < (E_t - E_V)$  as can be derived from Equations (3.16) and (3.17)<sup>1</sup>, indicating that a minority defect state must be positioned in the upper half of the band gap in a p-type semiconductor. Accordingly, majority defects with  $e_p > e_n$  are positioned in the lower half of the band gap. In case of an n-type semiconductor where holes represent the minority carriers it is the other way round: Minority defects with  $e_p > e_n$  are located in the lower half and majority defects with  $e_n > e_p$  in the upper half of the band gap.

Taking into account the temperature dependencies  $\langle v_p \rangle \propto T^{1/2}$  (see Equation (3.2)) and  $N_V \propto T^{3/2}$ , a temperature-independent prefactor  $\xi = (\langle v_p \rangle N_V \sigma_p) / T^2$  can be introduced. Assuming  $g_1/g_0 \approx 1$ , Equation (3.17) can be transformed to

$$\frac{e_p(T)}{T^2} = \xi \exp\left(-\frac{E_a}{kT}\right) \quad (3.18)$$

---

<sup>1</sup>It is assumed that the difference between the products of the pre-exponential factors in (3.16) and (3.17) can be neglected, respectively.

where  $E_a = E_t - E_V$ . If the hole emission rate  $e_p$  of a trap is measured at several temperatures  $T$ , a semilogarithmic plot of  $e_p/T^2$  against the inverse temperature results in a straight line. This so-called "Arrhenius plot" enables to derive the thermal activation energy from the slope and the cross section  $\sigma_p$  from the axis intercept  $\ln \xi$  provided that  $\langle v_p \rangle$  and  $N_V$  are known. For the emission of electrons analogous expressions to Equation (3.18) and  $\xi$  can be derived from Equation (3.16), where  $E_a = E_C - E_t$ . In case of a thermally activated capture cross section  $\sigma_{n,p}$ , the activation energy derived from the slope is the sum of the energetic distance  $E_a$  of the defect state to the corresponding energy band and the thermal activation energy  $\Delta E_\sigma$  of the cross section.

### 3.1.1 Thermodynamics of Carrier Emission

In the previous section the energetic distances between a defect state and the band edges were considered to be temperature-independent. As described in [69, p. 426-432], this is not entirely correct and will be shortly discussed in this section using the example of hole emission<sup>2</sup> according to Equation (3.17). In the following, the capture cross section  $\sigma_p$  is assumed to be temperature-independent. The distance between a defect state and a band edge is described by the chemical potential for the formation of a free carrier and an ionized defect. This chemical potential is defined as the change in Gibbs free energy  $\Delta G(T)$  which is needed for the emission of a hole from the state. Accordingly, the activation energy of the thermal emission rate  $E_a = E_t - E_V$  in Equation (3.17) can be generalized to

$$E_a = \Delta G(T) = E_t(T) - E_V(T) \quad . \quad (3.19)$$

Using this definition of  $E_a$  and the relationship between the change of Gibbs free energy and the changes in enthalpy  $\Delta H$  and entropy  $\Delta S$

$$\Delta G(T) = \Delta H - T\Delta S \quad (3.20)$$

Equation (3.17) can be transformed to

$$e_p(T) = \chi_p \sigma_p(T) \langle v_p(T) \rangle N_v(T) \exp\left(-\frac{\Delta H}{kT}\right) \quad (3.21)$$

where  $\Delta S$  is separated from the temperature-dependent exponent as an entropy factor

$$\chi_p = \exp\left(\frac{\Delta S}{k}\right) \quad . \quad (3.22)$$

From equation (3.21) it is obvious that the measurement of  $e_p$  at various temperatures delivers data pairs which in an Arrhenius plot give a straight line with the slope  $\Delta H$ . This means that the derived activation energy of the thermal emission  $e_p$  corresponds

---

<sup>2</sup>An analogous description can also be derived for electron emission according to Equation (3.16)

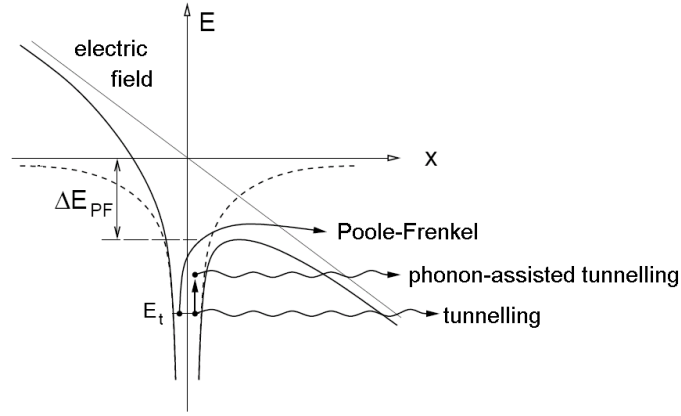


**Fig. 3.2:** The Poole-Frenkel effect: The potential barrier of a deep defect is reduced by the electric field. As a consequence, the emission rate is increased. The effect may even be pronounced by tunneling effects. From [69, p. 436]

to  $E_a = \Delta H$  instead of  $E_a = E_t - E_V$  as described above. The deviation between these both quantities depends on the temperature of the sample and the entropy  $\Delta S$  (equation (3.20)). Also the capture cross section is modified by the entropy which originates from changes in the electronic and vibronic configuration of the defect state. Thus, the axis intercept of the Arrhenius plot does not represent simply the capture cross section  $\sigma_p$  but an apparent capture cross section  $\sigma_{p,ap} = \chi_p \sigma_p$  (see [69, p. 432]).

### 3.1.2 The Poole-Frenkel Effect

When the thermal emission rate of a defect is measured in order to derive its characteristics from an Arrhenius plot, one further factor influencing the emission rate should be accounted for: The electric field in the depletion region, which in some experiments is additionally increased by an applied bias voltage, can lead to conflictive results at different measurement conditions. As shown in Fig. 3.2, the electrostatic potential binding the charge carrier to the defect center can be deformed by an electric field. As a consequence, the height and the width of the barrier gets reduced. The lowering of the barrier height increases the thermal emission rate which is known as Poole-Frenkel effect. The activation energy derived from the Arrhenius plot is then lowered by the energy  $\Delta E_{PF}$ . Another effect increasing the emission rate arises from the possibility of carriers tunneling through the narrowed barrier whereas phonon-assisted tunneling is even more probable. Thus, the latter effect is expected to occur along with the Poole-Frenkel effect already at electric fields  $> 10^4$  V/cm which can indeed exist in space charge regions. When measuring the thermal emission rate it is beneficial to choose a technique where capture and emission of traps appears significantly only at the edges of the depletion region where the field is low. Additionally, the comparison of measurements at different bias voltages allows to compare the thermal emission rates and to assess the influence of the mentioned effects [69].

## 3.2 The p-n Junction

The analytical methods used in this work rely on a fundamental knowledge of the processes within a solar cell. Especially capacitive methods take advantage of the properties of the depletion layer which develops when a contact is formed between an n- and a p-type semiconductor. Thus, the general characteristics of a p-n junction and the consequences for further considerations will be explained here briefly based on the more detailed descriptions given in [69] and [71].

Due to a high electron density on the n side and a high hole density on the p side of the junction, diffusion currents arise from the exchange of holes and electrons between both materials. A negative space charge occurs on the p side due to remaining ionized acceptors whereas a positive space charge is built up of ionized donors on the n side. The resulting electric field generates a drift current whose direction is opposing the diffusion current. An equilibrium is reached when the net current flow between drift and diffusion current at the p-n junction is equal to zero [71].

To construct the energy band diagram of a p-n junction the vacuum level is defined as reference level: It represents the energy of an electron at rest outside the material. As a material property the electron affinity of the n-type semiconductor  $\chi_n$  represents the energy required to remove an electron from the conduction band edge of the n-type material to the vacuum level. For the p-type material the corresponding electron affinity is labeled  $\chi_p$ . The thermal equilibrium of drift and diffusion currents finds its expression in a coincident Fermi level  $E_F$  on both sides of the junction. In Fig. 3.3 the resulting energy band diagram is shown. Far away from the interface the conduction and valence band energies approximate their bulk values with respect to the Fermi level [69, p. 222].

The arising built-in voltage  $V_b$  represents the potential difference induced by the electric field in the depletion region. At the edge of the depletion region where the electric field is zero the bands become flat. The width of the depletion region  $x_d$  depends on the total voltage drop across the junction and the net ionized charge density. The built-in voltage is given by the distances of the Fermi level from the conduction band edge in each material [69, p. 224]. Taking the subscripts  $n$  and  $p$  as indicators for the n- and p-sides of the junction the following can be derived from Fig. 3.3:

$$(E_C - E_F)_p + \chi_p = eV_b + \chi_n + (E_C - E_F)_n \quad . \quad (3.23)$$

In consideration of Fig. 3.3 the built-in field corresponding to the built-in voltage can be written as

$$eV_b = E_g - (E_F - E_V)_p - (E_C - E_F)_n + (\chi_p - \chi_n) \quad . \quad (3.24)$$

In the considerations above the properties of both materials are assumed to be homogeneous up to the interface, respectively. Interface charge due to defects or an interfacial layer are neglected. Nevertheless, this description turns out to be adequate for many junctions and can therefore be taken as an appropriate basis for the following considerations [69, p. 226]. In the following, a relation between the width  $x_d$  of the depletion

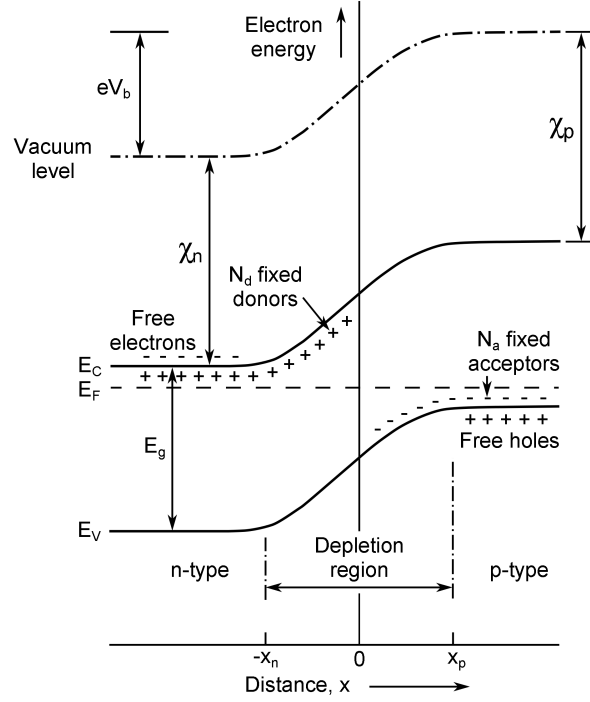


**Fig. 3.3:** Schematic energy band diagram for a p-n junction. From [69, p. 224], modified.

region will be derived in terms of the total voltage drop  $V$  across the junction. Since the latter can be increased by an applied reverse voltage  $V_a$  resulting in a widened depletion region the total voltage is defined as

$$V = V_b + V_a. \quad (3.25)$$

For reasons of simplicity, equal electron affinities  $\chi_n = \chi_p$  will be used. The starting point to find a relationship between  $x_d$  and  $V$  is given by Poisson's equation for the electrostatic potential  $\Psi$ :

$$\frac{d^2\Psi}{dx^2} = -\frac{1}{\epsilon\epsilon_0}\rho(x) \quad (3.26)$$

where  $\rho(x)$  is the charge density,  $\epsilon$  is the relative dielectric constant and  $\epsilon_0$  represents the permittivity of free space. The complete solution of this equation is accomplished in [69, pp. 226-227] and will not be outlined in detail here. However, the following assumptions and definitions have to be used as boundary conditions for the integration:

- Outside the depletion region the electric field is zero. Accordingly, the depletion layer boundaries are defined as the values of  $x$  where  $d\Psi/dx = 0$  so that  $(-x_n)$  and  $(x_p)$  are the limits of integration (see Fig. 3.3).
- The depletion region contains the same amount of positive and negative charges (charge neutrality condition).
- The band bending is defined in terms of the total voltage  $V$  relative to  $\Psi(-\infty) = 0$  as  $V = -\Psi(\infty)$ .

For a p-n junction with uniform doping concentrations  $N_a$  and  $N_d$  on each side the integration yields

$$V = \frac{e}{2\epsilon\epsilon_0} [x_p^2 N_a + x_n^2 N_d] \quad . \quad (3.27)$$

As the depletion region contains equal numbers of positive and negative charges the width of the depletion region on each side of the junction is inversely proportional to its corresponding doping concentration:

$$N_a x_p = N_d x_n \quad . \quad (3.28)$$

Using this relation together with Equation (3.27) the total width  $x_d$  of the depletion region is

$$x_d = (x_n + x_p) = \left[ \frac{2\epsilon\epsilon_0}{e} \left( \frac{N_a + N_d}{N_a N_d} \right) V \right]^{\frac{1}{2}} \quad . \quad (3.29)$$

For an abrupt asymmetric  $n^+ - p$  junction where  $N_d \gg N_a$  and according to (3.28)  $x_p \gg x_n$  the width of the depletion region can be reduced to

$$x_d = \left( \frac{2\epsilon\epsilon_0}{e N_a} \cdot V \right)^{\frac{1}{2}} \quad . \quad (3.30)$$

This expression found for  $x_d$  is based on the "full depletion" approximation: It is assumed that no free charge carriers are present in the depletion region while the bulk region is electrically neutral such that there is an abrupt transition at a distinct position  $x_d$  between both regions. Although this is an idealized scenario for the derivation, it delivers good expressions for the band bending and the width of the depletion region.

### 3.3 Space Charge Capacitance

As shown in the previous section, the width of the depletion region can be influenced by an external voltage  $V_a$  across the junction. In a  $n^+ - p$  junction the depletion region contains a fixed space charge built up mainly of ionized acceptors from the p-side. Increasing the band bending over the junction by a small amount of  $dV$  will add up fixed space charge per unit area  $dQ$ , which is identified as the small signal capacitance

$$C = A \frac{dQ}{dV} \quad (3.31)$$

with the diode area  $A$ . Accordingly, the capacitance  $C$  can be measured as a function of  $dV_a$  [69, p. 228]. Equation (3.31) states that the space charge capacitance is given by the differentiation of the total charge  $Q$  stored in the space charge region. In order to find a relation between the capacitance  $C$  and the band bending  $V$ , the charge distribution

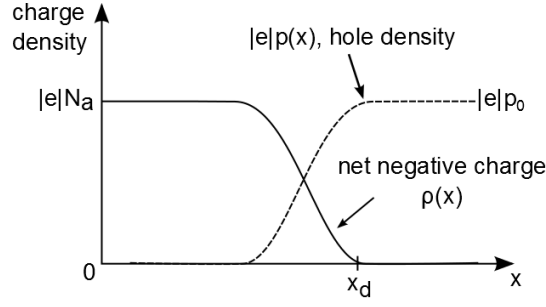


**Fig. 3.4:** Free hole distribution and net negative charge distribution  $\rho(x)$  at the edge of a depletion region in a p-type semiconductor. The spatial coordinate  $x$  indicates the distance from the contact to the n-side of the junction. From [69, p. 229], modified.

within the space charge region has to be considered. The electrostatic potential within the depletion region correlates with the valence band energy  $E_V$ :

$$-e\Psi(x) = E_V(x) - E_V(x_d) \quad . \quad (3.32)$$

As depicted in Fig. 3.4, the free hole concentration  $p(x)$  in the depletion region decreases from  $x < x_d$ :

$$p(x) = p_0 \exp\left(\frac{e\Psi(x)}{kT}\right) \quad (3.33)$$

where  $p_0$  is the free hole concentration in neutral material ( $x > x_d$ ). The net negative space charge distribution is

$$\rho(x) = e(N_a - p(x)) \quad . \quad (3.34)$$

The expressions (3.33) and (3.34) can be inserted in Poisson's equation (3.26) to calculate the electric field assuming that the acceptors are fully ionized in the neutral material, that is  $p_0 = N_a$ . As demonstrated in [69, pp. 230-231] the integration of Poisson's equation and some further calculation steps result in an expression for the total charge  $Q$  in terms of the total band bending  $V$ . By differentiation according to Equation 3.31 a relation between the capacitance and  $V$  can be derived:

$$C = A \left(\frac{\epsilon\epsilon_0 e N_a}{2}\right)^{\frac{1}{2}} \left(V - \frac{kT}{e}\right)^{-\frac{1}{2}} \quad (3.35)$$

In uniformly doped material the doping concentration  $N_a$  is given by the slope from a so called "Mott-Schottky" plot of  $C^{-2}$  against  $V_a$ . If the p-type doping is compensated by  $N_d$  donors the charge density derived from the slope is  $N_a - N_d$ . With Equation (3.25) the intercept with the  $V_a$  axis gives the built-in potential  $V_b$ . Assuming that  $V \gg kT/e$  Equation (3.35) and the equation for the width of the depletion region (3.30) can be combined to:

$$C = \frac{\epsilon\epsilon_0 A}{x_d} \quad (3.36)$$

which is consistent with the capacitance of a parallel plate capacitor. In contrast to a parallel plate capacitor, the charge  $Q$  in a depletion region does not increase linearly with the applied voltage but with  $V^{\frac{1}{2}}$  which is expressed by the differential capacitance according to (3.31). Equations (3.35) and (3.36) are the basis for the  $CV$  profiling method which will be explained in Section 4.4 in consideration of deep defects.

### 3.4 Contribution of Defects to the Space Charge Capacitance

In Section 3.2 the full depletion approximation was used for the calculation of  $x_d$ . In fact, the free charge carrier concentration decreases exponentially with the square of the distance from  $x_d$  within the depletion region (see Fig. 3.4):

$$p(x) = N_a \exp \left[ -\frac{1}{2} \left( \frac{x_d - x}{L_D} \right)^2 \right] \quad (3.37)$$

with the temperature-dependent Debye screening length

$$L_D = \left( \frac{\epsilon \epsilon_0 kT}{e^2 N_a} \right)^{\frac{1}{2}} \quad (3.38)$$

which sets the limits for a transition region where free charge carriers spill over from the bulk into the depletion region. The errors induced in the calculation of  $N_a$  and  $x_d$  by the full depletion approximation are small provided that  $V \gg (kT/e)$  and consequently  $L_D \ll x_d$ .

However, the Debye screening length is of particular importance if deep defects are present in the space charge region. This will be discussed for an  $n^+$ -p junction as depicted in Fig. 3.5 in the following. The spill over of charge carriers into the depletion region enables a finite equilibrium population probability for deep traps within the transition region  $x_d - x_1$ , where  $x_1$  denotes the intersection of the trap level and the Fermi level. When moving deeper into the depletion region where the trap level falls below the Fermi level, only a negligible number of free charge carriers (holes) is available for capture processes. In this region the occupation of deep levels is dominated by carrier emission processes [70].

Despite the charge carriers in the Debye tail, the number of free charge carriers beyond  $x_d$  is very low compared to the fixed charge from the ionized acceptors. Therefore, the space charge density in the transition region  $x_1 < x < x_d$  is  $\rho = q(N_a - N_t)$  in case of a donor-like and  $\rho = qN_a$  in case of an acceptor-like defect state. In the region  $x < x_1$  the acceptors and defect states are both ionized such that the contribution of this region to the space charge density is  $\rho = qN_a$  for a donor-like defect and  $\rho = q(N_a + N_t)$  for an acceptor-like defect. In brief, the space charge increases as soon as a defect state falls below the Fermi level regardless of whether the trap is acceptor- or donor-like. When the external bias is increased by a small amount  $\Delta V_a$  the space charge around  $x_d$  rises

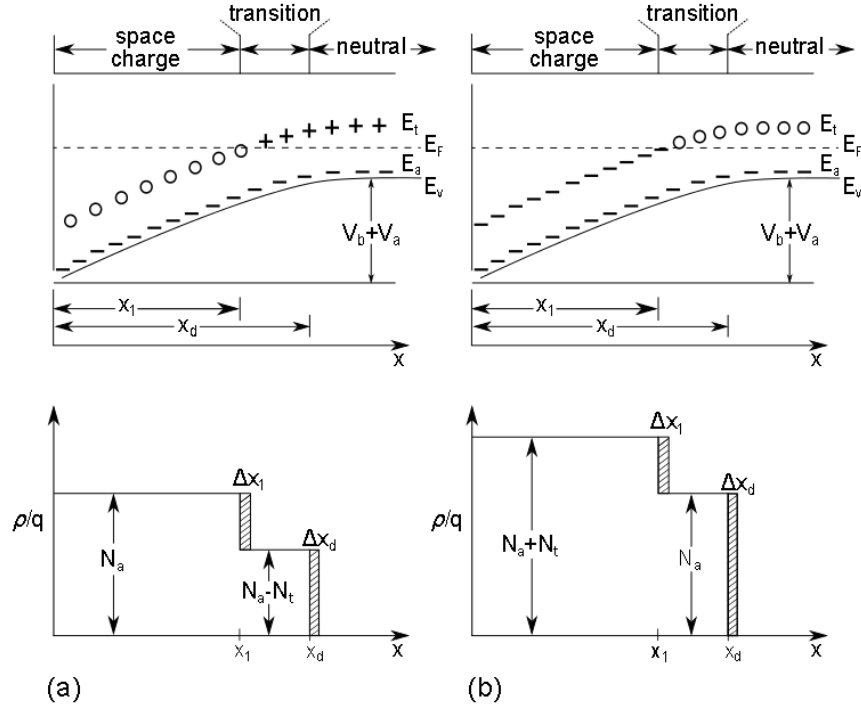


**Fig. 3.5:** Occupation of shallow acceptor levels ( $E_a$ ) and a deep donor (a) and an acceptor (b) level ( $E_t$ ), respectively, in an n<sup>+</sup>-p junction with the built-in voltage  $V_b$  and the applied reverse voltage  $V_a$ . The diagrams in the lower half illustrate the accumulated charge distribution in the depletion region given by the shallow doping density  $N_a$  up to the depletion layer edge  $x_d$ , the type of the deep defect and the intersection point  $x_1$  of its energy level with the Fermi level  $E_F$ . From [70], modified.

by  $qN_a\Delta x_d$ . If the bias is hold long compared to the inverse emission rate for holes  $e_p$  of a majority defect, the defect will be occupied by electrons during this time leading to a small increase of the space charge by  $qN_t\Delta x_d$ . By decreasing the bias, the traps will refill from holes in the Debye tail by a local capture rate  $c_p(x)$  which is equal to  $e_p(x)$  at the position  $x_1$  where the trap state intersects the Fermi level, i.e.  $E_t = E_F$ . Thus, the response of charge at the intersection point  $x_1$  to an applied alternating voltage is limited by the thermal emission rate  $e_p$ . The higher the frequency of the ac voltage the fewer charge carriers will follow.

According to Equation (3.31) changes of charge induced by changes of an applied voltage can be described by the capacitance. Consequently, the measured capacitance of a p-n junction reflects the occupation and emptying of shallow doping states at the edge of the depletion region and the charge response at the intersection points of defect levels and the Fermi level. As will be shown in the next chapter, this insight forms the basis for the capacitive methods used in this work for the investigation of defects.

# 4 Capacitance Measurement and Analytical Methods

In this chapter, the capacitive methods applied in this work and the evaluation methods linked to them are introduced. These methods make use of the space charge capacitance with regard to the contribution of defects as outlined in the previous chapter. First, the basic principle of capacitance measurements is described in Section 4.1 with regard to the equivalent circuit which is assumed for the solar cells. Thermal admittance spectroscopy (TAS) which is used for the investigation of defects in Cu(In,Ga)S<sub>2</sub> devices in this work is introduced in Section 4.2. The Meyer-Neldel rule which helps to verify a common origin for several defects and the *CV* profiling method for the derivation of apparent charge profiles are described in Sections 4.3 and 4.4, respectively.

## 4.1 Equivalent Circuits

To measure the capacitance of a p-n junction, the current response of the junction to an applied alternating voltage is analyzed regarding its angular phase shift and amplitude relative to the voltage signal. For this purpose an appropriate equivalent circuit has to be chosen for the p-n junction, which accounts for all capacitances and resistances involved. Fig. 4.1 shows one approach of an equivalent circuit. The framework is given by a capacitor of capacitance  $C_r$  and a resistor of resistance  $R_p$  connected in parallel (indicated by the conductance  $G_0 = 1/R_p$  in Fig. 4.1). While the capacitor represents the depletion region, the resistor allows for parasitic leakage currents. A resistor of resistance  $R_s$  connected in series includes the resistances originating from the semiconductor materials itself as well as ohmic contacts and wires for connecting the device to the measurement instrument. If the parallel resistance  $R_p$  is much higher than the series resistance  $R_s$ , as will also be assumed in this thesis, the series resistance can be neglected. In the remaining parallel circuit, the physical quantities capacitance and resistance are both comprised of the complex admittance  $Y$  in the imaginary part and the real part, respectively:

$$Y = i\omega C + G \tag{4.1}$$

where  $\omega$  is the angular frequency. As discussed in Section 3.4, the measured capacitance of a p-n junction includes a contribution of the fixed space charge  $C_r$  as well as a contribution arising from dynamic trap response. Losee [72] suggested that the frequency and temperature-dependent contribution of traps can be introduced by an

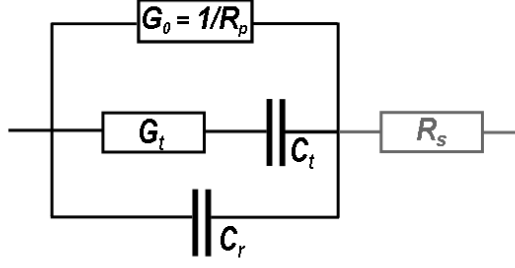


**Fig. 4.1:** Equivalent circuit for the admittance of a p-n junction. From [73], modified.

additional string parallel to the capacitor, composed of a series connection of a capacitor  $C_t$  and a conductance  $G_t$  (see Fig. 4.1). In Section 3.4 it was outlined that the contribution of defects to the capacitance is confined to frequencies which are low compared to the thermal emission rate of the defect. Therefore, the defect contribution can be considered as a low pass filter [73] whose admittance  $Y_t$  is given by

$$Y_t = i\omega \frac{C_t}{1 + i\omega \frac{C_t}{G_t}}. \quad (4.2)$$

Adding up all contributions of the parallel strings in Fig. 4.1, the admittance of the junction reads

$$Y = i\omega C_r + G_0 + i\omega \frac{C_t}{1 + i\frac{\omega}{\omega_0}} \quad (4.3)$$

where  $\omega_0 = G_t/C_t$  is defined as the cutoff frequency of the low pass filter. From this expression the real part  $G$  and imaginary part  $C$  according to Equation 4.1 can be extracted:

$$G = \text{Re}(Y) = G_0 + \frac{\omega^2 C_t^2 / G_t}{1 + \omega^2 / \omega_0^2} \quad (4.4)$$

$$C = \frac{\text{Im}(Y)}{\omega} = C_r + \frac{C_t}{1 + \omega^2 / \omega_0^2} \quad (4.5)$$

If the impedance  $Z(\omega) = 1/Y(\omega)$  is measured with an impedance analyzer which calculates the conductance  $G$  and the capacitance  $C$  under the assumption of a parallel circuit, Equations 4.4 and 4.5 can be used to analyze the frequency dependence of the capacitance and the conductance of the p-n junction [73]. The simplifying assumption of a parallel circuit can be verified by a plot of the imaginary part  $Z$  against the real part of  $Z$ , which is known as Cole-Cole plot. If the assumption is correct, the plot gives a semicircle with a diameter equal to the parallel resistance  $R_p = 1/G_0$ .

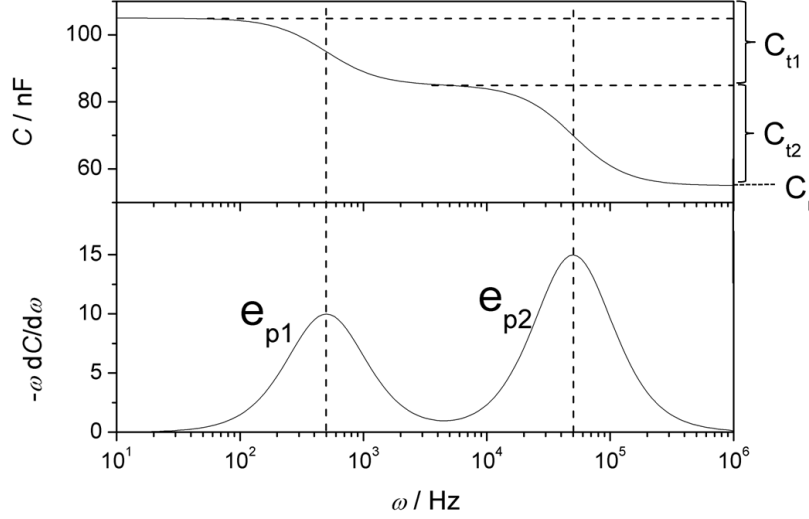


**Fig. 4.2:**  $C\omega$  spectrum including two capacitance steps with heights  $C_{t1}$  and  $C_{t2}$  evoked by two trap levels with the thermal emission rates  $e_{p1}$  and  $e_{p2}$ , respectively. The derivative representation in the lower half of the graph facilitates the read-out of the emission rates from the local maxima.

## 4.2 Admittance Spectroscopy

As described in Section 3.4 and 4.1 the capacitance contribution of a defect state which crosses the Fermi level at some location in the depletion region depends on the angular frequency  $\omega = 2\pi f$  of the applied ac voltage relative to the thermal emission rate of the defect. This circumstance allows to determine the thermal emission rate from a measurement of the admittance  $Y$  as a function of  $\omega$ . Because the imaginary part and the real part of  $Y$  are connected by the Kramers-Kronig relation, the information revealed from both quantities, the conductance  $G$  and the capacitance  $C$  is equivalent. It follows from Equations (4.4) and (4.5) that

- $\frac{G-G_0}{\omega}$  becomes maximum at  $\omega = \omega_0$ .
- $\omega \frac{dC}{d\omega}$  becomes minimum at  $\omega = \omega_0$ .

In Fig. 4.2 the angular frequency dependence of the capacitance given by Equation (4.5) is shown for the case of two defect states of different emission rates  $e_{p1}$  and  $e_{p2}$ . At low angular frequencies  $\omega < e_{p1}$  both defect states respond to the applied ac-voltage and provide the capacitance contributions  $C_{t1}$  and  $C_{t2}$ , respectively. With increasing angular frequency the capacitance decreases in two steps, where the first plateau at  $C = C_r + C_{t2}$  occurs when  $e_{p2} < \omega < e_{p1}$ , and the second plateau at  $C = C_r$  is observed when  $e_{p2} < \omega$ . In the latter frequency range only the free charge carriers at the edge of the depletion region are able to follow the alternating voltage and the spatial coordinate calculated from equation (3.36) reveals the width of the depletion region  $x_d$ . If the frequency is increased further, one more step may appear, which corresponds to the freeze-out of the mobility of the free charge carriers. Above the respective threshold frequency, the material acts as a dielectric medium and the geometrical capacitance

$C_{geo}$  is measured. For this value, equation (3.36) enables to determine the thickness of the semiconductor material. Regarding the capacitance range  $C > C_r$ , the cut-off frequency  $\omega_0$ , which can be easily derived from the plot of  $-\omega dC/d\omega$  against  $\omega$  for each trap, is related to the emission rate of the trap by

$$\omega_0 = 2e_p \left( 1 + \frac{x_1 N_t}{x_d N_a} \right) \quad (4.6)$$

in case of a p-type semiconductor [69]. If one of the ratios  $x_1/x_d$  or  $N_t/N_a$  is small, it can be assumed that  $\omega_0 \approx 2e_p$ . The height of each capacitance step relates strongly to the concentration  $N_t$  of the corresponding defect:

$$C_t = \frac{\epsilon\epsilon_0 N_t}{x_d N_a} \left( \frac{1 - x_1/x_d}{1 + (x_1 N_t)(x_d N_a)} \right) \quad (4.7)$$

If the emission rate of a defect is determined from temperature-dependent  $C(\omega)$  measurements, the activation energy  $E_a$  of the emission rate and the capture cross section  $\sigma$  can be derived from an Arrhenius plot as described in Section 3.1. The interpretation of the derived values has to be handled with care as discussed in Sections 3.1 and 3.1.1. Nevertheless both parameters,  $E_a$  and  $\sigma$ , form a signature which is commonly used to describe and compare defects.

An approach to determine the concentration of energetically continuous and spatially homogeneous distributed bulk defects has been introduced by Walter *et al.* [38]. The investigation of interface defect densities is more complicated. In contrast to a bulk defect, the activation energy  $E_a$  of the thermal emission rate depends on the energetic position of the Fermi level which is influenced by the applied bias. Furthermore, the Fermi level may be pinned by interface traps, which additionally complicates the analysis.

While the activation energy  $E_a$  derived from an admittance spectrum is related to the energetic depth of a defect, it is not directly possible to categorize the detected defects into minority or majority defects. In general, it is assumed that the detection of majority defects is more likely because an intersection of the trap state with the Fermi level is required. Indeed, if the band bending is strong enough such as in case of a type inversion close to an n<sup>+</sup>-p interface, an intersection of the Fermi level with a minority state is possible.

### 4.3 The Meyer-Neldel Rule

As mentioned in Section 3.1, the defect activation energy  $E_a$  and the capture cross section  $\sigma$  derived from an Arrhenius plot may be distorted for various reasons. These included a possible temperature dependence of  $\sigma$ , a temperature-dependent energetic distance of the defect level to the band edges (Section 3.1.1) and the Poole-Frenkel effect (Section 3.1.2). Additionally, the energetic distance of deep defect levels to the bands can depend on the ratios  $[Ga]/([Ga]+[In])$  and  $[S]/([S]+[Se])$  in  $Cu(In,Ga)(Se,S)_2$  [37].

In the application of defect spectroscopy this can complicate the analysis of the defect characteristics and the comparison of the results obtained from different samples and values taken from literature. Indeed, a wide range of activation energies is found in the literature for the signatures N1 and N2 which are frequently observed in Cu(In,Ga)Se<sub>2</sub> (see Section 2.3).

One approach to compare defect levels from different devices and to verify a common origin of these relies on the empirical Meyer-Neldel (MN) rule, which was discovered by Meyer and Neldel in 1937 [74]. This rule states that for an experimentally observed quantity  $X$  which is found to be thermally activated by

$$X = X_0 \exp\left(\frac{-\Delta}{kT}\right) \quad (4.8)$$

the activation energy  $\Delta$  is related to the pre-exponential factor  $X_0$  by

$$\ln X_0 = a + b\Delta \quad (4.9)$$

where  $a$  and  $b$  are positive constants. The MN rule has been empirically confirmed to be valid for a wide range of thermally activated processes in semiconductors. These include annealing phenomena, electronic processes in amorphous semiconductors, trapping in crystalline semiconductors and conductivity in ionic conductors ([75] and references cited there). Several authors found that the MN rule may also be helpful to assign experimentally found defect energies in different devices based on the same or similar material to a common origin and to distinguish between defects of different origin [76–79]. For this purpose, Equation (4.8) is assumed to correspond to Equation (3.18) where  $X_0$  and  $\Delta$  relate to  $\xi$  and  $E_a$ , respectively. In accordance with Equation (4.9) it is found that defects of common origin follow the relation

$$\xi = \xi_0 \exp\left(\frac{E_a}{kT_0}\right) \quad (4.10)$$

$T_0$  is the isokinetic temperature at which the various extrapolated Arrhenius plots cross. As shown by Djebbour *et. al.* [76] for data of N1 and N2 in Cu(In,Ga)Se<sub>2</sub> devices, the pre-exponential factor  $\xi_0$  relates to the "true" capture cross section  $\sigma^*$ :

$$\xi_0 = \frac{\sigma^* \langle v_{n,p} \rangle N_{V,C}}{T^2} \quad (4.11)$$

## 4.4 Capacitance-Voltage Profiling

In Section 3.3 a uniformly doped material has been assumed to connect the space charge capacitance to the total voltage drop across the junction as accomplished in Equation (3.35) which enables to calculate the doping concentration from the slope of the Mott-Schottky plot. Certainly, if the investigated material is not uniformly doped, the plot of  $C^{-2}$  over  $V$  will not give a straight line. However, it can be shown that in terms of the small signal capacitance following equation (3.31) a local doping

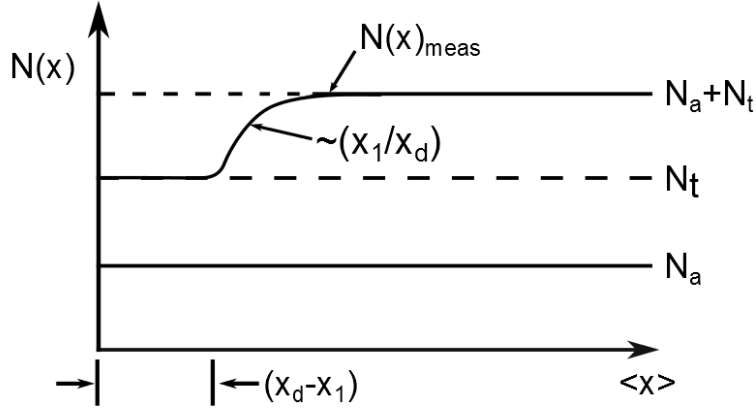


**Fig. 4.3:** Measured charge density profile  $N_{meas}$  derived from a measured  $CV$  profile on a  $n^+$ - $p$  junction in the presence of a homogeneously distributed deep acceptor level of density  $N_a$  as depicted in Fig. 3.5. Adapted from [70].

concentration  $N_a(x)$  of an  $n^+$ - $p$  junction can be derived from the local slope of the Mott-Schottky plot for each voltage [69, p. 237-240]. Thus, the measurement of the depletion capacitance by application of an ac voltage superimposed to a dc bias sweep enables to determine a depth profile  $N_a(x)$ , where the spatial coordinate can be calculated by means of equation (3.36).

Indeed, from the discussion in Section 3.4 it becomes clear that for low ac voltage frequencies the derived charge density  $N_a$  does not simply represent the doping density but is increased by a contribution arising from a dynamic trap response. Furthermore, the calculated spatial coordinate of the profile is distorted due to the participation of defects resulting in an additional capacitance contribution. It no longer represents the edge of the depletion region  $x_d$  but rather an average value  $\langle x \rangle$ . The magnitude of the distortion of the profile depends on the applied ac frequency of the voltage in regard to the thermal emission rate of the concerned defect state which correlates with the measurement temperature and the energetic depth in the band gap. By choosing a sufficiently high ac frequency and a low temperature the thermal emission rate of defect states can be held low and therefore the derived values for  $N_a$  and  $\langle x \rangle$  correspond mostly to the real values of the doping profile.

But even if the capacitance is measured at ac-voltage frequencies  $\omega(\Delta V_{ac}) > e_p$  the derived profile only reflects an apparent doping concentration  $N$  (referred to  $N_{meas}$  in Fig. 3.5) instead of the pure shallow doping density. This is because the measured capacitance depends on the change of the entire charge in the intervals  $\Delta x_d$  and  $\Delta x_1$  which also includes the static charge induced by ionized deep acceptors and donors (see Fig. 3.5). Assuming that the voltage sweep applied for scanning the spatial doping density is performed slowly compared to  $e_p^{-1}$ , the occupation of traps will correspond to each individual band bending caused by every single voltage step. Thus, in an  $n^+$ - $p$  junction the doping originating from shallow acceptor states can be compensated by donor-like deep levels located above the Fermi level. On the other hand, acceptor-like deep levels can increase the effective doping as long as they are occupied by electrons.

Consequently, the effective doping density derived from a Mott-Schottky plot in the presence of an acceptor trap is given by

$$N(x_d) = [N_a(x_d) - N_d(x_d)] + \frac{x_1}{x_d} \cdot N_t(x_1) \quad (4.12)$$

where  $N_d(x_d)$  represents donor traps in the upper half of the band gap which do not intersect the Fermi level and whose occupation is independent of  $x$  [69, p. 298-302]. The presence of a donor trap leads to

$$N(x_d) = [N_a(x_d) - N_d(x_d) - N_t(x_d)] + \frac{x_1}{x_d} \cdot N_t(x_1) \quad (4.13)$$

When the reverse bias is increased,  $x_1/x_d$  gets larger such that the analysis of the  $CV$  measurement reveals an increase in doping density even though the doping and trap levels are both uniform. This is valid irrespective if the trap is acceptor- or donor-like. In Fig. 4.3 the effect is illustrated for the case of an acceptor trap.

From these considerations it becomes clear that the interpretation of doping profiles derived from  $CV$  measurements has to be handled with care. An increase in the doping profile to higher values of  $\langle x \rangle$  cannot necessarily be attributed to a gradient in the doping or defect profile. Furthermore, the shape of the profile and the calculated  $\langle x \rangle$ -axis can depend on the applied ac-frequency. Nevertheless, as will be shown in Section 6.3.1, this frequency-dependent behavior can be valuable to assess the influence of individual defects on the space charge capacitance.



# 5 Investigated Samples

In this chapter, details of the samples investigated in this work are shortly described. An overview of the investigated Cu(In,Ga)S<sub>2</sub> samples processed by different RTP parameters is given in Section 5.1 and a method for sample contacting which facilitates extensive measurement series is introduced in Section 5.2.

## 5.1 Overview of Investigated Samples

The samples investigated in this work were provided by the Helmholtz Zentrum Berlin (HZB) and the Soltecture GmbH (formerly Sulfurcell GmbH). A detailed overview of these samples including labeling, absorber material and temperature profile during sulfurization is given in Table 5.1. The Cu(In,Ga)S<sub>2</sub> samples from HZB were processed on small substrates (5 × 5 cm<sup>2</sup>) by using various process parameters and are denoted by the following nomenclature:

H	Ga-doped sample fabricated by HZB
1/ 2/ 3	one/ two/ three temperature steps during sulfurization
HT/ LT	high/low sulfurization top temperature
VT	various temperatures: laterally inhomogeneous temperature distribution during sulfurization impedes assignment of temperature
H*T	particularly high sulfurization temperature: Since the temperature profile during processing these samples involved rather increasing and decreasing temperature gradients than stable temperatures, the sulfurization steps in Table 5.1 are referred to "ramp to...".
(no)	sample number

It should be mentioned that the temperatures given in Table 5.1 only refer to nominal temperatures during the sulfurization process which do not necessarily correspond to the real substrate temperature and can not be assumed to be homogeneous over the complete substrate including several samples. The latter could especially be verified for the sample series denoted by H2VT and H3VT by a gradient in the minimum band gap energy  $E_{g,min}$  and the  $V_{oc}$  from sample to sample within one batch. However, this inhomogeneity provides a variety of samples with different  $E_{g,min}$  according to different

**Table 5.1:** Denotation of  $\text{CuInS}_2$  and  $\text{Cu(In,Ga)S}_2$  samples processed with varied RTP parameters provided by Soltecture and HZB.

	sample name	material	sulfurization steps
HZB	H2HT-(no)	$\text{Cu(In,Ga)S}_2$	250 °C (3 min), 600 °C (3 min)
	H1HT-(no)	$\text{Cu(In,Ga)S}_2$	600 °C (5 min)
	H2LT-(no)	$\text{Cu(In,Ga)S}_2$	250 °C (3 min), 540 °C (3 min)
	H2VT-(no)	$\text{Cu(In,Ga)S}_2$	250 °C (3 min), 600 °C (3 min)
	H3VT-(no)	$\text{Cu(In,Ga)S}_2$	250 °C (3 min), 620 °C (10-15 sec), 560 °C (3 min)
	H3HT-(no)	$\text{Cu(In,Ga)S}_2$	280 °C (3 min), 730 °C (10 sec), 580 °C (3 min)
	H3H*T-(no)	$\text{Cu(In,Ga)S}_2$	ramp to 620 °C (3 min), 850 °C (40 sec), ramp to 649 °C (1 min)
	Soltecture	SOG-(no)	$\text{Cu(In,Ga)S}_2$
SO-(no)		$\text{CuInS}_2$	confidential

Ga concentrations at the absorber surface. This enables a systematic investigation of the influence of Ga on the performance and defect characteristics. The reader should keep in mind, that results derived for individual samples in this work cannot be generally transferred to other samples obtained from the same nominal RTP process.

The  $\text{CuInS}_2$  and  $\text{Cu(In,Ga)S}_2$  samples from Soltecture were cut out of large-scale modules. Compared to the HZB samples these devices are rather homogeneous regarding their performance characteristics and only one RTP process per absorber type is investigated in this work. Their denotation is given by the following:

SO/ SOG    Ga-free/ Ga-doped sample fabricated by Soltecture

(no)        sample number

The Solteature samples are also compared in terms of the influence of Ga on the parameters of interest. Due to the company secret the exact RTP parameters of these samples are not disclosed which is irrelevant since no different RTP processes are compared.

## 5.2 Sample Contacting

Several samples were investigated by an extended measurement series in this work which implicated repeated contacting of each sample. Since the layers of the solar cells are sensitive to mechanical stress applied by the use of needles or spring-loaded pins for contacting the grid, an alternative contacting approach was required to avoid the generation of shunts.

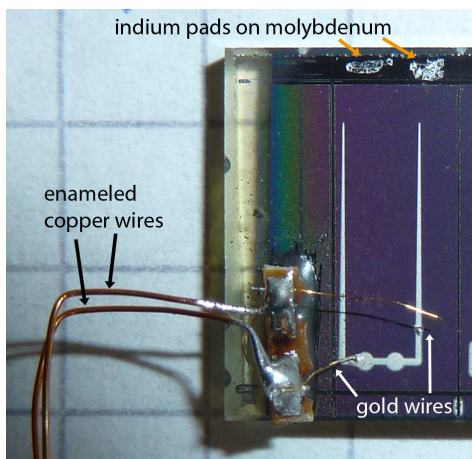


**Fig. 5.1:** HZB sample provided with contacts which were fixed with a conductive adhesive on the grid. Detailed description is given in the text.

This was achieved by sticking a small piece of blank on the substrate next to the solar cell on which two 50  $\mu\text{m}$  thin gold wires and two more robust enameled copper wires were soldered (Fig. 5.1). The gold wires were fixed on the grid with a conductive adhesive based on a silver filled modified polycarbamin acid derivative which had to be cured at 80  $^{\circ}\text{C}$  for 30 minutes. For repeated contacting, the enameled copper wires could be connected by additional cables. To connect the back contact, two indium pads were attached to the bare molybdenum which were contacted by conventional needles or spring-loaded pins.

This approach does not just prevent mechanical stress to the film but also allows for a reduced shading compared to conventional contacting methods and provides constant contact positions on the grid which offers an optimized reproducibility of the measurements. Nevertheless, the quality of the contacts on the grid may vary with regard to the series resistance. This has to be considered especially in the evaluation of the forward current from which the saturation current density  $J_0$  and the diode quality factor  $A$  can be derived as described in [80]. An example for the influence of the contact quality on the forward current corrected by the parallel resistance  $R_p$  is demonstrated in Fig. 5.2. Upon improving the contact, the analysis of the slope at  $V = 750\dots 850$  mV

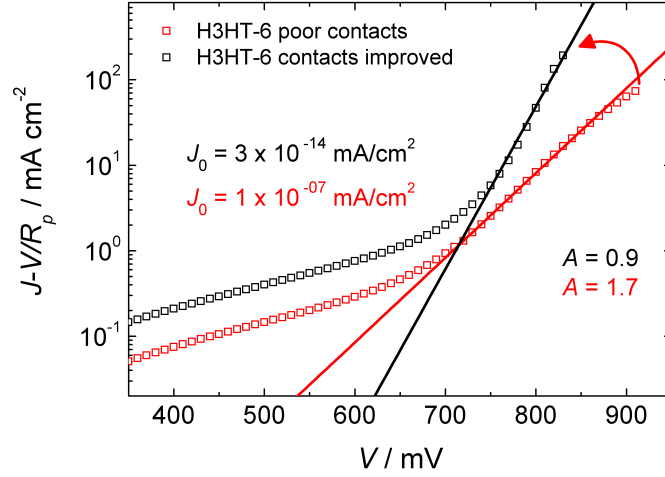


**Fig. 5.2:**  $IV$  curves of the HZB sample H3HT-6 with poor contacts and improved contacts, measured at 300 K in the dark as part of an  $IVT$  measurement. The poor contacts result in a higher series resistance and therefore in a higher diode quality factor  $A$  as derived from a fit at  $V = 750\dots850$  mV. The assignment of sample IDs is given in Table 5.1.

and the current-axis intercept results in decreased  $A$  and  $J_0$  values, respectively. Where possible, the  $IV$  curves discussed in this work are corrected by  $R_s$ . However, most of the parameters which will be discussed are not affected by  $R_s$ . These include the open circuit voltage  $V_{oc}$ , the minimum band gap energy  $E_{g,min}$ , the defect activation energy  $E_a$  and the activation energy of the saturation current  $E_A$ .

# 6 Results and Discussion

In the following sections the results of this thesis are presented and discussed. The key objective is to understand the influence of Ga on the device parameters and the defect spectrum of Cu(In,Ga)S<sub>2</sub> solar cells. Section 6.1 focuses on the impact of Ga on the  $V_{oc}$  and the band gap widening at the interface as well as the identification of the  $V_{oc}$ -limiting recombination process. In Section 6.2 the defect spectra of samples with different Ga depth profiles are examined. The evaluated signatures are compared to those known from Cu(In,Ga)Se<sub>2</sub> solar cells and conclusions are drawn on the influence of Ga on the energetic position of the conduction and valence band in sulfur-based devices. The aim of Section 6.3 is to verify if specific signatures can be associated with the often discussed N1 level (see Section 2.3), which commonly occurs in selenium-based devices, and to find out if they can be assigned to interface defects. For this purpose, the results of air annealing experiments and  $CV$  profiling at selective frequencies are presented and discussed.

## 6.1 Basic Characterization

In this section the fundamental properties of the differently RTP-processed samples introduced in Section 5.1 are presented. The discussion includes results obtained from external quantum efficiency ( $EQE$ ) spectra, energy dispersive X-ray spectroscopy (EDX), current-voltage ( $IV$ ) characteristics at standard test conditions<sup>1</sup> (STC) as well as the temperature dependence of current-voltage characteristics ( $IVT$ ). A detailed description of these methods is given in [71, 80] ( $EQE$ ,  $IV$ ), [81] (EDX) and [5, 61, 82] ( $IVT$ ). Within this work, the parameter of main concern derived from  $IV$  curves is the open circuit voltage  $V_{oc}$  while the results from  $IVT$  measurements additionally deliver essential insight into the dominant recombination process in the samples. The high voltage limit introduced in Section 2.4 is exemplified by comparison of the minimum band gap energies  $E_{g,min}$  derived from the  $EQE$  spectra and the  $V_{oc}$ -values of the corresponding devices. In this context, the influence of the process parameters and the Ga content at the heterointerface on the results obtained from  $IV$ ,  $IVT$  and  $EQE$  measurements is discussed. To assess the correlation of the Ga depth profiles in the absorber with the measurement results, EDX line scans of the absorber cross sections are utilized. Although capacitance-voltage ( $CV$ ) measurements could also be regarded as a standard characterization tool, the results obtained from this method will be individually presented in Section 6.3 since the measurement conditions were chosen based on the findings of the thermal admittance spectra evaluated in Section 6.2.

---

<sup>1</sup>1000 W/m<sup>2</sup> irradiance, 25 C sample temperature and AM1.5 spectrum

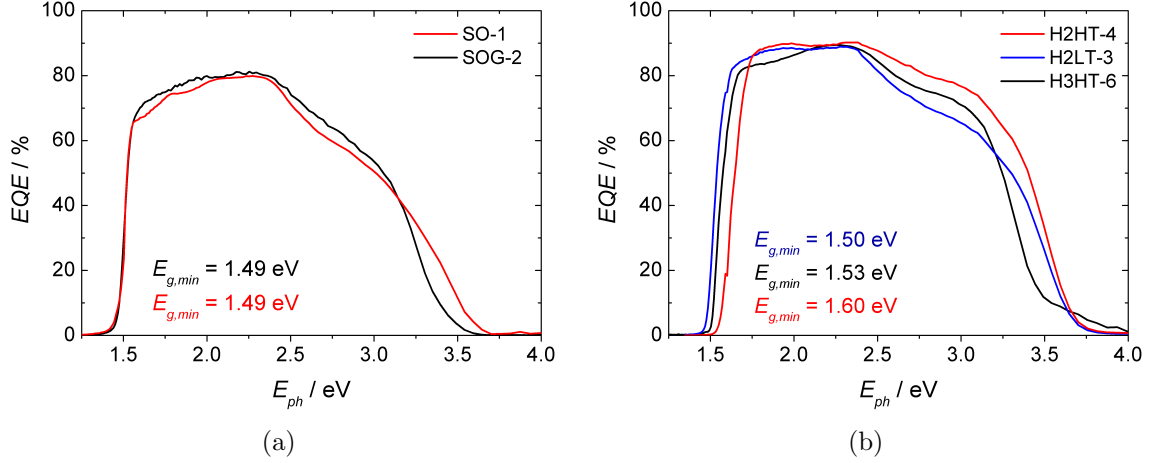


**Fig. 6.1:** (a)  $EQE$  spectra for exemplary Ga-free (SO-1) and Ga-doped (SOG-2) samples from Soltecture. (b)  $EQE$  spectra for Ga-doped HZB samples processed by 2 and 3 sulfurization steps, respectively. The assignment of sample IDs is given in Table 5.1.

### 6.1.1 EQE Spectra and IV Characteristics

External quantum efficiency spectra reflect the spectrally resolved contributions of the incident photon flux to the short circuit current density  $J_{sc}$ . Before being absorbed in the  $\text{Cu}(\text{In,Ga})\text{S}_2$  absorber, the photons have to pass the  $\text{ZnO}:\text{Al}/\text{i-ZnO}$  window and the  $\text{CdS}$  buffer layer. Photons with energies  $E_{ph}$  above the band gap energies of the window and the buffer layer are not collected and therefore do not contribute to the photocurrent. Furthermore, the band gap energy of the absorber determines the threshold energy for photons that can be effectively absorbed. Since a Ga gradient within the absorber induces a band gap gradient, the onset of the  $EQE$  spectrum at low  $E_{ph}$  indicates the minimum band gap  $E_{g,min}$  existing in the absorber material. Within this work,  $E_{g,min}$  is determined from a linear extrapolation of the squared  $EQE$  at the intersection point with the photon energy axis. This approach is motivated by the proportionality between the absorption coefficient and the square root of the photon energy for direct semiconductors.

Fig. 6.1 shows the  $EQE$  spectra of samples with different Ga-concentrations at the heterocontact. In Fig. 6.1 (a) the spectral response of a Ga-free and a Ga-doped sample from Soltecture is compared. For the  $EQE$  spectra of HZB samples as presented in Fig. 6.1 (b) the impact of Ga shall be discussed by means of different temperature profiles during the RTP process. The denotation of the samples contains informations on the manufacturer and the temperature profile as listed in Table 5.1.

The maximum  $EQE$  of both Soltecture samples SO-1 and SOG-2 in Fig. 6.1 (a) is considerably lower than the  $EQE$  of the HZB samples as shown in Fig. 6.1 (b). It should be noted, that the  $EQE$  was found to be laterally inhomogeneous for both, the Soltecture and the HZB samples. For the Soltecture samples,  $EQE$  spectra with up to 85 % could be detected at some positions, but these represent rather exceptional cases than representative data compared to those chosen for Fig. 6.1 (a). A reduced  $EQE$

over the whole energy range can be caused by optical losses due to reflection from the cell's surface and internal interfaces as well as a high interface recombination velocity [80, 83]. In the photon energy range between the Cu(In,Ga)S<sub>2</sub> absorption edge and the CdS absorption edge at  $E_{ph} = 2.40$  eV the  $EQE$  descends from high to low  $E_{ph}$  in case of the Solteature samples whereas it is more uniform in case of the HZB samples. The reduction of the  $EQE$  for low-energy photons may result from a reduced diffusion length of minority charge carriers generated deeper within the absorber layer [80].

In the following, the focus of the discussion will be on the changes in  $E_{g,min}$  evoked by different Ga-concentrations at the heterocontact and its impact on the  $V_{oc}$ . Despite of the above mentioned lateral inhomogeneities of the spectral response,  $E_{g,min}$  can be considered to be a reliable parameter. Nevertheless, EDX line scans will serve to verify the statements that will be made based on  $E_{g,min}$ .

As indicated in Fig. 6.1 (a), the onset of the spectral response does not differ significantly between the Ga-doped and the Ga-free sample. For both devices the minimum band gap energy amounts to  $E_{g,min} = 1.49$  eV which corresponds to the band gap energy of pure CuInS<sub>2</sub>. According to the explanation given in Section 2.5, the low band gap energy  $E_{g,min}$  of sample SOG-2 is probably caused by a top temperature that was too low to enable the diffusion of Ga towards the heterointerface. The same conclusion results from the rather low value  $E_{g,min} = 1.50$  eV of the HZB sample H2LT-3 (see Fig. 6.1 (b)). However, the insufficient diffusion of Ga to the heterocontact has to be verified later in this section by means of EDX line scans. The higher sulfurization temperatures used for processing the samples H3HT-6 and H2HT-4 obviously allowed for some interdiffusion of CuInS<sub>2</sub> and CuGaS<sub>2</sub> throughout the absorber layer. This is indicated by the minimum band gap energies of these samples which amount to  $E_{g,min} = 1.53$  eV and  $E_{g,min} = 1.60$  eV, respectively.

The absence of Ga at the heterointerface of sample H2LT-3 could also provide an explanation for the lower  $EQE$  at  $E_{ph} > 2.40$  eV. Following the statements given by Merdes *et al.* [67, 84] the crystal growth kinetics of CdS may depend on the Ga content at the Cu(In,Ga)S<sub>2</sub> surface. As a consequence, also the growth of the ZnO:Al/i-ZnO layer and thereby its absorption characteristics could be modified <sup>2</sup>. This correlation between the presence of Ga at the buffer/absorber interface and the spectral response at energies  $E_{ph} > 2.40$  eV may also be concluded from the spectra of the Solteature samples although it was stated above, that no Ga is expected at the heterointerface of sample SOG-2.

At  $E_{ph} \approx 2.0$  eV the  $EQE$  for sample H3HT-6 exhibits a step which indicates that there are less regions with band gap energies  $E_g < 2.0$  eV compared to the 2-step RTP-processed samples. This band gap gradient could exist laterally within the Cu(In,Ga)S<sub>2</sub> layer due to inhomogeneously sputtered precursors or growth kinetics during the RTP process on the one hand or within the depth of the Cu(In,Ga)S<sub>2</sub> layer due to a gradient in the Ga depth profile on the other hand.

---

<sup>2</sup>Different absorption characteristics of the ZnO:Al/i-ZnO layers may also exist due to deviations in its doping properties. Detailed information about the process parameters of individual ZnO:Al/i-ZnO layers are not known to the author.

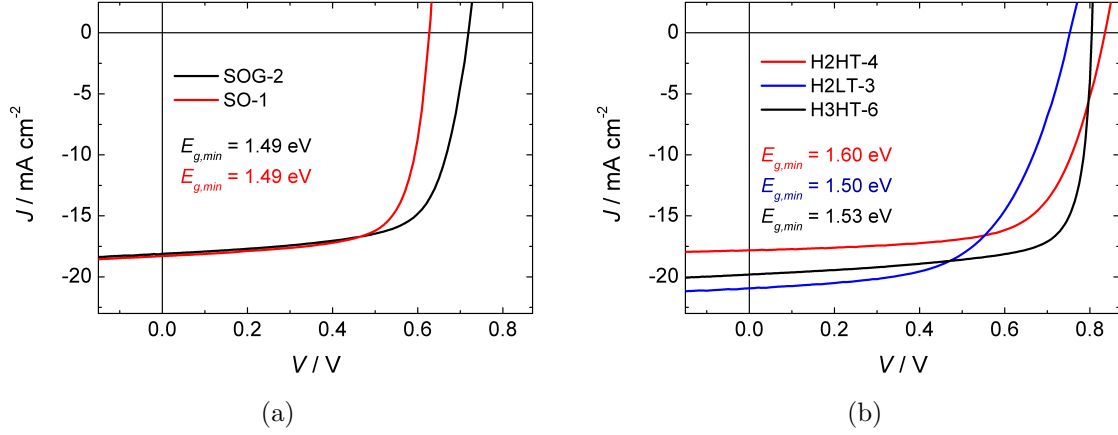


**Fig. 6.2:** (a)  $IV$  characteristics for Soltecture samples with  $\text{CuInS}_2$  and  $\text{Cu(In,Ga)S}_2$  as absorber material. (b)  $IV$  characteristics for HZB samples processed by 2 and 3 sulfurization steps, respectively. The assignment of sample IDs is given in Table 5.1.

The  $IV$  characteristics<sup>3</sup> presented in Fig. 6.2 correspond to the samples discussed above and reflect the impact of Ga incorporation on the open circuit voltage. Compared to the Ga-free Soltecture sample SO-1 the  $V_{oc}$  of the Ga-doped sample SOG-1 is increased by 91 mV (Fig. 6.2(a)). This is a surprising result because the corresponding  $EQE$  spectrum did not confirm a shift of  $E_{g,min}$ . Indeed, an increase of the band gap close to the heterojunction would enable a larger splitting of the quasi-Fermi levels which sets the upper limit for the  $V_{oc}$ . It should also be noted, that the  $V_{oc}$  for the SO sample is quite low compared to results reported elsewhere for solar cells with pure  $\text{CuInS}_2$  as absorber material [85], whereas the  $V_{oc}$  obtained for the Ga-doped sample is much closer to these values. Therefore, the reason for the higher  $V_{oc}$  in the SOG sample could be a reduced recombination velocity in the space charge region and/or at the heterointerface instead of a widened interface band gap.

In contrast to the Soltecture samples a correlation between  $E_{g,min}$  and the  $V_{oc}$  is obvious for the HZB samples, as depicted by the  $IV$  characteristics in Fig. 6.2 (b). While the increase in  $V_{oc}$  with increasing  $E_{g,min}$  can be explained with an enhanced Ga-concentration at the heterojunction, the decrease in  $J_{sc}$  with increasing  $E_{g,min}$  results from absorption losses at lower photon energies  $E_{ph}$ .

To assess the Ga depth distribution and thereby the band gap energy at the buffer/absorber interface, EDX line scans were performed at random positions of the device cross sections in a field-emission SEM. The band gap profiles were calculated from the Ga profiles as explained in [86]. Where possible, the same samples from which the  $IV$  and  $EQE$  results are discussed above were chosen. Otherwise, for example if complicated by affixed contacts on the original sample, a sample from the same RTP process with comparable characteristics was selected.

Fig. 6.3 (a) shows the calculated band gap gradings for three different positions along

<sup>3</sup>While the current density  $J$  (normalized to the sample area) is shown in the graphs, the standard terms "current-voltage ( $IV$ ) measurements/ curves/ characteristics..." are used in the text.

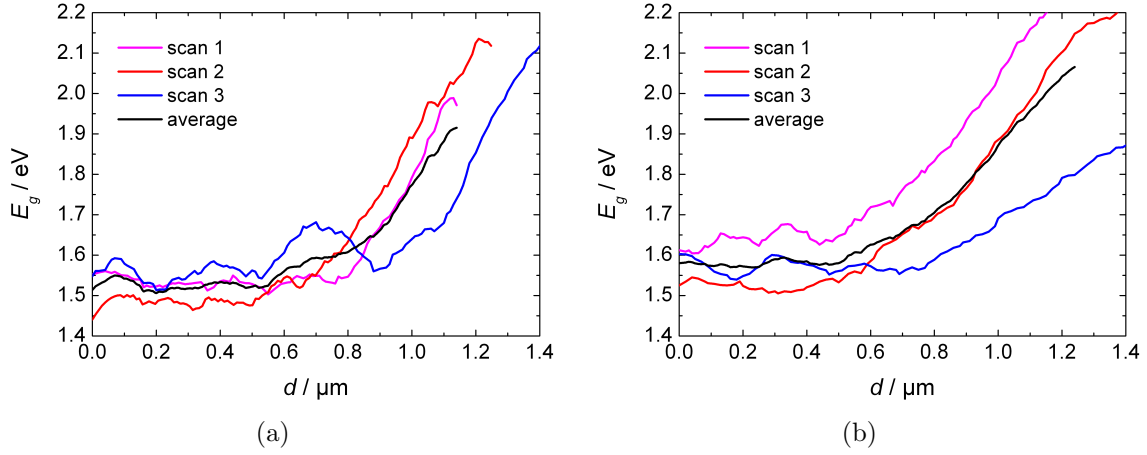


**Fig. 6.3:** (a)  $E_g$  depth profiles calculated from EDX scans for sample SOG-7 and (b)  $E_g$  depth profiles calculated from EDX scans for sample H2LT-3.  $d$  denotes the distance from the CdS buffer layer. The assignment of sample IDs is given in Table 5.1.

a cross section of a SOG sample with  $IV$  and  $EQE$  characteristics very similar to that of SOG-2. The profiles reveal that most of the Ga is located towards the back contact, whereas its concentration decreases gradually towards the interface as a consequence of the RTP process. It is also demonstrated that the Ga-distribution varies strongly between different scan positions. However, the assumption that no Ga reached the heterointerface, which was concluded from the low  $E_{g,min} = 1.49$  eV, cannot be confirmed. On the other hand, the strong variation of  $E_{g,min}$  suggests that there are probably sufficient Ga-free regions in the absorber which account for the mean value of  $E_{g,min}$  equal to that of the Ga-free SO samples.

In Fig. 6.3 (b) EDX scans performed on the sample H2LT-3 are presented. Also for this sample, a strong band gap gradient from the back contact towards the interface and varied band gap energies at the absorber surface are observed. Similar to the results obtained for the SOG-7 sample, the band gap energy close to the heterojunction is mostly higher than  $E_g = 1.50$  eV at least in the regions investigated. As also argued for sample SOG-2, this finding disagrees with the minimum band gap energy  $E_{g,min} = 1.50$  eV derived from the  $EQE$  spectrum. Accordingly, the same argument as used for sample SOG-2, namely the presence of Ga-free regions evoking the low  $E_{g,min}$  value can be considered to explain this deviation.

The band gap profiles for several Ga-doped samples, including H2LT-3 and SOG-7, derived from averaging two or three EDX-scans per sample are presented in Fig. 6.4 (a). From these profiles the average minimum band gaps  $\overline{E}_{g,front}$  within the flat region of the profile close to the absorber surface were calculated and compared to  $E_{g,min}$  from  $EQE$  spectra and to  $V_{oc}$  in Fig. 6.4 (b). For all investigated samples the  $\overline{E}_{g,front}$  values are higher than the respective  $E_{g,min}$  values. This complements the observations for sample H2LT-3 and SOG-7 and suggests that  $E_{g,min}$  generally does not reveal the average minimum band gap energy with regard to the depth profile but rather accounts for regions where only a small Ga-concentration exists.

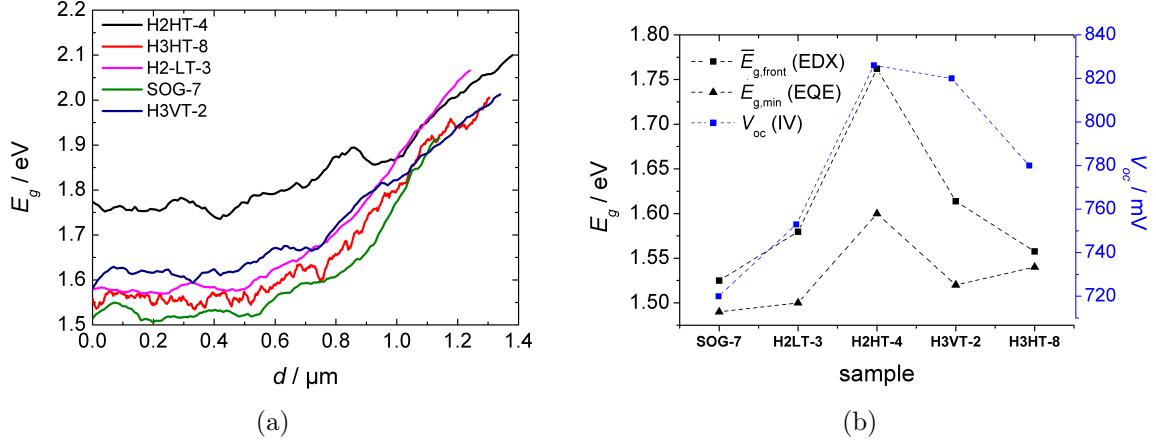


**Fig. 6.4:** (a) Averaged  $E_g$  depth profiles calculated from two or three EDX cross sectional line scans for each sample. (b) Comparison of values for  $E_{g,min}$  derived from  $EQE$  spectra,  $\bar{E}_{g,front}$  derived from EDX scans and  $V_{oc}$  determined by  $IV$  measurements. The assignment of sample IDs is given in Table 5.1.

In case of sample SOG-7 and the 2-step RTP-processed samples H2HT-4 and H2LT-3 both band gap energies  $E_{g,min}$  and  $\bar{E}_{g,front}$  follow the trend of the  $V_{oc}$  while such behavior cannot be observed in case of the 3-step processed samples H3VT-2 and H3HT-8. Especially for sample H3VT-2 the  $V_{oc}$  is remarkably high related to its relatively low band gap energy close to the heterointerface. This specific feature becomes more evident in Fig. 6.5 where the  $V_{oc}$  is plotted against  $E_{g,min}$  from  $EQE$  for numerous samples of all types investigated in this work. For six samples stemming from 3-step RTP-processed HZB samples with  $E_{g,min} = 1.52 - 1.54$  eV the  $V_{oc}$  is found to be distinctly higher than expected for the respective  $E_{g,min}$  if the trend of the remaining data is considered as a reference. These conspicuous samples are highlighted by a blue shade to distinguish them from other 3-step processed samples which do not show this specific feature. For the samples with  $E_{g,min} > 1.6$  eV the open circuit voltage seems to approach  $V_{oc} \approx 820$  meV except for three samples, highlighted by a gray shade. These samples experienced a very high short-term sulfurization temperature during the RTP process (H3H\*T), similar to the 3-step processed samples, resulting in a significantly improved  $V_{oc}$  related to the trend described above. Nevertheless, the open circuit voltages of these samples are not in line with the high  $V_{oc}$  values obtained with the 3-step process for the six special samples at  $E_{g,min} = 1.52 - 1.54$  eV.

The lowest  $V_{oc}$  values are found for the Solteature  $\text{CuInS}_2$  samples which significantly deviate from the trend established by the rest of the data. In contrast, the SOG samples with the same  $E_{g,min}$  adopt quite well to the trend. However, Fig. 6.5 also demonstrates that a large discrepancy between the measured  $V_{oc}$  and those values extrapolated from  $\text{Cu(In,Ga)Se}_2$  champion cells (dashed line) is still present and that the 3-step RTP process shows a great promise for closing a part of this gap. Consequently, it is worthwhile to consider the reason for the phenomenon that for some samples the  $V_{oc}$  is higher than that observed for other samples with the same or similar  $E_{g,min}$ .

One possible factor influencing the  $V_{oc}$  is the Ga-distribution throughout the absorber

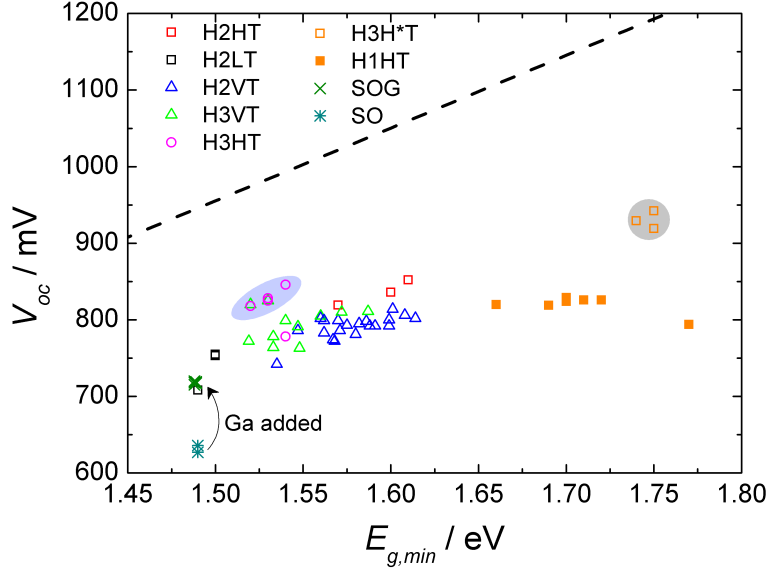


**Fig. 6.5:**  $V_{oc}$  versus  $E_{g,min}$  for samples studied in this work. The blue shade marks samples from a 3-step RTP process which revealed particular high  $V_{oc}$  values. Samples from the H3H\*T process are marked by a gray shade. The dashed line represents extrapolated data of Cu(In,Ga)Se<sub>2</sub> champion solar cells [56]. The assignment of sample IDs is given in Table 5.1.

material. In principle,  $E_{g,min}$  does not reveal the spatial position of the minimum band gap and in the foregoing discussion it has just been presumed that it is located at the heterojunction as a logical consequence of the RTP process. Indeed, a V-shape formed in the Ga profile has been previously observed for RTP-processed samples [13] but such a shape did not appear in the EDX scans performed in this work. It should be mentioned that due to the limited number of line scans it can not be excluded that there are regions with a V-shaped Ga profile. Apart from that, the Ga-concentration at the heterojunction is presumably rather randomly distributed. While individual regions with low Ga concentrations at the heterointerface may account for the low  $E_{g,min}$ , the improved  $V_{oc}$  value could be evoked by a higher value  $E_g$  averaged over all interface positions.

An increased Ga content at the back contact has been shown to be beneficial regarding the  $V_{oc}$  [87] as it repels electrons diffusing towards the back contact and thereby prevents interface recombination at the back contact. At least for the SOG samples the accumulated Ga at the back contact could be responsible for the higher  $V_{oc}$  values compared to the Ga-free SO samples due to reduced interface recombination at the back contact. For the HZB samples this effect should be less significant since these cells generally exhibit a pronounced Ga grading towards the back contact. Furthermore, a back surface grading should mainly increase the  $J_{sc}$  as a consequence of an improved charge carrier collection especially for such carriers generated by low photon energies close to the back contact [88]. However, such an effect cannot be concluded from the shape of the corresponding  $EQE$  spectra shown in Fig. 6.1 (a).

An excess forward current density has been identified by Sites *et al.* [89] to be responsi-

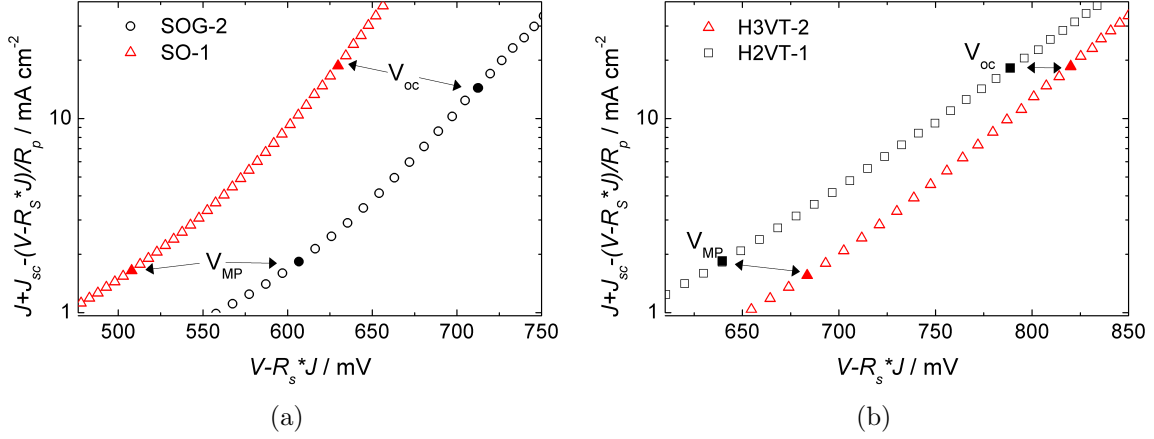


**Fig. 6.6:** Comparison of the forward current density corrected by  $J_{sc}$ ,  $R_s$  and  $R_p$  for (a) Soltecture samples with  $\text{CuInS}_2$  and  $\text{Cu(In,Ga)S}_2$  absorber and for (b) a 2-step and a 3-step processed HZB sample. The assignment of sample IDs is given in Table 5.1.

ble for a reduced  $V_{oc}$  and a reduced fill factor in polycrystalline solar cells as compared to monocrystalline solar cells with similar band gaps. Recombination of electrons and holes via defect states in the depletion region is a fundamental mechanism increasing the forward recombination current which is regulated by the saturation current density  $J_0$  and the quality factor  $A$  of the diode. The authors concluded that the reduction of recombination at grain boundaries should be the major task to achieve high efficiencies in polycrystalline solar cells. Indeed, Contreras *et al.* [10] could assign a reduced  $J_0$  correlated with an improved  $V_{oc}/E_g$  ratio of their wide-gap  $\text{Cu(In,Ga)Se}_2$  solar cells to a change in defect characteristics at grain boundaries.

In Fig. 6.6 (a) the forward current density derived from illuminated  $IV$  curves corrected for  $J_{sc}$  and resistive losses is compared for a Ga-doped and a Ga-free Soltecture sample of equal minimum band gap energy  $E_{g,min} = 1.49$  eV. An equivalent representation is shown in Fig. 6.6 (b) for HZB samples from a 3-step and a 2-step RTP process. Despite its higher minimum band gap value  $E_{g,min} = 1.55$  eV, the  $V_{oc}$  of sample H2VT-1 is smaller compared to the  $V_{oc}$  of sample H3VT-2 with  $E_{g,min} = 1.52$  eV. For both, the Soltecture and the HZB samples, a reduced forward current density coincides with higher  $V_{oc}$ -values of samples H3VT-2 and SOG-2. In case of the HZB sample also the fill factor is slightly increased, indicated by a larger difference between the voltages of the maximum power points  $V_{MP}$  compared to the difference between the  $V_{oc}$ -values. This correlates with a higher slope of the forward current density of sample H3VT-2 indicating a lower diode quality factor  $A$ . Furthermore, the data indicate that the saturation current density  $J_0$  of sample H3VT-2 is lower than  $J_0$  of sample H2VT-1 which points to reduced recombination losses and could reason the improved  $V_{oc}$ . An oppositional relationship is found for the Soltecture samples: Sample SOG-2 with the higher  $V_{oc}$ -value has a larger diode quality factor and an increased  $J_0$ -value compared to sample SO-1. This is contradictory to the decrease in forward current density and the increase in  $V_{oc}$ . Therefore, the question why the  $V_{oc}$  for the Ga-doped Soltecture samples is significantly higher compared to the Ga-free samples cannot be answered

directly by the forward current density.

In the above-mentioned work of Contreras *et al.* [10] the authors found a clear correlation between the substrate temperature used during deposition of the selenium-based absorbers by a high vacuum evaporation process and the  $V_{oc}$ . It was already shown before, that high substrate temperatures during the growth process are needed to achieve improved performance parameters [90]. Similar to the performance improvements reported in [10, 90], the high temperature step during processing the 3-step HZB samples may account for reduced recombination losses and the improved  $V_{oc}$  compared to the 2-step processed devices. However, in Cu(In,Ga)S<sub>2</sub> solar cells recombination at the buffer/absorber interface is typically found to limit the  $V_{oc}$ , which leads to the assumption that defects at the interface are more relevant compared to bulk defects in the discussion of limiting recombination processes in this thesis.

### 6.1.2 Temperature-Dependent IV Characteristics

In order to determine the  $V_{oc}$ -limiting recombination mechanism,  $IVT$  characteristics are analyzed in this section. The parameter of main interest is the activation energy  $E_A$  of the saturation current density which enables to distinguish between interface recombination and bulk recombination as  $V_{oc}$ -limiting loss mechanism. From the large pool of available samples only a limited number could be chosen for  $IVT$  measurements within the scope of this work. To investigate the influence of Ga at the heterojunction on  $E_A$ , HZB samples with  $E_{g,min}$ -values ranging from 1.50 eV to 1.60 eV were selected. It should be noted, that a direct correlation of the results and the RTP process parameters is avoided. This would not be justified due to the limited number of investigated samples and the discrepancy between the nominal RTP parameters and the resulting inhomogeneous absorber characteristics (see Section 5.1). In addition to the HZB samples, two Soltecture samples based on pure CuInS<sub>2</sub> absorbers are investigated. For these samples a particular low  $V_{oc}$  was detected in Section 6.1.1 compared to Ga-doped Soltecture and HZB samples with similar  $E_{g,min}$ -values. The value of  $E_A$  of these samples will be compared to those values obtained from the Ga-doped HZB samples to check for an indication of the low  $V_{oc}$ . Besides the analysis of  $E_A$  the quality factor  $A$  is considered, as its value and temperature dependence can potentially define the information about the recombination path. In this section it is in particular consulted to ascertain whether or not the Fermi level is pinned at the heterointerface. Since no systematic relation between  $E_{g,min}$  and  $A$  was found for the samples investigated in this work, this parameter is discussed on two exemplary samples from HZB and Soltecture, respectively.

From  $IVT$  measurements  $E_A$  can be derived using a linear extrapolation of the open circuit voltage to  $T = 0$  K [61]. This analysis was performed for  $V_{oc}(T)$  at one sun illumination in the temperature range  $T = 150 \dots 300$  K for six HZB samples with different  $E_{g,min}$  and two Ga-free Soltecture samples. In Fig. 6.7 (a) the extrapolation is exemplarily shown for three HZB samples and one Ga-free Soltecture sample. In Fig. 6.7 (b) the derived activation energies  $E_A$  are plotted versus  $E_{g,min}$  for all investigated samples. From this representation the following conclusions can be drawn for the general case

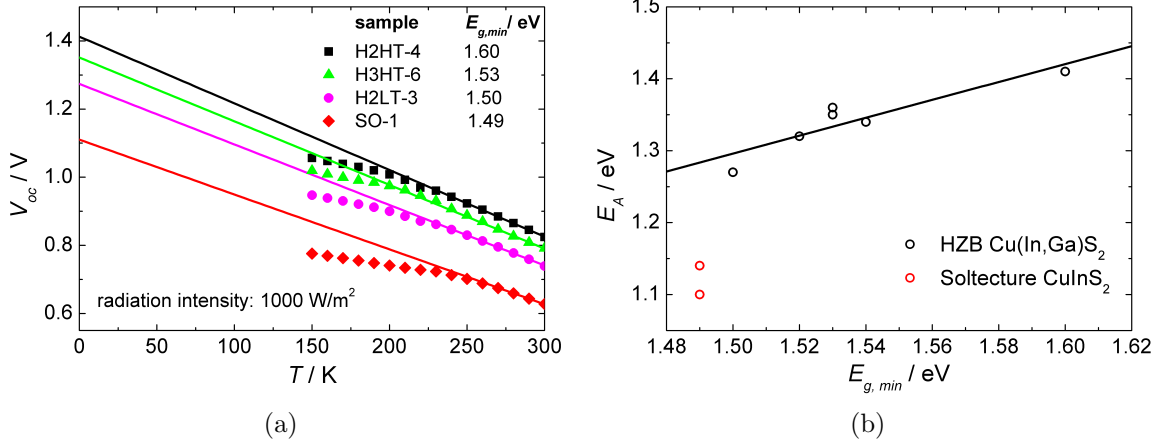


**Fig. 6.7:** (a) Extrapolation of the temperature-dependent  $V_{oc}$  for three Cu(In,Ga)S<sub>2</sub> samples with different  $E_{g,min}$  and one Ga-free Soltecture sample. (b) Activation energy  $E_A$  versus  $E_{g,min}$  for all investigated samples. For the Ga-doped HZB samples  $E_A$  increases linearly with  $E_{g,min}$  as indicated by the linear fit (solid line). The activation energies of samples based on pure CuInS<sub>2</sub> absorbers appears to be much smaller and deviate from the trend. The assignment of sample IDs is given in Table 5.1.

that the heterojunction is characterized by a negative conduction band offset:

For all investigated samples  $E_A$  is found to be smaller than  $E_{g,min}$ . This result, which is frequently observed for solar cells based on Cu(In,Ga)S<sub>2</sub>, is commonly interpreted to indicate recombination at the buffer/absorber interface as the predominant loss mechanism in these devices [13, 14, 63]. In case of  $E_A < E_{g,min}$  the activation energy measures

- the interface band gap energy  $E_{g,i}$  as long as the Fermi level is not pinned at the interface.  $E_{g,i}$  is expected to be smaller than the band gap within the absorber in devices with a negative conduction band offset (see Fig. 2.5).
- the recombination barrier for holes  $\Phi_b^p$  at the interface if the Fermi level is pinned by a high density of interface defect states [5]. This barrier corresponds to the energetic distance between the Fermi level and the valence band edge at the interface (see Fig. 2.5).

In the presence of a negative conduction band offset it is not possible to draw a definite conclusion from the value of  $E_A$  whether or not the Fermi level is pinned. This question can be potentially answered by regarding the diode quality factor  $A$ . The quality factor can be derived from the exponential part in the forward current range of a dark  $IV$  curve [80]. Its value is defined by the location of the dominant recombination path within the solar cell, e.g.  $A = 2$  is observed for recombination in the space charge region (SCR) while  $A = 1$  results from recombination at the interface or in the neutral bulk of the absorber [5]. In addition, the value of  $A$  depends on whether or not the Fermi level is pinned. It is furthermore affected when the recombination is enhanced by tunneling via defect states in the SCR which leads to an increase in  $A$  at low temperatures. In order to gain information about the presence of Fermi level pinning (FLP),  $A(T)$  will

**Table 6.1:** Distinction between  $E_A = E_{g,i}$  and  $E_A = \Phi_b^p$  by means of the quality factor and its temperature dependence for the case of interface recombination limiting the  $V_{oc}$ . (+) marks the ideal case in accordance with theory and (-) marks the ideal case not in accordance with theory [91].  $E_{g,i} = E_{g,i}(x, y)$  and  $\Phi_b^p = \Phi_b^p(x, y)$  denote a fluctuating interface band gap and a fluctuating hole barrier, respectively. An exponentially distributed defect concentration  $N_{IF}$  can account for the temperature dependence of  $A$  in case of  $E_A = E_{g,i}$ , expressed by  $dN_{IF}(E)/dE \sim \exp(E/kT^*)$ , where  $1/kT^*$  represents a damping factor. This table is extracted from [91] where a detailed description of its derivation is given.

	$dA/dT = 0$		$dA/dT < 0$
	$A = 1$	$A > 1$	$A \geq 1$
$E_A = E_{g,i}$ without FLP	strongly asymmetric heterojunction	+	Tunneling enhancement or $E_{g,i} = E_{g,i}(x, y)$ or $dN_{IF}(E)/dE \sim \exp(E/kT^*)$
$E_A = \Phi_b^p$ with FLP	+	-	Tunneling enhancement or $\Phi_b^p = \Phi_b^p(x, y)$

be discussed using the example of the HZB samples H3HT-3 and H3HT-6 and the Soltecture samples SO-1 and SO-2 presented in Fig. 6.8 (a) and (b), respectively. The  $A$  factors were derived from  $IV$  curves measured in the dark for  $T = 150 \dots 330$  K.

At  $T > 300$  K the diode quality factor approaches values slightly below two for the Soltecture samples whereas  $A$  approaches one for the sample H3HT-3. For sample H3HT-6 a shift in the quality factor is found at  $T > 300$  K from  $A \approx 2$  to  $A \approx 1$  upon improving the contact quality. With this contact improvement the  $A(T)$  curve is very close to that of sample H3HT-3. As has been exemplified in Section 5.2 by the dark  $IV$  curve of sample H3HT-6 at  $T = 300$  K, an increased series resistance induces an overestimation of  $A$  in the case of a poor contact. This finding raises reasonable suspicion that non-ideal contacts also result in overestimated quality factors for the Soltecture samples considered in Fig. 6.8. However, in contrast to the  $IV$  measurements at STC presented in Section 6.1.1, the measurement range for the current used during the  $IVT$  measurements is not sufficient to evaluate the series resistance for a correction of the  $IV$  curves.

The increase of  $A$  with decreasing temperature is indicative for tunneling-assisted carrier recombination within the SCR which has already been reported for Cu(In,Ga)S<sub>2</sub> solar cells before [13, 14]. On the other hand,  $R_s$  increases with decreasing temperature which is expected to overestimate  $A$  for low temperatures. It is likely that the true temperature dependence of  $A$  is less pronounced than indicated in Fig. 6.8 (a).

A suggestion for the distinction between  $E_A = E_{g,i}$  (no FLP) and  $E_A = \Phi_b^p$  (FLP) by

means of  $A$  in case of interface recombination as  $V_{oc}$ -limiting process is given by Scheer in [91]. Using analytical models describing the recombination rate at the interface in each case, the author comes to the conclusions summarized in Table 6.1. According to Scheer,  $A \approx 1$  could be explained by a pinned Fermi level whereas  $A > 1$  would exclude the possibility of Fermi level pinning as long as  $dA/dT = 0$ . On the other hand,  $A = 1$  is also expected if the heterojunction is strongly asymmetric, that is when almost the complete voltage drops across the absorber layer. Furthermore, as  $dA/dT < 0$  in the presented data, Fermi level pinning may be present even if  $A \geq 1$ . This can be a consequence of tunneling enhanced recombination, a spatially fluctuating hole barrier or an exponential defect distribution at the interface. However, if the quality factor is temperature-dependent, the result  $A \geq 1$  can be observed in the presence as well as in the absence of FLP. In summary, the finding that  $A \approx 1$  for sample H3HT-3 and the well contacted sample H3HT-6 at  $T > 300$  K points to a pinned Fermi level but the temperature dependence of  $A$  does not allow for a clear interpretation. Analogically, the temperature dependence of  $A$  hinders the interpretation of the results for the SO samples.

It should be mentioned that a high series resistance, e.g. caused by improper contacts as discussed above, does not influence the  $V_{oc}$ . Consequently, the analysis of the activation energy  $E_A$  remains unaffected by these problems. In contrast to the quality factor, the activation energy is found to correlate with the Ga-content at the heterojunction. As demonstrated in Fig. 6.7 (b), the activation energies obtained for the HZB samples increase linearly with the minimum band gap energy, where  $\Delta E_A \approx \Delta E_{g,min}$ . According to the arguments given in Section 2.4 with regard to a negative conduction band offset, an up-shift of the absorber CBM will not increase the  $V_{oc}$  as long as interface recombination limits the  $V_{oc}$ . This statement is based on the fact, that lifting up the CBM would neither increase  $\Phi_b^p$  nor  $E_{g,i}$  (see Fig. 2.5). Irrespective of the existence of FLP, the activation energy would not be affected. Since interface recombination is confirmed to be the  $V_{oc}$ -limiting mechanism for all investigated samples, the linear increase of  $V_{oc}$  and  $E_A$  with  $E_{g,min}$  supports the assumption that the Ga-concentration influences the valence band energy in Cu(In,Ga)S<sub>2</sub>. Due to the finding that  $\Delta E_A \approx \Delta E_{g,min}$  it could even be concluded that Ga mainly shifts the VBM while the CBM remains essentially unchanged. This would be in contrast to the effect of gallium in Cu(In,Ga)Se<sub>2</sub>, where Ga is observed to affect mainly the CBM [37]. In a study on CdS/Cu(In,Ga)S<sub>2</sub> junctions with various Ga-concentrations at the heterocontact it was also stated that Ga mainly affects the CBM in analogy to what is known from selenium-based devices [66]. As already mentioned in Section 2.4, the error range of the results obtained by X-ray spectroscopic methods in the corresponding study is very close to the band gap widening due to Ga. Thus, further investigations are needed to verify which of the band edges is shifted by gallium.

In fact, the increase of  $E_A$  and  $E_{g,min}$  by lowering the VBM via Ga-doping would be a good prior condition for the reduction of interface recombination losses. Nevertheless, interface recombination remains the dominant loss process even for those samples with large recombination barriers. This permits the conclusion that a high concentration of interface defects is present in sulfur-based chalcopyrite solar cells which fundamentally limits the  $V_{oc}$ . For the investigation of recombination mechanisms it follows that in-

interface defects have a much higher importance in Cu(In,Ga)S<sub>2</sub> solar cells compared to their Cu(In,Ga)Se<sub>2</sub> counterparts, for which the  $V_{oc}$  limitation is essentially established by the bulk properties of the absorber material [40, 92, 93].

Another scenario could generally explain the increase in  $V_{oc}$  and  $E_A$  with increasing Ga at the absorber surface. In case of FLP ( $E_A = \Phi_b^p$ ), the increase in  $E_A$  does not necessarily rely on a down-shift of the valence band but could also arise from an up-shift of the Fermi level. If so, the type inversion would be improved by an enlargement of the barrier  $\Phi_b^p$ . For shifting the energetic position of the pinned Fermi level closer to the CBM of the buffer, the defect distribution at the heterointerface would have to be modified. If such a modification was evoked by a change in the Ga-concentration at the heterojunction, this could account for the increase in  $E_A$  with  $E_{g,min}$ . In Section 6.2 these considerations will be resumed and contribute to the clarification of the very important question to which amount the VBM and the CBM are shifted by Ga, respectively.

The activation energies for the Soltecture samples shown in Fig. 6.7 (b) differ considerably from the trend found for the HZB samples. In the presence of FLP, a reduced  $E_A$  compared to the Ga-doped HZB samples can be a consequence of a Fermi level position closer to mid-gap, analogous to the considerations above. Thereby, the type inversion would be reduced which would be unfavorable for achieving high  $V_{oc}$ -values in case of interface recombination (see Section 2.4). If the Fermi level is not pinned, the low activation energy  $E_A = E_{g,i}$  compared to the HZB samples can only be explained by a smaller energetic distance between the VBM of the absorber and the CBM of the buffer at the interface. However, from the *IVT* results it cannot be concluded which of these scenarios is true. Nevertheless, the low  $E_A$ -values of the Ga-free samples provide a reason for their low  $V_{oc}$ -values reported in Section 6.1.1 relative to the Ga-doped samples of similar  $E_{g,min}$ . The assumption made in Section 6.1.1 that an increased recombination velocity at the heterojunction may be responsible for the low  $V_{oc}$  is thereby confirmed.

### 6.1.3 Conclusions I

High annealing temperatures are required during the RTP process in order to enable the diffusion of Ga towards the heterointerface where it induces a widening of the band gap. This could be observed on differently RTP-processed samples from HZB. From these samples the following conclusions can be drawn from the results of *IV*, *EQE*, *EDX* and *IVT* measurements regarding the influence of Ga at the heterointerface on the device characteristics:

- A linear relation between  $V_{oc}$  and  $E_{g,min}$  is observed for  $E_{g,min} < 1.6$  eV, whereas for the sample series H1HT with  $E_{g,min} > 1.6$  eV the open circuit voltage approaches  $V_{oc} \approx 820$  meV.
- Exceptions to this trend are observed for some samples of the series H3VT, H3HT and H3H\*T which exhibit significantly higher  $V_{oc}$ -values as compared to those of other samples with similar  $E_{g,min}$ . For these samples a short step of especially high sulfurization temperature (see Table 5.1) was applied during the RTP process.

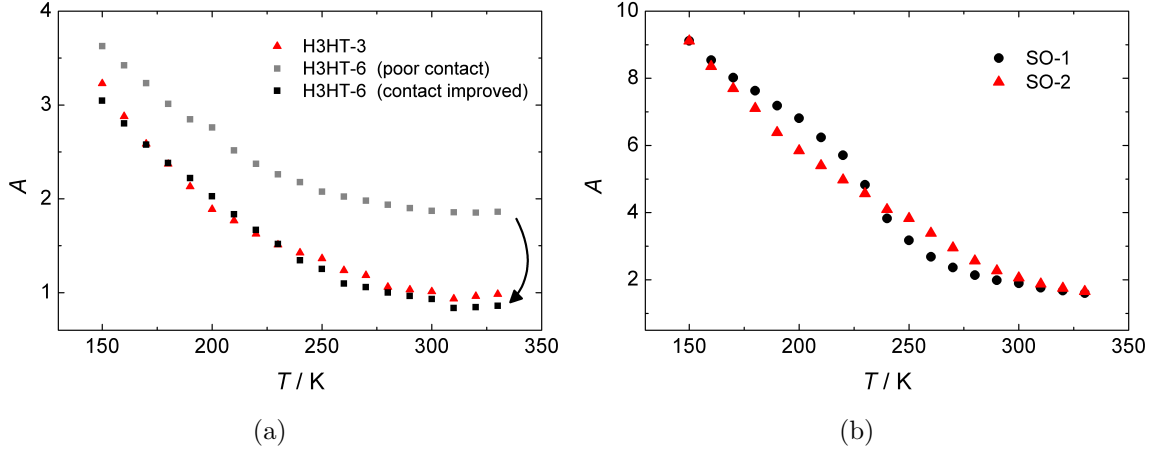


**Fig. 6.8:** Temperature dependent diode quality factor  $A$  derived from  $IV$  curves measured in the dark for (a) HZB samples and (b) Ga-free Soltecture samples. The data of sample H3HT-6 is shown in (a) for a measurement before and after rebuilding the contacts. The assignment of sample IDs for processing details is given in Table 5.1.

- The forward current density corrected by  $R_s$  and  $R_p$  is found to be higher for these peculiar samples which points to recombination losses via defect states in these devices.
- A V-shaped Ga-profile, which could explain the improved  $V_{oc}$  in the above mentioned samples, could not be confirmed with single EDX line scans. However, a laterally inhomogeneous Ga-distribution at the interface might be present and could contribute to the elevated  $V_{oc}$ -values. This would require a more integral investigation of the chemical depth profiles which was beyond the scope of this work.
- Also for those samples with  $E_{g,min}$ -values corresponding to pure  $\text{CuInS}_2$  a low Ga-concentration was found at the heterointerface. A laterally inhomogeneous Ga-distribution at the heterointerface may account for the comparatively high  $V_{oc}$ -values despite their rather low  $E_{g,min}$ -values.
- The activation energies  $E_A < E_{g,min}$  derived from  $IVT$  measurements identifies recombination at the buffer/absorber interface as the dominant recombination mechanism.
- An increase of  $E_{g,min}$  is found to provoke an equivalent increase of  $E_A$  which has been investigated systematically for the first time in this work. This result suggests that the band gap widening by Ga is mainly caused by a down-shift of the valence band which is in direct contrast to what is known from  $\text{Cu}(\text{In,Ga})\text{Se}_2$ .
- If the Fermi level was pinned in the studied samples, the assumption that Ga acts preferentially on the VBM has to be handled with care. In this case, an upward shift of the Fermi level energy at the interface induced by Ga could also explain the increase in  $E_A$  with  $E_{g,min}$ .

The Soltecture samples are characterized by the fact that the incorporation of Ga induced an increase in  $V_{oc}$  of 90 mV while the  $E_{g,min}$  remained identical to the value observed on the Ga-free samples. Furthermore, the results from *IV*, *EQE*, *EDX* and *IVT* measurements on these samples allow for the following conclusions:

- Despite their identical  $E_{g,min}$ , the Ga-doped SOG samples fit the  $V_{oc}$  versus  $E_{g,min}$  trend of the HZB data while the Ga-free SO samples stand out due to their low  $V_{oc}$ .
- Similar to the results on the HZB samples, the forward current density corrected by  $R_s$  and  $R_p$  is found to be higher for the SOG samples compared to that of the SO samples. On the other hand, the values of  $J_0$  and  $A$  obtained for the SO samples are lower than those derived for the SOG samples. This finding hinders a clear attribution of recombination losses via defect states in the SO samples to their low  $V_{oc}$ .
- EDX line scans on the SOG samples revealed analogous results to those found for the HZB samples: The Ga depth profiles did not show a V-shape that could explain the different  $V_{oc}$  at an  $E_{g,min}$  that is identical to that of the SO samples. On the other hand, the presence of Ga at single positions within the SOG samples could be verified. A higher number of line scans would be needed to check for positions that exhibit a V-shape of the Ga-profile or Ga-free regions at the heterocontact that could explain the enlarged  $V_{oc}$  in combination with an unchanged  $E_{g,min}$ .
- *IVT* measurements on the SO samples reveal  $E_A < E_{g,min}$  with  $E_A$ -values being significantly lower compared to the values of the HZB samples. This finding suggests that a reduced  $E_{g,i}$  or  $\Phi_b^p$  promotes recombination losses via interface defects that account for the reduced  $V_{oc}$  of these samples.

## 6.2 Thermal Admittance Spectroscopy

Following the explanations given in Sections 2.3 and 2.4 and the results presented in Section 6.1.2, recombination via interface defects is considered to limit the  $V_{oc}$  in Cu(In,Ga)S<sub>2</sub> solar cells. In this chapter defect characteristics are investigated with regard to the impact of Ga by means of thermal admittance spectroscopy (TAS). Thereby the parameter of main interest is the activation energy  $E_a$  which shall give an estimation of the energetic depth of the defect within the band gap of the semiconductor. In order to distinguish between bulk and interface defects, TAS can be performed with an applied (reverse) bias voltage. Since this is expected to shift the electron Fermi level at the interface, the activation energy of an interface defect should change (in case of an energetically continuous defect distribution) or the defect should be completely removed from the observed spectrum. In contrast,  $E_a$  should remain unaffected for a bulk defect since the intersection of the electron Fermi level and the defect level would be shifted only spatially (on the depth-scale) whereas its energetic distance position within the band gap would remain constant<sup>4</sup>. However, if the Fermi level is pinned

---

<sup>4</sup>This is only valid if the energetic distance between the defect and the correlated band is independent of the depth coordinate

at the interface, a shift of its energetic position at the interface cannot be achieved by the applied bias voltage. In this work, no voltage induced changes were observed in the TAS spectra. Since it could not be clarified by *IVT* measurements whether the Fermi level is pinned (see Section 6.1.2) no distinction between interface and bulk defects can be made by TAS in the first instance.

As explained in Section 4.2, TAS itself cannot reveal whether the observed signatures can be assigned to capture of minority or majority carriers, respectively. DLTS measurements are an appropriate tool to distinguish between majority and minority defect states but the application of sufficiently high reverse bias is required in order to generate practical signals. Unfortunately, the small avalanche voltage  $V_{av} \approx -0.5$  V of the samples investigated in this work impeded the implementation of DLTS measurements. Additionally, the DLTS technique is based on the measurement of small capacitance changes  $\Delta C$  with respect to the space charge capacitance  $C$ . If the defect concentration is low compared to the doping concentration,  $\Delta C/C$  is expected to be small and therefore difficult to detect. This could also have accounted for the particular low DLTS signals observed for the samples investigated in this work. However, DLTS measurements did not reveal reliable results and will therefore not be discussed in this work.

Even though the information about the defect origin (interface/bulk, minority/majority) cannot be derived from TAS spectra directly, the findings presented in this chapter demonstrate that some conclusions regarding these defect characteristics can be made in consideration of the band alignment in Cu(In,Ga)S<sub>2</sub> solar cells. Certainly, the focus should be on the detection of interface defects that may account for the limitation in  $V_{oc}$ . Nevertheless, results from those signatures that are assigned to bulk defects allow for important conclusions regarding the effect of Ga on the energetic positions of the VBM and the CBM, respectively.

The influence of Ga on the band alignment is especially discussed using the TAS spectra of HZB samples with different Ga depth profiles in Section 6.2.1. As shown in Section 6.1.1 the different sulfurization temperatures used during the RTP process evoked different values of  $E_{g,min}$ , that can be taken as an indicator for the Ga-concentration at the heterointerface. Section 6.2.2 deals with the comparison of Ga-doped and Ga-free Solteature samples. The derived defect spectra are compared to those obtained from the HZB samples. In Section 6.2.3 the signatures discovered by TAS in HZB and Solteature samples are compared to each other and to signatures reported in literature for CuInS<sub>2</sub> and Cu(In,Ga)Se<sub>2</sub> devices using the Meyer-Neldel rule (see Section 4.3). In particular, possible relations of the revealed signatures to the frequently discussed features N1 and N2 in Cu(In,Ga)Se<sub>2</sub> devices are considered.

The TAS spectra were measured in a frequency range  $f = 100$  Hz ... 200 kHz and a temperature range  $T = 30$  ... 350 K. To realize these temperatures the sample to be measured was mounted on a sample holder which was placed in a closed cycle cryostat. Helium in the sample chamber served as contact gas to allow for good temperature transfer and temperature control. Two contacts on the grid and two contacts on the molybdenum back contact were used to connect the sample to an impedance analyzer (Solartron 1260). By applying an ac-voltage of 30 mV the impedance analyzer derived the capacitance and the conductance from the amplitude and the phase shift of the

responding current signal. For this purpose a simple parallel equivalent circuit was assumed (see Section 4.1). To fulfill the important requirement  $R_P \gg R_S$  it was ensured that the sample was not shunted. Prior to the measurement, the samples were annealed in the He atmosphere for one hour at 350 K in the dark to ensure a common relaxed state for all investigated samples.

### 6.2.1 Defects in HZB Samples with Varied Ga Depth Profiles

HZB samples with varied Ga-concentrations at the heterointerface were investigated by TAS. Due to the high number of investigated samples, not every single spectrum can be discussed in detail within the scope of this work. Therefore, exemplary results of samples stemming from various RTP processes resulting in different  $E_{g,min}$ -values are presented. Differences in the spectra that correlate with the RTP process parameters or with  $E_{g,min}$  are discussed on the results of individual samples in order to exemplify general trends observed on the complete set of samples.

In Fig. 6.9 the  $Cf$  spectrum of sample H2HT-6 is presented. The sample was processed with a high sulfurization temperature (see Table 5.1) that resulted in a correspondingly high Ga-concentration at the interface. As shown in Section 6.1.1 this is correlated with enhanced values of  $E_{g,min}$  and  $V_{oc}$ , respectively. Four capacitance steps can be distinguished within the spectrum. For low temperatures and high frequencies the capacitance converges to its lowest value in the spectrum, that is the geometrical capacitance which results from a freeze-out of the charge carrier mobility. In this case the complete absorber layer acts as a dielectric so that the geometrical capacitance can be used to estimate the layer thickness according to Equation (3.36). For the example shown in Fig. 6.9 the geometrical capacitance of about  $(5.0 \pm 0.4)$  nF/cm<sup>2</sup> results in an absorber layer thickness of  $(2.1 \pm 0.2)$   $\mu\text{m}$ <sup>5</sup>, assuming that  $\epsilon = 11.8$ . This result is in good agreement with the typical absorber layer thickness deposited in these devices<sup>6</sup>.

At capacitances higher than the freeze-out step the first possibly defect-related step is observed which is further denoted by D0. In the given example the signature is confined by a lower capacitance threshold of  $(40 \pm 2)$  nF/cm<sup>2</sup> and an upper threshold of  $(60 \pm 2)$  nF/cm<sup>2</sup>. The lower threshold is determined by a frequency and temperature range in which a charge response of defects to the alternating voltage is restricted by the thermal emission rate described by Equation (3.18) (see also Section 3.4). Therefore, the corresponding capacitance value can be seen to represent the capacitance assigned to the "true" width of the space charge region, which is calculated to be  $x_d = (261 \pm 14)$  nm for the considered sample. Above the D0 signature step two further steps are observed, one of them between  $(60 \pm 2)$  nF/cm<sup>2</sup> and  $(90 \pm 2)$  nF/cm<sup>2</sup> and another one above  $(90 \pm 2)$  nF/cm<sup>2</sup> denoted by D1 and D2, respectively.

In Fig. 6.10 the  $Cf$  spectrum of sample H3HT-2 is shown. This sample stems from a 3-step RTP process that resulted in a particular high  $V_{oc} = 828$  mV in relation to its  $E_{g,min} = 1.53$  eV as shown in Fig. 6.5. The value corresponding to the width of the space charge region is approximately equal to the value obtained for sample H2HT-6.

<sup>5</sup>The error in  $\langle x \rangle$  derived for the layer thickness and the width of the space charge region is calculated in consideration of the given capacitance error by using Equation (3.36). The error in  $C$  results from the reading error at the smoothed transitions of the capacitance steps.

<sup>6</sup>According to the specification of the HZB, the nominal absorber layer amounts to about 2  $\mu\text{m}$ .

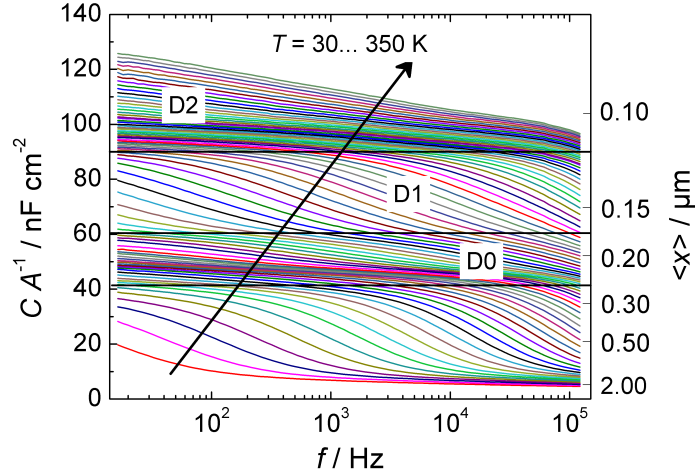


**Fig. 6.9:**  $Cf$  spectrum measured for sample H2HT-6. Above the freeze out step, i.e. for  $C > 40$  nF/cm<sup>2</sup>, three signatures denoted by D0, D1 and D2 can be distinguished. The right axis indicates the distance  $\langle x \rangle$  which is calculated from the capacitance in accordance with Equation (3.36). The value of  $\langle x \rangle$  has to be handled with care as outlined in Section 4.4. Its correlation with the "true" width of the depletion layer is only allowed in a particular frequency and temperature range. The assignment of sample IDs is given in Table 5.1.

In contrast, the geometrical capacitance of about  $(2.8 \pm 0.5)$  nF/cm<sup>2</sup> would yield an absorber layer thickness of  $(3.7 \pm 0.1)$  μm. This value is in fact higher than the true thickness, presumably due to an inadequate equivalent circuit at low temperatures evoked by a large series resistance of the device [69].

Regarding the steps above 40 nF/cm<sup>2</sup> the spectrum differs on some points from that presented in Fig. 6.9. An additional step denoted as DY follows the freeze out step whereas the capacitance above 80 nF/cm<sup>2</sup> only slightly increases but does not reveal such a significant step compared to the spectrum of H2HT-6.

According to Section 4.2 the emission rate of a defect indicated by the inflection point of the corresponding step in the  $Cf$  spectrum can be determined from the maximum of  $\omega dC/d\omega$  for each temperature. In Fig. 6.11 the derivative is plotted against frequency and temperature and thereby allows to quantify the temperature dependence of the emission rate for each signature in the two spectra described above. In this representation it becomes obvious that the signature DY is also weakly indicated between the freeze-out step and the signature D0 in the spectrum of sample H2HT-6 (Fig. 6.11 (a)). DY occurs differently pronounced in all investigated samples and is often only visible in the very low frequency range. It is most distinguishable in the spectra of those 3-step processed samples that attract attention due to a high  $V_{oc}$  related to their  $E_{g,min}$  (see Fig. 6.5). However, due to strong superpositions of DY with other defects in this energy range the results of this work did not allow for a systematic analysis of DY.

From Fig. 6.11 (a) it can also be seen, that the signature D2 only shows up in the high-temperature range which complicates the investigation of this signature. Indeed, the corresponding maximum cannot be unambiguously identified in the given presentation

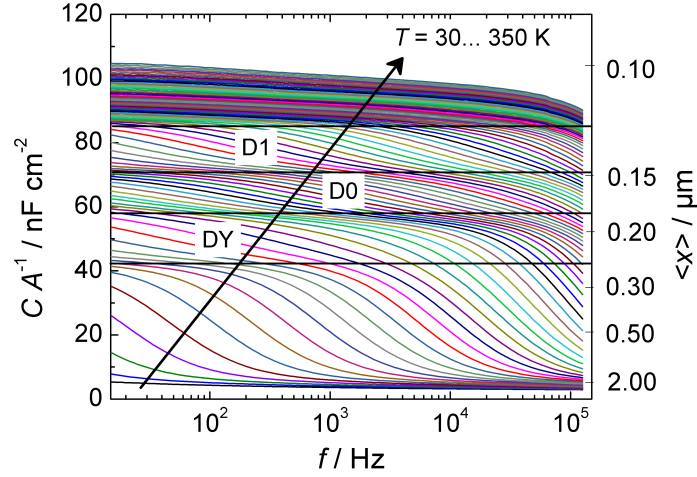


**Fig. 6.10:**  $Cf$  spectrum measured for sample H3HT-2. Above the freeze out step, i.e. for  $C > 40$  nF/cm<sup>2</sup>, three signatures denoted as DY, D0 and D1 can be distinguished. The right axis indicates the spatial coordinate  $\langle x \rangle$  which is calculated from the capacitance in accordance with Equation (3.36). The value of  $\langle x \rangle$  has to be handled with care as outlined in Section 4.4. Its correlation with the "true" width of the depletion layer is only allowed in a particular frequency and temperature range. The assignment of sample IDs is given in Table 5.1.

for sample H3HT-2 but is very weakly indicated if a closer look is taken at the low frequencies. The absence or only weak occurrence of D2 in the TAS spectra is observed for all 3-step processed samples that resulted in particular high  $V_{oc}$ -values, which may be explained by the following scenarios: On the one hand, practical limitations of TAS may limit the detection of this signature. Its activation energy  $E_a$  may be too high to be detected by TAS within the performable temperature and frequency range. On the other hand, the defect state evoking this signature may be absent or only exist with a low concentration within these samples which could relate to the enlarged  $V_{oc}$  of these samples.

A plot of the threshold frequency  $\omega_0 = 2e_{n,p}$  versus  $1/T$  according to Equation (3.18) gives an Arrhenius representation which enables to derive the activation energy  $E_a$  of the emission rate from the slope of the associated fit. This is presented in Fig. 6.12 for the signatures discussed above (with exception of DY) taken from exemplary  $Cf$  spectra of samples stemming from different RTP processes: The green, red and blue data points are assigned to the signatures D0 and D1 and belong to three exemplary samples of different band gap energies, respectively. To evaluate the activation energy of D2, the data of two samples (H1HT-3 and H3H\*T-4) were added to the Arrhenius diagram as this signature arises more clearly in these devices. The activation energy  $E_a$  of D2 varies strongly between 380 and 690 meV but appears to be generally higher for samples with higher  $V_{oc}$  stemming from the H3H\*T process. In contrast, the signature D1 is confirmed with a very stable activation energy of about 370 meV independent of the RTP process parameters and performance parameters of the device. For the signature D0 the activation energy  $E_a$  is found to increase with the minimum band gap energy approximately from 100 to 250 meV. This relationship is demonstrated in

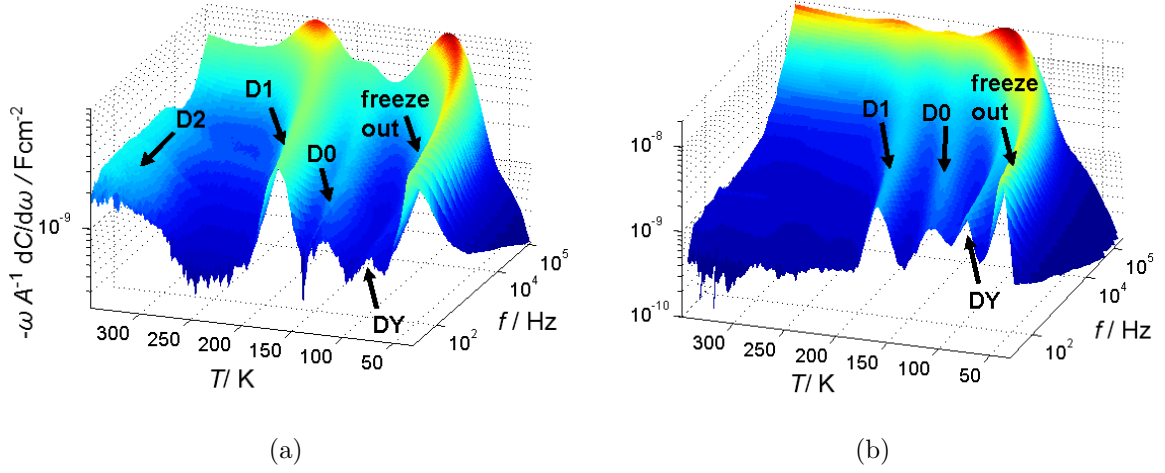


**Fig. 6.11:** Derivative representation of the  $Cf$  spectra presented in Fig. 6.9 and 6.10 for (a) sample H2HT-6 and (b) sample H3HT-2, respectively. Peaks visualize the characteristic response of the different signatures at given temperature. The assignment of sample IDs is given in Table 5.1.

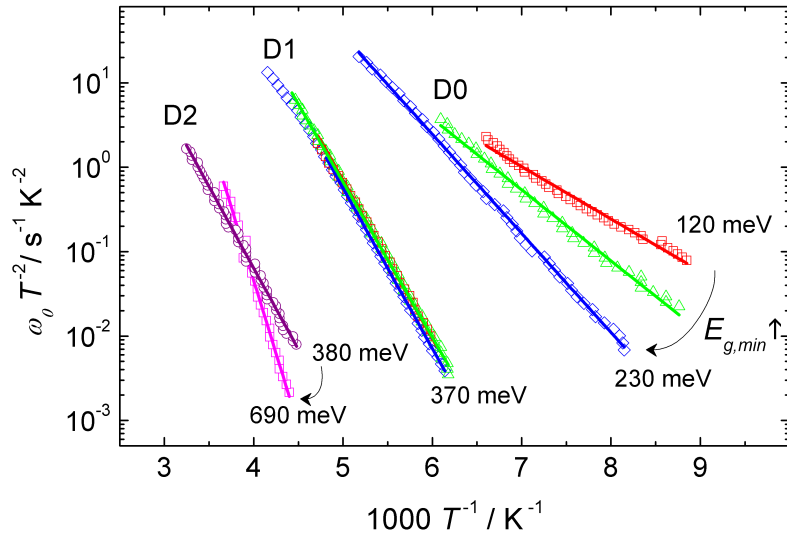


**Fig. 6.12:** Representative Arrhenius plot for  $\text{Cu}(\text{In,Ga})\text{S}_2$  samples from HZB. Green, red and blue symbols represent the signatures D0 and D1 observed in three samples of different  $E_{g,\text{min}}$ . The signature D2 was confirmed only in samples of the series H1HT and H3H\*T (violet and magenta symbols, respectively) whereas in other samples it is visible but less distinctive and more difficult to evaluate.

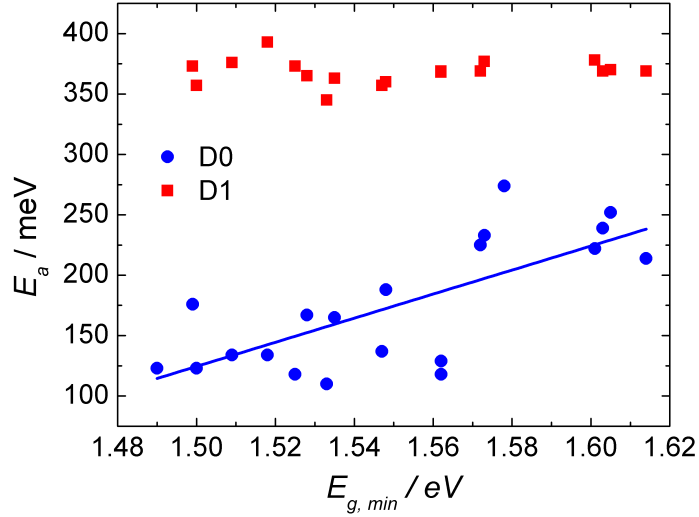


**Fig. 6.13:** Activation energies  $E_a$  derived for the signatures D0 and D1 for  $\text{Cu}(\text{In,Ga})\text{S}_2$  samples stemming from different RTP processes resulting in varied  $E_{g,min}$ . A linear fit to the D0 data indicates the coupling between  $E_a$  and  $E_{g,min}$  whereas  $E_a$  of D1 appears to be insensitive to the minimum band gap of the absorber.

more detail in Fig. 6.13 where the activation energy for signature D1 is additionally plotted to illustrate its comparatively stable value. A fit to the data from signature D0 corresponding to the Arrhenius relation (3.18) indicates that the increase in activation energy roughly amounts to the increase in the band gap energy.

So far the steps arising in the  $Cf$  spectra were discussed in a general manner without speculating on the physical origin of the signatures. It should be reminded that different origins for steps in admittance spectra have been discussed in literature as mentioned in Section 2.3. Nevertheless, the signatures observed in this thesis are treated as to be potentially evoked by electronic defect states. Based on this assumption their interaction with device parameters and their relevance for the clarification of open questions regarding the influence of Ga on the band alignment in  $\text{Cu}(\text{In,Ga})\text{S}_2$  solar cells are investigated. The activation energy  $E_a$  of the signature can be interpreted as a measure for the energetic depth of the associated defect within the band gap, although this may be an inaccurate interpretation as discussed in Section 3.1. As already mentioned in Section 4.2, a TAS measurement cannot resolve whether  $E_a$  refers to the energetic difference between the detected defect state and the valence band or the conduction band, respectively. Especially if a strong type inversion at the heterojunction of the  $\text{Cu}(\text{In,Ga})\text{S}_2$  exists, the intersection of a minority defect state with the Fermi level might contribute to the measured capacitance.

Turcu *et al.* [37] proposed that the correlation of  $E_a$  of an identified majority or minority defect with the absorber composition can be used to verify the influence of the individual elemental concentrations on the energetic positions of the VBM and CBM. In this way, the authors investigated the influence of gallium and sulfur on the band alignment of  $\text{Cu}(\text{In}_{1-x}\text{Ga}_x)(\text{Se}_{1-y}\text{S}_y)_2$  devices with  $0 < y < 0.7$  for two sets of samples with  $x = 0$  and  $x \approx 0.3$ , respectively, by using the defect states N1 and N2 as reference levels.

However, their study did not include selenium-free samples and the influence of Ga on the VBM and the CBM of pure sulfur-based devices remained open.

The approach used by Turcu *et al.* will be applied in the following by consideration of D0 whose  $E_a$  is found to vary with the Ga-concentration at the heterojunction. A classification of the charge state of D0 can be achieved by considering the conduction band alignment in Cu(In,Ga)S<sub>2</sub> devices as depicted in Fig. 6.14. The negative conduction band offset at the Cu(In,Ga)S<sub>2</sub>/CdS interface is estimated to amount to about 300 meV [64, 65]. Therefore, it is unlikely that a bulk minority defect level with  $E_a$  being smaller than the conduction band offset intersects the Fermi level within the SCR. Accordingly, those minority carriers are not expected to contribute to the device capacitance measured during TAS experiments. Since the maximum activation energy obtained for D0 amounts to  $E_a = 250$  meV, its interpretation as a bulk minority defect can be excluded. The signature D0 is additionally unlikely to arise from an interface minority defect, regardless of whether Ga acts on the valence or the conduction band. In the presence of a cliff at the interface an increase of the conduction band energy introduced by Ga should not affect the interface band gap and thereby the activation energy  $E_a$  of an interface minority defect should remain unaffected. Also a down-shift of the valence band by Ga would generally not increase the activation energy of a minority defect. Consequently, the signature D0 can only be attributed to a majority defect whose activation energy varies with the energetic position of the valence band. The effect of an increasing activation energy of the majority defect D0 with increasing gallium concentration in the front section of the absorber points to an impact of Ga on the VBM position. Additionally, it is found that the change in  $E_a$  corresponds to a comparable change in  $E_{g,min}$ . Accordingly, it can be concluded that Ga even leaves the conduction band rather unaffected which was already suggested due to a variation in the activation energy of  $J_0$  by  $\Delta E_A \approx \Delta E_{g,min}$  in Section 6.1.2. This finding establishes a key result of this work.

Due to its comparatively low activation energy D0 is furthermore expected to arise from a majority bulk defect rather than from majority interface defects because the Fermi level position at the interface is expected in the upper half of the band gap. Consequently, the position of the minimum band gap energy and the intersection point of the D0 energy and the Fermi level are not generally expected at the same depth position, because  $E_{g,min}$  is expected to be located at or close to the buffer/absorber interface. This might explain the deviation of some data points for D0 in Fig. 6.13 from the linear trend.

In accordance to these findings the signature D1 has to be assigned to a minority defect level due to its activation energy which is independent of changes of the minimum band gap energy. These conclusions regarding the energetic positions of D0 and D1 demonstrate that even though TAS does not allow to distinguish between majority and minority contributions, an assignment to the charge state is enabled in a systematic study of varied samples and consideration of the conduction band alignment.

However, it is not evident if D1 is caused by a defect at or close to the interface or by a bulk defect. One approach to probe the presence of interface defects is to perform TAS with an applied reverse bias voltage. As long as the Fermi level is not pinned at

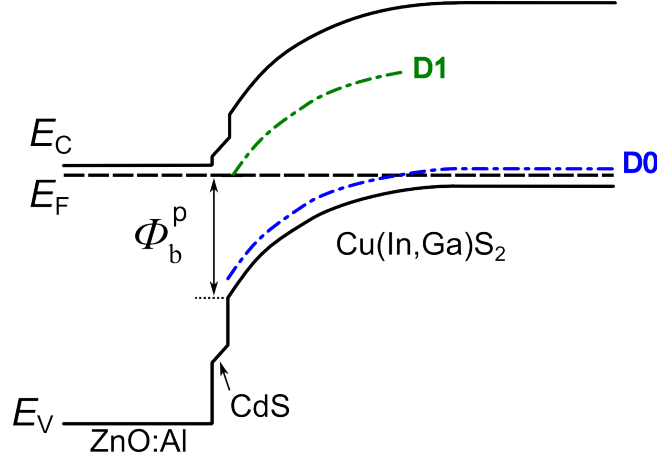


**Fig. 6.14:** Sketch of a band diagram for a Cu(In,Ga)S<sub>2</sub> solar cell with the signatures D0 and D1 interpreted as majority bulk defect and minority bulk defect. Whether D1 is evoked by a defect at or close to the interface or by a bulk defect remains to be resolved.

the interface, the bias voltage is expected to change the position of the electron Fermi level  $E_{Fn}$  at the interface and thereby the measured activation energy of interface defects. Such tests were also performed on the samples presented in this thesis, but did not reveal any changes in the TAS spectra. It follows, that either the Fermi level is pinned or D1 does not originate from interface defects at all. Certainly the cliff at the absorber/buffer interface poses an obstacle for the detection of D1 as a bulk minority defect as well, which is finally a matter of the real cliff height and the type inversion at the interface. Concerning the activation energy of D1 and its declaration as a minority defect this signature can be associated with the signature N1 known from Cu(In,Ga)Se<sub>2</sub> devices where it is commonly observed as minority signal in DLTS. The activation energy  $E_a = 370$  meV of D1 could approximately be in line with values found for N1 by Turcu *et al.* [37]. In their study the authors investigated the shift of the activation energy of the N1 signature within the Cu(In<sub>1-x</sub>Ga<sub>x</sub>)(Se<sub>1-y</sub>S<sub>y</sub>)<sub>2</sub> alloy system depending on the sulfur and the gallium content. However, they only investigated samples with sulfur contents up to  $y = 0.6$  so that the N1 activation energy for  $y = 1$  can only be estimated. Furthermore, the samples were grown under Cu-rich conditions and it is not ensured that N1 appears in Cu-poor grown Se-free samples at all. Using the example of N1, it becomes clear that the activation energy alone is insufficient for the assignment of a defect. Values ranging from 30 to 200 meV have been reported in literature for N1 and the activation energy can be influenced by annealing the devices in ambient air (see Section 2.3).

Nevertheless, taking the activation energy as an indicator, the signature D2 could correspond to the bulk acceptor state N2 in Cu(In,Ga)Se<sub>2</sub>. In Cu(In,Ga)Se<sub>2</sub> N2 has an activation energy of 280 – 300 meV but in pure sulfur-chalcopyrites N2 could lie deeper in the band gap with activation energies above 500 meV [37]. In contrast to D0 and D1, the D2 signature is often not available in the measured TAS spectra. Additionally,

D2 is in most cases hard to evaluate resulting in less statistics for this capacitance step. As mentioned before, the absence of D2 in the spectra from 3-step processed samples with particular high  $V_{oc}$ -values suggests a correlation with reduced recombination losses via this defect state. The high temperature step within the 3-step process may lead to a passivation of this defect. Also for N2 in Cu(In,Ga)Se<sub>2</sub> solar cells the value of  $V_{oc}$  was found to increase with decreasing defect concentration, but in these devices recombination in the bulk was found to limit the  $V_{oc}$ . If D2 corresponds to the bulk acceptor N2 its influence on the open circuit voltage remains open since the samples investigated in this work are limited by interface recombination. On the other hand, a bulk defect which is also present at or close to the interface may also be involved in interface recombination: Siemer [19] also found a comparably deep majority defect in Cu(In,Ga)S<sub>2</sub> solar cells by means of TAS and DLTS, whose concentration correlated with the value of  $V_{oc}$ . Since the author also indicated recombination via interface defects as the  $V_{oc}$  limiting mechanism, he concluded that this defect is located at or close to the interface.

### 6.2.2 Defects in Ga-doped and Ga-free Solteature Samples

TAS was performed on the Ga-free samples SO and Ga-doped samples SOG under the same conditions as described for the HZB samples in Section 6.2.1. An exemplary plot of  $-\omega dC/d\omega$  against frequency and temperature is given for both sample types in Fig. 6.15. One dominant signature appears above the freeze out step in the TAS spectrum for pure CuInS<sub>2</sub> based SO samples, referred to as Q2, whereas for the Ga-doped SOG samples an overlap of two dominant signatures, P1 and P2, appears in the corresponding temperature and frequency range. A weakly pronounced peak between the freeze-out peak and the dominant signatures indicates one more signature which is referred to P0 in SOG samples and Q1 in SO samples. For both absorber types the TAS spectra measured for several samples are very similar among themselves. The activation energy of signature Q2 in the SO samples amounts to about 300 meV. Due to simultaneous response of defects with similar activation energy and weak defect response, the activation energies of P0, P1, P2 and Q1 could not be evaluated in the conventional way, respectively.

An attempt has been made to fit the peaks representing P0, P1, P2 and Q1 shown in Fig. 6.15 by a linear combination of differently centered Gaussian functions to estimate the individual peak positions within the spectrum. The coordinates which were evaluated this way for two SO samples and two SOG samples result in the Arrhenius plot given in Fig. 6.16 in which only the data for Q2 were derived by standard peak analysis. For comparison, also the signatures D0 and D1 from the HZB sample H3HT-2 are added to the graph.

For the small peaks directly situated above the freeze-out peak, P0 in the SOG samples and Q1 in the SO samples, the respective position in the Arrhenius plot questions a common origin of these signatures. In the previous section a down-shift of the VBM by an increased Ga-concentration was assumed to correlate with the activation energy of the bulk acceptor D0 in the HZB samples. Accordingly, a relationship between the

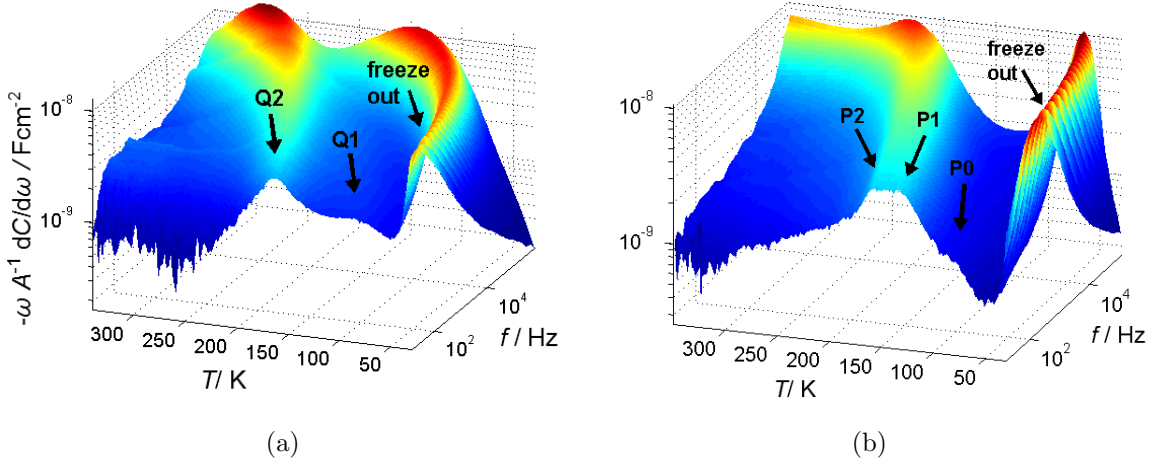


**Fig. 6.15:** Derivative representation of the  $Cf$  spectra measured for (a)  $\text{CuInS}_2$  sample SO-2 and (b)  $\text{Cu(In,Ga)S}_2$  sample SOG-2. The assignment of sample IDs is given in Table 5.1.

signature P1, which is one contributing part of the double-peak in the SOG-samples, and the signature Q1 in the SO samples may exist. These signatures could correspond to the signature D0 in the HZB samples, regarding their position within the Arrhenius representation. Though the minimum band gap energy  $E_{g,min}$  and the EDX scans presented in Section 6.1 indicate that the diffusion of Ga to the absorber surface during the RTP process failed in the SOG samples, a bulk acceptor with small activation energy is expected to intersect the Fermi level deeper in the bulk and not directly in front of the absorber/buffer interface. At the position of this intersection point the Ga content and thereby the band gap energy can be higher than at the interface. This could result in a correspondingly higher  $E_a$  at this position in comparison to a Ga-free absorber region. It should be noted that these considerations are not verified but rather based on an idea of the Ga-grading within the SCR of the SOG-samples and the assumption that P0 and Q1 can be assigned to majority bulk defects.

The second contribution to the double peak in the SOG samples, the P2 signature, could be related to the signature Q2 observed in SO samples. Regarding their activation energies, both of these signatures could correspond to the signature D1 found in HZB samples. Due to the results derived from HZB samples, where the activation energy of this signature was found to be independent of the Ga-concentration at the heterojunction, a reason for the different activation energies for Q2 and P2 is not obvious. Remarkably, the signature P2 from SOG samples matches the signature D1 from HZB samples in the Arrhenius plot which suggests a common origin of these features. Possibly the addition of Ga is responsible for a higher activation energy of D1 and P2 in the  $\text{Cu(In,Ga)S}_2$  devices compared to the  $E_a$  of Q2 in pure  $\text{CuInS}_2$  due to changes of the stoichiometry within the absorber material. If the signature originates from a defect level at or close to the buffer/absorber interface, also a shift of the Fermi level at the interface may cause the differences between the activation energies of Q2 and P2. In this case, the activation energy measures the difference between the conduction band

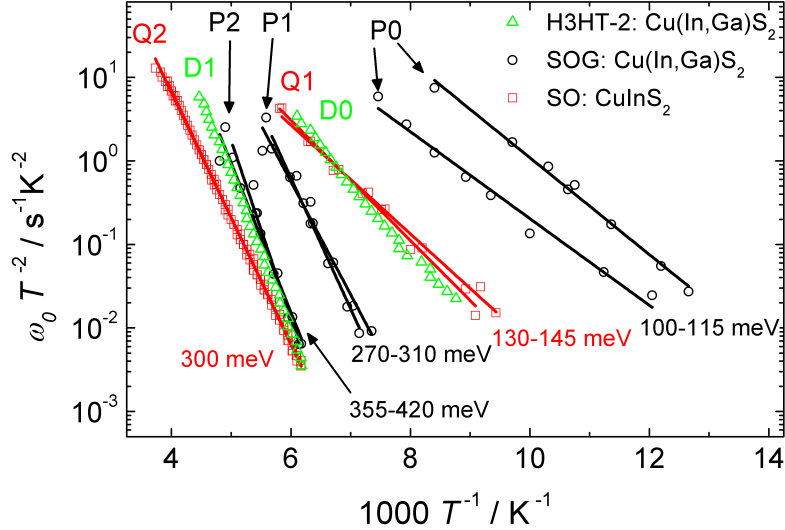


**Fig. 6.16:** Arrhenius plot for two Soltecture samples based on  $\text{Cu(In,Ga)S}_2$  (SOG-2 and SOG-6, black circles) and  $\text{CuInS}_2$  (SO-1 and SO-2, red squares), respectively. The signature Q2 for  $\text{CuInS}_2$  are conventionally derived from the peak positions in the derivative spectrum. The remaining signatures are evaluated by fitting the overlapping peaks with a linear combination of Gaussians. For comparison, D0 and D1 from the HZB sample H3HT-2 are added (green triangles). The assignment of sample IDs is given in Table 5.1.

of the buffer at the interface and the Fermi level. The increased activation energy in the SOG samples could therefore result from a reduced type inversion at the interface. It should be noted that the SO and SOG samples stem from different RTP processes and it remains questionable to which degree it is possible to compare the signatures from both materials. As evaluated by capacitance-voltage measurements the Ga-doped samples exhibit a wider space charge region  $x_d \approx 265$  nm and a lower charge carrier concentration  $N \approx 1.5 \cdot 10^{17} \text{cm}^{-3}$  compared to the Ga-free samples ( $x_d \approx 200$  nm and  $N = 2.7 \cdot 10^{17} \text{cm}^{-3}$ ). Consequently, the spatial and energetic positions of the defect response must be specifically considered. In order to account for these difficulties and to enable a direct comparison of the signatures detected in the Soltecture samples and in the HZB samples, the Meyer-Neldel rule is employed in the next section.

### 6.2.3 Defect Mapping with the Meyer-Neldel Rule

It is assumed that the majority of the defect states in chalcopyrite thin films are of native origin. For bulk defects, the energetic distance to the energy bands depends on the local band gap energy which complicates the direct comparison of defect activation energies measured in different samples. As described in Section 4.3 the Meyer-Neldel rule establishes a tool to examine defects identified in different samples for a common physical origin by including the apparent capture cross section of the defects. In this section this method is applied for a closer consideration of defect levels which have been discussed in the previous sections. Additionally, the Meyer-Neldel rule shall allow for

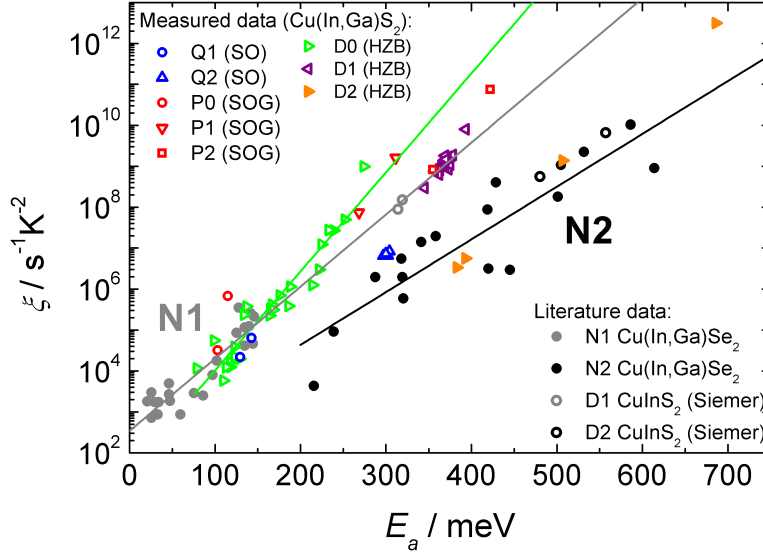


**Fig. 6.17:** Meyer-Neldel plot of the pre-exponential factor for the transition rate  $\xi$  from Arrhenius plots versus activation energy. Grey and black full circles and the corresponding fitted lines stem from the Meyer-Neldel plot presented in [76], where they were employed to distinguish between the signatures N1 and N2 in Cu(In,Ga)Se<sub>2</sub>. Grey and black open circles show literature data found by Siemer in CuInS<sub>2</sub> [19]. Colored symbols represent the characteristic defect parameters found in this work for Cu(In,Ga)S<sub>2</sub> samples.

a comparison of the detected defects with those already known from literature. Fig. 6.17 shows the MN-representation of the defect characteristics of the discussed samples in comparison with defect data published by Djebbour *et al.* [76] on the prominent signatures N1 and N2 found in Cu(In,Ga)Se<sub>2</sub> solar cells, as well as the deep defect levels found by Siemer *et al.* in Cu(In,Ga)S<sub>2</sub> solar cells [19]. A linear fit to the N1 literature data from Cu(In,Ga)Se<sub>2</sub> devices is represented by the gray line which is extrapolated to higher values of  $E_a$  while the black line represents a fit to the N2 literature data from Cu(In,Ga)Se<sub>2</sub> solar cells. The fact that the signatures D1 and D2 found by Siemer in CuInS<sub>2</sub> solar cells match the N1 fit and the N2 fit, respectively, suggests common origins of the respective signatures.

The green line represents a fit to the data originating from the D0 signature found in HZB samples. In Section 6.2.1 it was shown that  $E_a$  of D0 scales with the minimum band gap energy  $E_{g,min}$ . The trend found for D0 deviates from the N1 data which indicates that D0 does not relate to the prominent N1-level known from Cu(In,Ga)Se<sub>2</sub>. In contrast, both, the data of signature D1 identified in this work and the D1 data from Siemer are in line with the trend line of N1. Though the D1 data of both sources are restricted to rather small intervals of  $E_a$ , it seems to be reasonable to propose a common origin with the N1 phenomenon. Since N1 is often observed as minority signature [21, 42–44], the interpretation of D1 as minority defect in this work additionally supports the assignment of D1 to N1. It should be noted that Siemer observed D1 as majority signature in DLTS measurements in solar cells stemming from a sequential sulfurization process using moderate heating ramps compared to those realized in the RTP process.

On the other hand, in RTP-processed solar cells he found a minority contribution at 300 meV. Unfortunately, the value of  $\xi$  is not given for this minority signature in [19], preventing an individual mapping in the MN-plot.

The data from the deep level D2 identified in this work go along with the N2 trend line for Cu(In,Ga)Se<sub>2</sub> and the D2 data given by Siemer with the exception of one sample with  $E_a = 686$  meV. Nevertheless, the coincidence of the data points at lower  $E_a$  supports the assumption of a common origin of these defects which was already considered in Section 6.2.1 with regard to the activation energy of D2. The N2 level is commonly found as a majority bulk defect which is predominantly present in poorly performing solar cells. If D2 could be interpreted as a bulk acceptor, its activation energy  $E_a$  should correlate with  $E_{g,min}$  assuming that Ga shifts the VBM. Indeed, very different values of  $E_a$  in the range 380 ... 690 meV were obtained for D2 as shown in Fig. 6.17, whereas a clear correlation with  $E_{g,min}$  could not be confirmed. However, D2 was evaluable only in four samples leading to less reliable statistics on this defect level.

The signature P1 of Ga-doped SOG samples and the signature Q1 from Ga-free SO samples were proposed to correspond to the signature D0 from HZB samples already in the previous section. In fact, the data of P1 and Q1 both match the green trend line of D0 shown in Fig. 6.17. On the other hand, a definite attribution of P1 and Q1 remains questionable because their activation energies are restricted to a narrow range of low  $E_a$  where the three plotted lines are very close to each other. The same applies for the signature P0 identified in the SOG samples. However, following the results of Turcu *et al.*, N1 and N2 are expected to occur with higher activation energies in Cu(In,Ga)S<sub>2</sub> compared to those values reported for Cu(In,Ga)Se<sub>2</sub> devices. This is a consequence of the widened band gap of sulfur-based devices compared to selenium-based devices. Since sulfur acts on both energy bands, majority and minority defects are both expected deeper in the band gap. Consequently, the activation energies of P0, P1 and Q1 are too low to allow for an assignment to one of these defects, respectively.

The data points for signature Q2 from SO samples are located between the N1 and the N2 curve which prohibits an assignment to one of these signatures. As already deduced from the Arrhenius plot in Fig. 6.16, the signature P2 from SOG samples matches quite well the signature D1 found in HZB samples. In the Meyer-Neldel plot this can be confirmed for at least one of the two P2 data points so that P2 could also be related to the N1 signature. However, in order to verify this statement, a higher number of SOG samples would have to be investigated by TAS.

As a summary, Table 6.2 relates the defect states discussed in this work to the N1 and N2 states commonly observed in Cu(In,Ga)Se<sub>2</sub> and excludes those signatures which clearly deviate from the respective trend lines. A correlation between signatures within one column is proposed based on the results of the MN-plot and the discussions in Sections 6.2.1 and 6.2.2.

**Table 6.2:** Possible correlations between signatures derived from TAS in this work and the signatures N1 and N2 reported in literature for Cu(In,Ga)Se<sub>2</sub> devices. The labels D1 and D2 include the signatures obtained in this work as well as those reported in [19]. The columns labeled N1 and N2 include the defect states which are proposed to have the same physical origin. A relation between D0, P1 and Q1 could not be directly confirmed by the MN-plot but was suggested in Section 6.2.1 based on the observed influence of Ga on  $E_a$  of D0.

Cu(In,Ga)Se <sub>2</sub>	?	N1	N2
HZB Cu(In,Ga)S <sub>2</sub>	D0	D1	D2
SOG Cu(In,Ga)S <sub>2</sub>	P1	P2 (?)	–
SO CuInS <sub>2</sub>	Q1	Q2 (?)	Q2 (?)

## 6.2.4 Conclusions II

The TAS results obtained for HZB samples allow conclusions concerning the characteristic features of the observed defects and the influence of Ga on the band structure in Cu(In,Ga)S<sub>2</sub> devices:

- A signature D0 with  $E_a = 100 \dots 250$  meV was found in various samples. As a consequence of a cliff-like conduction band offset at the heterointerface it is assigned to a majority bulk defect (Section 6.2.1).
- $E_a$  of D0 is found to increase linearly with increasing Ga content close to the buffer/absorber interface. Combined with the cliff-like conduction band offset this supports the assumption that Ga shifts mainly the valence band and leaves the conduction band essentially unaffected (Section 6.1.2).
- A signature D1 with an activation energy  $E_a \approx 370$  meV which is independent of  $E_{g,min}$  (Fig. 6.13) is evaluated and assigned to a minority defect. The MN-plot suggests a relation between D1 in Cu(In,Ga)S<sub>2</sub> and N1 in Cu(In,Ga)Se<sub>2</sub>.
- A signature D2 with  $E_a = 380 \dots 690$  meV is found in TAS spectra of only some samples. This signature is missing in 3-step processed samples with high  $V_{oc}$ . The MN-plot suggests a relation between D2 in Cu(In,Ga)S<sub>2</sub> and N2 in Cu(In,Ga)Se<sub>2</sub>.

The TAS spectra of Ga-free and Ga-doped Solteature samples reveal the following:

- In the CuInS<sub>2</sub> samples two signatures, Q1 with  $E_a = 130 \dots 145$  meV and Q2 with  $E_a = 300$  meV are detected. While Q1 may be related to D0 in HZB samples, a relation of the signature Q2 to N1 or N2 in Cu(In,Ga)Se<sub>2</sub> remains to be confirmed.
- Three signatures are found in the Cu(In,Ga)S<sub>2</sub> samples provided by Solteature: P0 with  $E_a = 100 \dots 115$  meV, P1 with  $E_a = 270 \dots 310$  meV and P2 with  $E_a = 355 \dots 420$  meV. A relation of P1 to Q1 and D0 is taken into consideration

and P2 is assigned to D1 from HZB devices and N1 from Cu(In,Ga)Se<sub>2</sub>.

Further examinations of N1-like characteristics of signatures in question will be the matter of Section 6.3.

### 6.3 Detailed Investigation of N1-indicative Characteristics

Within Section 6.2 three signatures observed in the TAS spectra were considered to correspond to the prominent N1 signature known from Cu(In,Ga)Se<sub>2</sub> devices. These are the signatures D1 from Cu(In,Ga)S<sub>2</sub> samples from HZB and the signatures Q2 and P2 from Ga-free and Ga-doped Solteature samples, respectively (see Table 6.2). Beyond previous interpretations regarding the origin of the N1 signature, the interface defect model [21, 42–44] is of particular relevance for the sulfur-based samples investigated in this work due to their performance limitation by interface recombination. In this section characteristic features of D1 and Q2 are investigated to allow for more specific conclusions concerning their attribution to interface defects and the relation of these signatures to N1. The signature P2 observed in the Ga-doped Solteature samples is not considered here, since its overlap with signature P1 impedes an attribution of the observed characteristics to the individual signatures P1 and P2 (see Fig. 6.15 (b)). However, for the investigation of D1 and Q2 two approaches are applied which were proposed in literature concerning the N1 signature in Cu(In,Ga)Se<sub>2</sub> solar cells [20, 21]. The results obtained in this section are discussed with regard to the observations reported in these studies on N1 [20, 21].

The first approach relies on the considerations by Cwil *et al.* [20]. They discriminated between bulk and interface defects by analysis of the apparent doping profiles derived from *CV* measurements performed at different test frequencies. Their evaluation is based on the following argumentation:

If the investigated signature arises from a bulk defect, it might account for an increase of the apparent charge profile for high values of  $\langle x \rangle$  due to accumulation of charge in the traps with increasing reverse bias (see Section 4.4). However, according to Cwil *et al.* this should only be observed when the test frequency used for the *CV* measurement was higher than the emission rate of the defect. In contrast, the profile should be rather flat if the test frequency is lower than the emission rate, since the response of the bulk defect would correspond to that of shallow doping levels. In case of a homogeneous doping and defect distribution, respectively, doping and defect concentration should add to a charge profile being constant over the complete range of  $\langle x \rangle$ . However, this is only expected to be observed as long as no additional even deeper bulk defects are present. These could further account for a gradient in the apparent charge profile due to a carrier emission rate that is lower than the test frequency. If the signature is evoked by an interface defect, the deviation between profiles derived from *CV* profiling at high/low frequencies with regard to the emission rate of the defect turns out different: According to an earlier work by Niemegeers *et al.* [42], the height of a capacitance step in a *Cf* spectrum which is caused by interface defects does not correspond to the

concentration of interface traps but to the contribution of the depleted buffer layer. Consequently, the difference in charge densities derived from  $CV$  profiling at high and low frequencies relative to the transition frequency is not correlated to the trap concentration. Cwil *et al.* concluded that a  $CV$  measurement performed at high/low frequencies (HF/LF) should reveal apparent charge profiles that are identically shaped but displaced to each other on both, the spatial and the charge density axis. More precisely, the HF profile should be shifted to higher  $\langle x \rangle$  by a distance  $w_n$  corresponding to the width of the depleted buffer layer and to lower values of  $N$  as compared to the LF profile. Indeed, exactly this was observed by the authors for apparent doping profiles derived at frequencies higher and below the characteristic transition rate of the N1 signature. Accordingly, they assigned the N1 signature to an interface defect.

The second approach focuses on systematic investigations of air annealing effects on the defect and device characteristics of chalcopyrite solar cells. Herberholz *et al.* [21] obtained results from air annealing experiments on  $\text{CuInSe}_2$  that supported the interpretation of the N1 signature to be evoked by minority defect states at the buffer/absorber interface. The authors found that the activation energy  $E_a$  of the signature N1 analyzed by TAS and DLTS increases continuously with increasing duration of air annealing the device at 200 °C while the activation energy of a second signature named N2 remained constant. For an interface defect the activation energy corresponds to the energetic distance between the Fermi level and the conduction band at the interface. According to this, the authors explained the increasing activation energy of N1 by a passivation of compensating donors at the interface by oxygen causing a shift of the Fermi level position at the interface towards mid gap [21, 44]. Especially the donor state  $V_{\text{Se}}$  and the acceptor state  $\text{Cu}_{\text{In}}$  can be assumed to be present at grain boundaries and surfaces [94]. The neutralization of such donor states at the buffer/absorber interface by oxygen may be beneficial for the device performance due to decreased interface recombination via these defects. On the other hand, the passivation of the positive surface charge established by these states may reduce the type inversion at the heterojunction so that interface recombination becomes more probable. Accordingly, a counterbalance of both, the beneficial and the detrimental effect of oxygenation of interface states is imaginable [44].

As mentioned in Section 2.3 the origin of N1 is controversial discussed in literature and the validity of the defect model described above is not definitely proven. Nevertheless, the  $CV$  profiling method and air annealing experiments are employed for the identification of N1 by comparison of the observed effects with those reported by other authors on N1 in  $\text{Cu}(\text{In,Ga})\text{Se}_2$  devices.

### 6.3.1 Influence of the CV Test Frequency on Apparent Doping Distributions

In this section apparent charge profiles are discussed with regard to the signature D1 from HZB solar cells and the signature Q2 from Solteature devices with  $\text{CuInS}_2$  absorbers. Regardless of the individual RTP parameters, the D1 signature was observed in all HZB samples investigated by TAS which applies to the Q2 signature in the

SO samples as well. The results reported in this section were observed on several samples and are discussed using the examples of H2VT-2 and SO-2.

$CV$  measurements were performed at a temperature where the respective signature is well pronounced within the  $Cf$  spectrum using a high frequency (HF) and a low frequency (LF) relative to the inflection point of the capacitance step. In Fig. 6.18 (a) the  $Cf$  spectrum of sample H2VT-2 is presented which offers the selection of appropriate measurement parameters for the investigation of the D1 signature. The highlighted  $Cf$  curve measured at  $T = 192$  K completely covers the D1 capacitance step. At this temperature, the chosen frequency  $LF = 50$  Hz is sufficiently low to allow for a dynamic defect response of D1 to the test signal whereas the use of  $HF = 8$  kHz is high enough to eliminate its dynamic contribution to the capacitance. It should be noted, that for the selection of appropriate frequencies the derivative of the  $Cf$  curve was additionally regarded to distinguish between two steps within the spectrum.

During the  $CV$  measurements the voltage sweeps were performed sufficiently slow compared to the emission rates indicated by the investigated capacitance steps with integration times of up to one second. This slow profiling ensures that the charge of both, doping states at the edge of the depletion region and the static charge from deep states at  $x_1$  (see Fig. 3.5) contribute to the derived charge profile even at high test frequencies. A voltage range of  $V_a = -0.6 \dots 0.8$  V and an ac-amplitude of 30 mV were applied.

The apparent charge distributions presented in Fig. 6.18 (b) are derived from  $CV$  curves measured at  $T = 192$  K with HF and LF ac-modulation, respectively, using Equation (3.35). Towards low profile depths  $\langle x \rangle$  the apparent charge density increases due to increased minority carrier injection at forward bias. In this range, however, the assumption of a parallel circuit  $C_p - R_p$  becomes inappropriate because the relation  $R_S \ll R_P$  is no longer valid. An increased influence of the series resistance overestimates the spatial coordinate and the apparent charge density  $N$  [69]. Therefore, this part of the profile will be neglected in the following discussion.

For both profiles the apparent charge density increases towards higher  $\langle x \rangle$  values due to the occupation of deep defect levels by electrons with increasing voltage-induced band bending (see Section 4.4). Furthermore, a step is observed in both profiles at  $\langle x \rangle = 130$  nm (LF) and  $\langle x \rangle = 160$  nm (HF), respectively. Generally, discontinuities within a profile are not necessarily caused by inhomogeneous doping or trap distributions: As shown by Cwil *et al.* [20] a step in the profile can occur if an intersection of a deep bulk defect level with the Fermi level depends on the band bending. While the defect level could lie completely above the Fermi level at low band bending, it might start to intersect the Fermi level within increasing band bending. As a consequence, its voltage-depending contribution to the measured capacitance could generate a step in the  $N$ -profile. Accordingly, the interpretation of discontinuities in the profile has to be handled with care and cannot be definitely ascribed to gradients in the doping or defect concentration.

To facilitate the comparison of the HF and the LF profile, the profile HF\* (solid black line) in Fig. 6.18 (b) is derived from the HF profile in the following way: First, the distance  $w_n$  is subtracted from the depth scale of the HF profile. From this new depth scale a corresponding capacitance is calculated using Equation (3.36). These capaci-

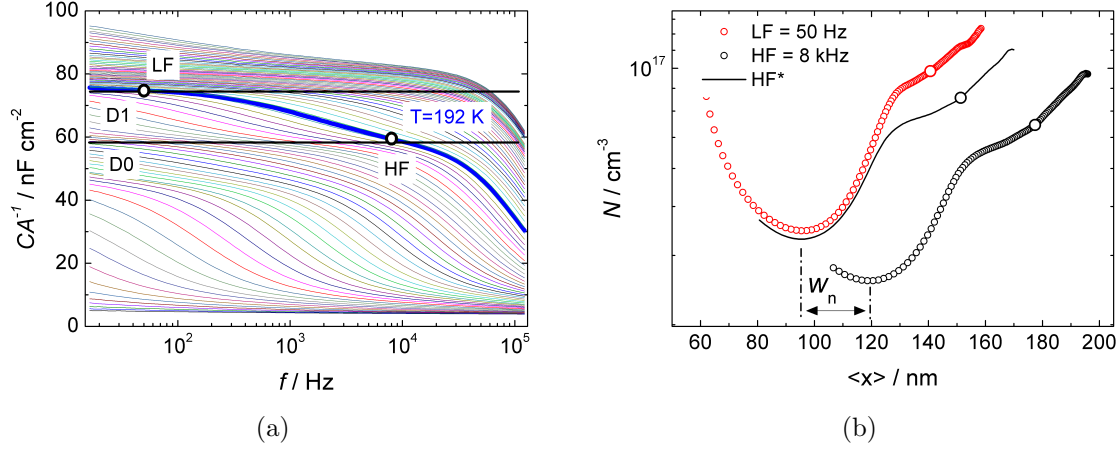


**Fig. 6.18:** (a)  $Cf$  spectrum for the HZB sample H2VT-2 and choice of a high frequency (HF) and a low frequency (LF) relative to the inflection point of signature D1 (b) Charge profiles derived from  $CV$  measurements on H2VT-2 at 192 K with LF = 50 Hz and HF = 8 kHz. The HF\* profile is calculated from the HF profile as described in the text. Big open circles indicate the data points corresponding to  $V_a = 0$  V. The assignment of sample IDs is given in Table 5.1.

tance values are combined with the original voltage scale to calculate the HF\* profile. Proceeding this way, Cwil *et al.* [20] found that the calculated HF\* profile merges the LF profile regarding N1 in Cu(In,Ga)Se<sub>2</sub>. As a consequence of their considerations described above, they concluded that the N1 signature is evoked by an interface defect. In Fig. 6.18 (b) the LF and the HF\* profiles only coincide for  $\langle x \rangle < 120$  nm. Consequently, the interpretation of D1 as a pure interface defect can be excluded. However, according to the coincidence of the profiles at low  $\langle x \rangle$ -values, D1 could rather be assigned to a bulk defect level that is also present at the heterointerface as sketched in Fig. 6.14. With increasing forward bias the intersection point of the Fermi level and the defect level would move closer to the interface. Nearby the interface it may provoke the same effects with respect to the apparent charge profiles as expected by pure interface traps. At high  $\langle x \rangle$ -values the LF profile does not approach a constant value although the low ac-modulation frequency allows for a dynamic capacitance contribution of the D1 bulk defects that should be independent of the applied voltage. Accordingly, additional deep bulk defects with even lower carrier emission rates may exist in the absorber that account for the increase in  $N$ . On the other hand, an inhomogeneous defect or doping distribution could be responsible for a gradient in the charge distribution.

Concerning the interpretation of the D1 signature, it should be reminded that D1 was assigned to a minority defect in Section 6.2.1. This supported the assumption of a relation between D1 and N1. Although D1 cannot be assigned to a pure minority interface defect analogous to the conclusions by Cwil *et al.* regarding N1, a correlation between both signatures remains possible: The interpretation of D1 as a minority bulk defect level close to the interface which is suggested here has also been considered by some authors in literature with regard to N1 [49, 76].

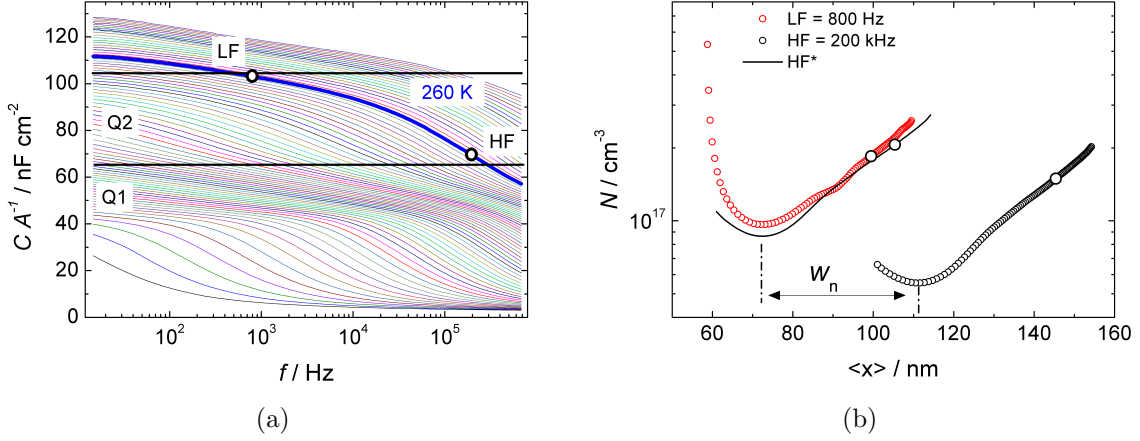


**Fig. 6.19:** (a)  $Cf$  spectrum for the Soltecture sample SO-2 and choice of a high frequency (HF) and a low frequency (LF) relative to the Q2 capacitance step. (b) Charge profiles derived from  $CV$  measurements on SO-2 at 260 K with LF = 800 Hz and HF = 200 kHz and the calculated HF\* profile. Big open circles indicate the data points corresponding to  $V_a = 0$  V. The assignment of sample IDs is given in Table 5.1.

In Fig. 6.19 (a) the  $Cf$  spectrum of the Ga-free SO-sample is shown. The temperature  $T = 260$  K and the frequencies LF = 800 Hz and HF = 200 kHz are selected for the investigation of the signature Q2 by  $CV$ -profiling. For choosing these frequencies also the derivative presentation of the  $Cf$  curve was taken into account.

The apparent charge profiles derived from  $CV$  profiling performed at HF and LF relative to the Q2 capacitance step at  $T = 260$  K are shown in Fig. 6.19 (b). Analogous to the description given for sample H2VT-2, a HF\* profile is calculated from the HF profile. It reveals that the shape of the HF and the LF profiles is approximately equal. The deviation in the vicinity of the minimum is presumably caused by an influence of the series resistance at forward bias: Since the influence of the series resistance additionally gains with increasing frequency [69], the distortion of the HF profile may be differently pronounced. At  $\langle x \rangle \approx 90$  nm a step is weakly indicated in the LF profile which is not visible in the HF profile. As explained above for sample H2VT-2 the interpretation of discontinuities within the profile has to be handled with care. Furthermore, if an increased series resistance at high test frequencies distorts not just the region at low  $\langle x \rangle$ -values but the complete profile, the discontinuities observed in the LF profile could be superimposed by this effect in the HF profile. However, the similarity between the overall shape of both profiles suggests that the signature Q2 is evoked by an interface defect and could be related to N1. In contrast to the D1 signature observed in the HZB samples, the TAS results of SO samples reported in Section 6.2.2 did not reveal if Q2 corresponds to a minority or to a majority defect, respectively. Indeed, the interpretation of Q2 as an interface defect implies that the activation energy  $E_a = 300$  meV of Q2 indicates the energetic distance between the Fermi level and the CBM of the buffer at the interface. Since the Fermi level is expected to intersect the interface in the upper half of the interface band gap, Q2 can be attributed to a minority interface defect.

In the  $Cf$  spectra shown in Fig. 6.18 (a) and 6.19 (a), also the signatures D0 and Q1 are indicated, respectively. While D0 was assigned to a majority bulk defect in Section 6.2.1, the classification of Q1 remained open. For both signatures HF and LF profiles were derived from  $CV$  profiles. The measurements had to be performed in a very low temperature range at which the influence of the series resistance was too strong to allow for a reliable analysis. A shift of the HF profile to higher values of  $N$  as compared to the LF profile was obtained which cannot be explained by means of defect physics.

### 6.3.2 Air Annealing Experiments

Air annealing experiments on  $\text{Cu(In,Ga)Se}_2$  solar cells in the dark were shown to result in an increase of the N1 activation energy by several researchers [21, 44, 95]. As outlined to the beginning of Section 6.3, the authors concluded from their results, that N1 can be assigned to an interface defect. Furthermore, changes in the device characteristics were observed. These included an increase in the width of the space charge region  $x_d$  which correlated with a decrease of  $V_{oc}$ . Rau *et al.* [44] attributed the losses in  $V_{oc}$  to an enhanced recombination via defect states in the widened space charge region. However, they noted that the decrease in  $x_d$  does not conform to the oxygenation model, since a passivation of compensating donors is rather expected to increase the net doping resulting in a narrowed space charge region. The authors suggested that the widened SCR could be explained by  $\text{Cu}^+$ -ions that were released upon annealing and moved towards the absorber bulk enforced by the electric field of the SCR.

In this section, the effect of air annealing on the TAS spectra and the device characteristics of sulfur-based solar cells are investigated. Based on the findings in Section 6.3.1, changes in  $E_a$  of the signatures Q2 in the Ga-free Soltecture samples and D1 in the HZB samples are of special interest: Q2 was interpreted as a minority interface defect whereas D1 was rather assigned to a minority bulk defect that could also be present at the heterointerface. For both of them, a relation to N1 was considered to be possible. The changes of device parameters due to air annealing are investigated by means of  $IV$  curves,  $EQE$  spectra and  $IVT$  measurements. The results are discussed in the context of the N1 signature and the air annealing effects on selenium-based devices reported by Herberholz *et al.* and Rau *et al.* [21, 44].

Ga-free Soltecture samples and HZB samples are investigated in this section, whereas the Ga-doped Soltecture samples are excluded due to the overlap of the signatures P1 and P2 in the TAS spectrum that complicated a consideration of their individual characteristics. Within the scope of this work the experiments had to be restricted to one exemplary sample of each absorber type. The most important criterion for the selection of these sample was that the signature D1 and Q1 were significantly pronounced in the TAS spectrum, respectively. All measurements were performed on the samples prior to the annealing procedure ("as grown" condition) and after annealing in ambient air in the dark on a hot plate at 200°C<sup>7</sup>. Regarding the dwell times of the

<sup>7</sup>The annealing temperature  $T = 200^\circ\text{C}$  is equal to the temperature applied by Herberholz *et al.* and Rau *et al.* in their annealing experiments on  $\text{Cu(In,Ga)Se}_2$  devices [21, 44].

annealing some statements have to be made:

As reported in literature, the extent of the annealing effects observed on selenium-based devices depend on the annealing temperature as well as the dwell time [21, 44, 95]. In consideration of the dwell times reported there and with intent to observe significant changes in the defect and device characteristics, a dwell time of one hour was chosen for annealing the HZB sample H3HT-2. The TAS spectrum of this sample was already discussed in Section 6.2.1. As will be shown in this section, the TAS spectrum and the device characteristics of H3HT-2 changed dramatically upon this annealing procedure. Unfortunately, the attempt to perform the annealing experiment on a Solteature sample with the same annealing dwell time as used for H3HT-2 resulted in a shunted device. Therefore, the experiment was repeated with shorter annealing durations of one minute in a first step and further 5 minutes in a second step on the sample SO-1. After a third annealing step of additional 15 minutes, this sample was shunted. It should once more be emphasized, that all SO samples offered similar device characteristics and TAS spectra. Accordingly, the TAS spectrum of sample SO-1 prior to air annealing was very similar to that shown for SO-2 in Section 6.2.2. Presumably due to the low annealing duration used for SO-1 compared to the HZB sample, the observed changes of the device characteristics and the  $E_a$  of SO-1 are less pronounced than those found for H3HT-2.

### Air Annealing Effects on TAS Spectra

The presence of the N1 signature in sulfur-based devices might be further confirmed by an increase of its activation energy upon annealing in the dark in ambient atmosphere. Such behavior was observed by several researchers for the N1 level in  $\text{Cu}(\text{In,Ga})\text{Se}_2$  devices [21, 44, 95]. In this thesis, such phenomenon was verified for the samples H3HT-2 and SO-1.

For sample SO-1 only little changes are induced to the TAS spectrum upon air annealing for 1 minute and additional 5 minutes. No significant deviations were found for signature Q1 whereas a slight increase of the activation energy of about 20 meV is observed for signature Q2 (Fig. 6.20 (a)) which points to an N1-like origin of Q2. From the capacitance level above the "freeze-out" step in the  $Cf$  spectrum a reduction of the width of the space charge region is evaluated from  $x_d = (246 \pm 6)$  nm in the as grown state to  $(227 \pm 5)$  nm and  $(223 \pm 5)$  nm after air annealing for 1 minute and additional 5 minutes, respectively. In accordance with Equation (3.30) a reduction of  $x_d$  is attended by an increased net doping concentration. Following the oxygenation model, the increase in net doping can be a consequence of the passivation of compensating minority defects by oxygen [94].

In the Arrhenius plot shown in Fig. 6.20 (b) the signatures of the HZB sample H3HT-2 in the as grown condition are compared to the signatures identified after air annealing the sample for one hour at 200 °C on a hot plate. As described in Section 6.2 the signature D2 is only very weakly pronounced in the TAS spectrum of sample H3HT-2. Thus, only the signatures D0 and D1 with activation energies of 170 meV and 370 meV are shown for the as grown sample, respectively. From these signatures, D1 was con-

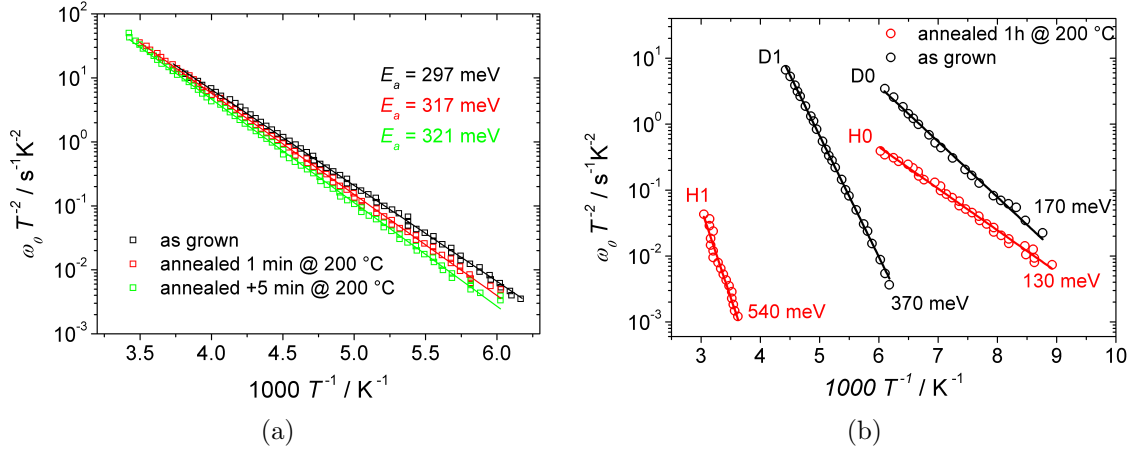


**Fig. 6.20:** Arrhenius plot for (a) the signature Q2 of the Soltecture sample SO-1 before air annealing and after repetitive air annealing for one minute and additional five minutes, respectively, and for (b) the HZB sample H3HT-2 before and after annealing the device for one hour in ambient air. The assignment of sample IDs is given in Table 5.1.

sidered to be related to N1 in Sections 6.2.3 and 6.3.1. The annealing procedure leads to radical changes in the TAS spectrum. A signature with  $E_a = 130$  meV and a weakly pronounced but evaluable signature with  $E_a = 540$  meV appear, denoted as H0 and H1, respectively, while the presence of the former levels D0, D1 or D2. If the D1 signature corresponds to N1, a shift of its activation energy to higher values after air annealing could be indicative for a common origin of D1 and H1.

To verify a relation between the signatures shown in Fig. 6.20 (b) for sample H3HT-2 before and after the annealing procedure, the results are added to a Meyer-Neldel plot in Fig. 6.21 including parts of the data already presented in Section 6.2.3. For a clear presentation, the signatures D1 and H1 and the signatures D0 and H0 are pairwise examined in Fig. 6.21 (a) and (b), respectively.

While the signature D1 of the as grown sample H3HT-2 matches well the N1 line in Fig. 6.20 (a), a relation of the signature H1 observed in the annealed sample to N1 is rather excluded. In contrast, the defect characteristics of H1 fit better to the MN-Plot of N2 (and thereby also to D2, as discussed in Section 6.2.3). It has to be concluded that air annealing removes the signature D1 from the TAS spectrum while it enforces the occurrence of the signature H1 which was already weakly indicated in the TAS spectrum of the as grown sample. According to the oxygenation model the absence of D1 after annealing may be caused by a shift to an activation energy which is too high to be detected by TAS. On the other hand, the defects which provoked the signature could be completely neutralized by oxygenation or their concentration could be reduced to a value that is below the detection limit of TAS.

From the  $Cf$  spectra of the as grown and the annealed sample H3HT-2 a reduction of the width of the space charge region from  $x_d = (249 \pm 6)$  nm to  $x_d = (197 \pm 4)$  nm could

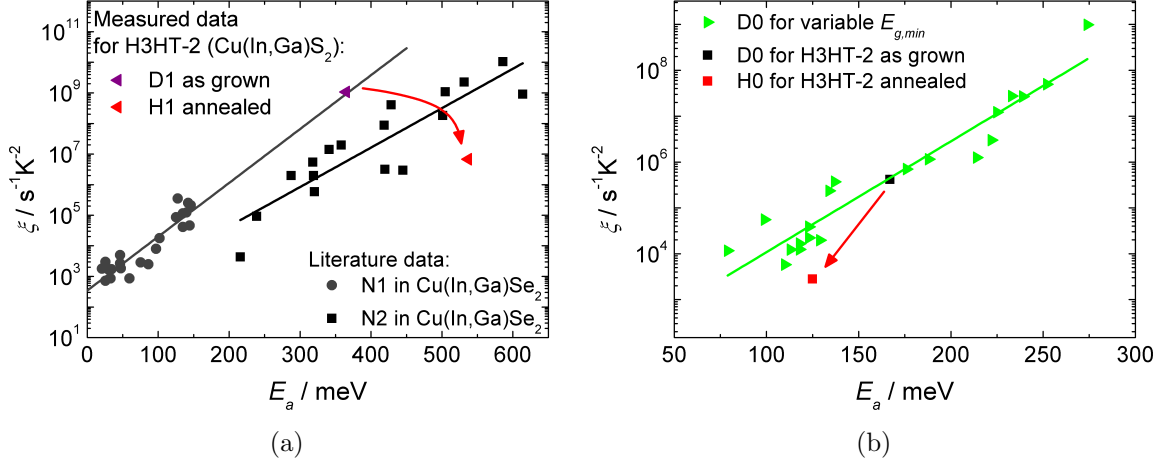


**Fig. 6.21:** Meyer-Neldel plots for comparison of the signatures derived from the TAS spectrum of sample H3HT-2 before and after air annealing the sample for one hour at 200 °C. In (a) the signature H1 from the annealed sample is compared to data on D1 from the as grown sample and literature data on N1 and N2 in Cu(In,Ga)Se<sub>2</sub> devices as already presented in Fig. 6.17. In (b) the data of signature H0 from the annealed sample is compared to D0 from the as grown sample and further HZB samples with various  $E_{g,min}$ . The assignment of sample IDs is given in Table 5.1.

be derived. As described for SO-1, this is in accordance with the oxygenation model which suggests a passivation of compensating donor states resulting in an increased net doping concentration [94]. Although an increased doping could generally be expected to increase the band bending, a passivation of positive charge at the interface could reduce the type inversion at the interface. As a consequence, the Fermi level could be moved towards mid gap and the band bending would be rather decreased. Based on this thought, a relation could exist between the signatures D0 and H0 of the as grown and the annealed sample, respectively: In case of a reduced band bending the intersection point of the Fermi level and the D0 level could have moved closer to the interface. At a position closer to the interface the Ga-concentration could be lower which could account for a reduced  $E_a$  of D0 (see Section 6.2.1). In Fig. 6.21 (b) the signature H0 of the annealed sample H3HT-2 is compared to the TAS results of the signature D0 identified in various HZB samples with different  $E_{g,min}$ . Due to the position of the H0 data point within the MN-plot, no clear relation to D0 can be stated. Already the position of the signature H0 within the Arrhenius plot in Fig. 6.20 (b) casts doubt on a common origin of H0 and D0 because it does not fit to the trend given by the data of D0 observed on samples with different  $E_{g,min}$  as shown in Fig. 6.12. There, the D0 curves with lower slope lie above the curves with higher slope and intersect at a value higher than  $\omega_0/T^2 = 1$ . In contrast, the intersection point of the Arrhenius data of H0 and D0 would be located at a value below  $\omega_0/T^2 = 10^{-2}$  in Fig. 6.20 (b).

In summary, for both samples a reduced space charge width upon air annealing is observed which is explained by a passivation of compensating donors within the oxygenation model. For the SO-1 sample such an effect could be indicated by the increase

in  $E_a$  of the signature Q2 which corresponds to the result observed by Herberholz *et al.* and Rau *et al.* [21, 44] regarding N1. Accordingly, the assumption of a relation between Q2 and N1 as well as its interpretation as an interface defect is further supported. Since the TAS spectrum of the annealed sample H3HT-2 did not reveal a signature that could be related to D1, this signature cannot be definitely assigned to N1 in this thesis.

### Air Annealing Effects on Device Characteristics

Besides the shift of the activation energy of defect states at the buffer/absorber interface, further changes caused by air annealing may be observed in the device characteristics. Following the model described in [21, 44] an increase of the net doping concentration and a decreased width of the space charge region is expected as a consequence of the neutralization of donor states. Indeed, a decrease in  $x_d$  was confirmed for both investigated samples in this work as described above. However, a passivation of donor states at the interface could result in a reduced type inversion and thereby enhance recombination losses via interface defects. As mentioned in the introduction of this section, the results presented in [21, 44], revealed an increase of the SCR width instead of a decrease which does not conform to the oxygenation model. As demonstrated by their work, the results of air annealing can be puzzling and do not necessarily fulfill all the expectations given by the oxygenation model. In the following, the effects of air annealing on the device characteristics are discussed, based on results from *IVT*, *IV* and *EQE* measurements.

In Fig. 6.22 the *IV* curves measured at STC before and after air annealing the samples SO-1 (a) and H3HT-2 (b) are compared. In case of the Soltecture sample SO-1, air annealing for one minute leaves the *IV* curve essentially unchanged. Additional five minutes of air annealing reduces the fill factor from 71 to 66 %. For the HZB sample H3HT-2, air annealing for one hour causes, however, considerable changes in the *IV* characteristics. The  $V_{oc}$  and the  $J_{sc}$  are reduced by 170 mV and 1.9 mA/cm<sup>2</sup>, respectively. Additionally, the fill factor is lowered from 73 % to 37 %.

In the previous discussion on the TAS spectra, a reduced width of the space charge region upon air annealing was reported for both samples which is in accordance with an increased net doping concentration. Generally, an increased doping concentration would be expected to enhance the  $V_{oc}$ . On the other hand, a passivation of donors at the interface could have reduced the type inversion. This would support recombination via interface defects and accordingly explain the decreased  $V_{oc}$  of sample H3HT-2 upon air annealing. Furthermore, the narrowed space charge region impedes the collection of charge carriers generated deeper in the neutral bulk which results in the decreased  $J_{sc}$  of sample H3HT-2. The decreased fill factor supports this argument as it indicates that the current collection efficiency becomes impeded under increasing forward voltage which further reduces the width of the space charge region. The fact that for sample SO-1 the  $V_{oc}$  and the  $J_{sc}$  remain unaffected by the air annealing procedure can be attributed to the much lower annealing duration compared to sample H3HT-2. On the other hand, a trade-off may exist between the beneficial and the detrimental effects of oxygenation - the saturation of interface defects impeding recombination losses via these

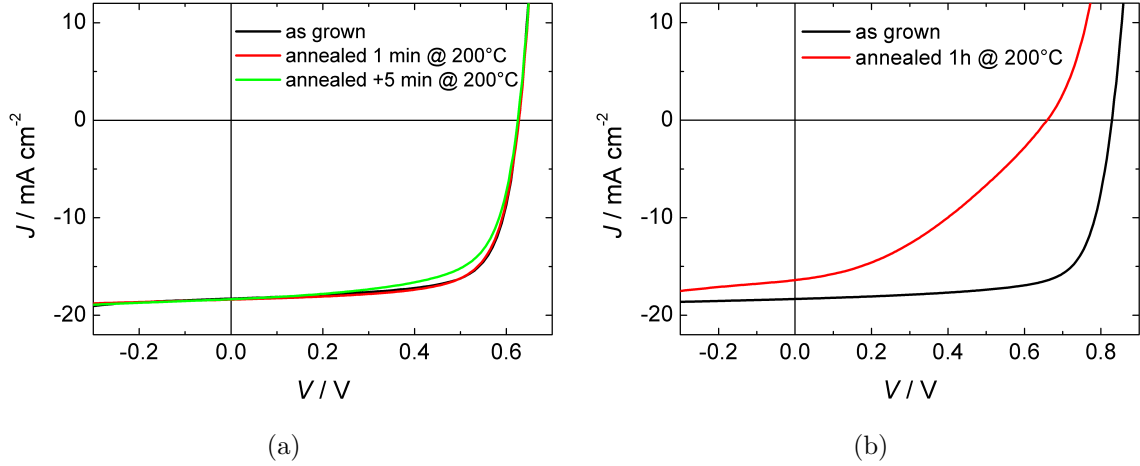


**Fig. 6.22:** *IV* characteristics presenting the effect of air annealing for (a) the Soltecture sample SO-1 annealed for one minute and additional five minutes, respectively, and (b) the HZB sample H3HT-2 annealed for one hour. The assignment of sample IDs is given in Table 5.1.

states and the reduction of the type inversion supporting interface recombination. Since the  $J_{sc}$  remains unaffected by the annealing procedure, the effective diffusion length of the charge carrier generated in the neutral bulk still seems to be sufficient to reach the space charge region at  $V = 0$  V. However, the reduced fill factor after the second air annealing step indicates that under load conditions the reduced width of the space charge region limits the current collection efficiency.

A more detailed investigation of air annealing effects on the current is facilitated by *EQE* spectra of the as grown and annealed samples presented in Fig. 6.23. For both samples, the deviations between the *EQE* spectra in the as grown condition and the annealed condition are small and vary within the error of the measurement. Especially the inhomogeneity of the samples complicates the reproducibility of the measurement, although it was attempted to perform the *EQE* measurement at the same local position of the respective samples in the as grown and annealed state, respectively. As already discussed in Section 6.1.1 the differences between values for  $J_{sc}$  obtained from *EQE* spectra and *IV* measurements can arise from deviations in the solar spectrum of the light source used for the *IV* measurements and errors in the determination of the sample area. Furthermore, the presence of photons over a wider spectrum during the *IV* measurements may lead to a different conditioning of the sample compared to the situation during *EQE* experiments, where the sample is illuminated with monochromatic light. For instance, the occupation of metastable defect states may significantly influence the respective results.

The influence of air annealing on the temperature dependence of the open circuit voltage is demonstrated for both samples in Fig 6.24. For sample SO-1 the activation energy  $E_A$  derived from the extrapolation of the  $V_{oc}$  values at  $T > 260$  K to  $T = 0$  K varies slightly between the as grown condition and the two successively annealed conditions within 60 meV, but the changes do not correlate with the annealing duration (Fig. 6.24(a)).

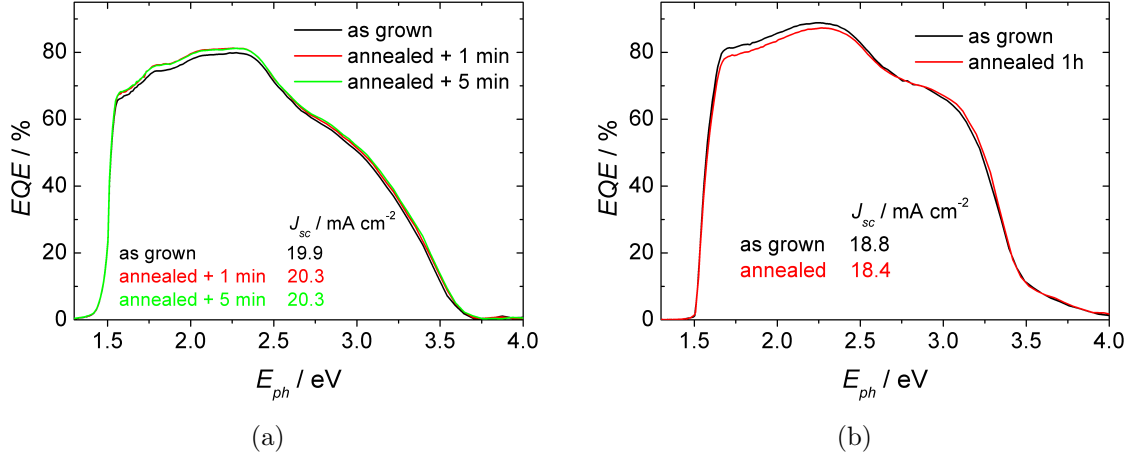


**Fig. 6.23:** *EQE* spectra presenting the effect of air annealing for (a) the Soltecture sample SO-1 annealed for one minute and additional five minutes, respectively, and (b) the HZB sample H3HT-2 annealed for one hour. The assignment of sample IDs is given in Table 5.1.

On the contrary, a significant reduction of the activation energy by  $E_A = 180$  meV is found between the as grown and the annealed state for sample H3HT-2 (Fig. 6.24(b)). Within the oxygenation model, a decrease of  $E_A$  may occur due to a reduced type inversion at the interface. This would imply a reduced band bending leading to a reduced interface band gap  $E_{g,i}$  (see Fig. 2.5). If the Fermi level is pinned, the activation energy measures the distance between the valence band edge and the Fermi level at the interface. Also in this case,  $E_A$  should be reduced because the Fermi level is shifted closer to mid-gap position. Considering the data points at  $T < 270$  K the curve exhibits an abnormal shape compared to other *IVT* results presented in this work and in literature: Commonly, the  $V_{oc}$  is observed to drop below the linear fit for high temperatures. This differing behavior could result from metastable defect states evoked by the air annealing procedure since a slight decrease in  $V_{oc}$  was already observed at room temperature for repeated *IV* measurements. Due to repeated illumination at each temperature step, this effect may proceed during the entire measurement which runs from low to high temperatures. A very careful and comprehensive analysis of this metastable behavior would be required to confirm such mechanism which would go beyond the scope of this work.

In summary, the annealing experiments revealed similar but differently pronounced phenomena regarding the solar cell characteristics of sample SO-1 and H3HT-2: For both samples, the reduced width of the space charge region results in a reduced fill factor. The reduced activation energy  $E_A$  of sample H3HT-2 derived from *IVT* measurements points to a reduced type inversion which accounts for the reduced  $V_{oc}$  of this sample. Within the oxygenation model, the reduced type inversion can be explained by a passivation of donor states at the interface. The fact that the annealing-induced changes observed on sample SO-1 are less significant compared to sample H3HT-2 is presumably a consequence of the very different annealing durations for both samples.

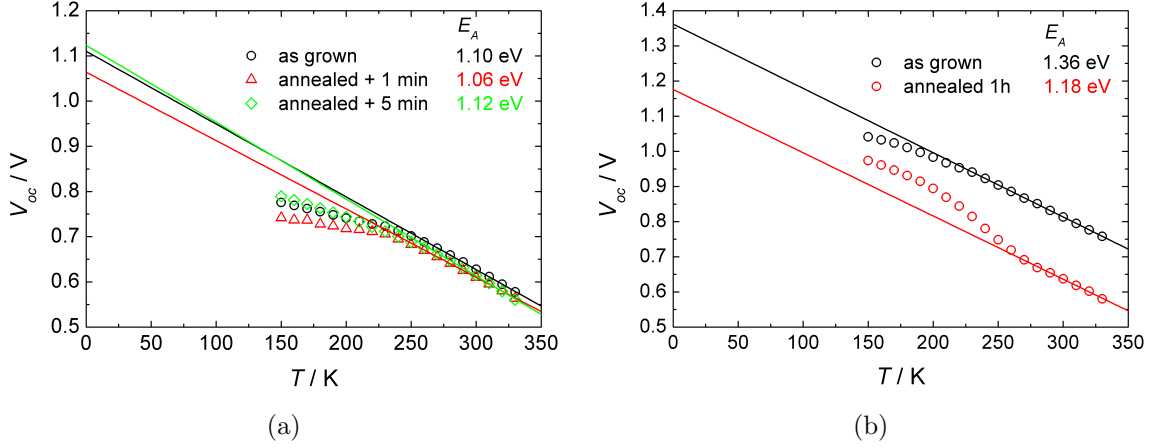


**Fig. 6.24:** Evaluation of the activation energy  $E_A$  of the saturation current density from extrapolation of the temperature-dependent open circuit voltage to  $T \rightarrow 0$  K for (a) the Soltecture sample SO-1 before air annealing and after repetitive air annealing for one minute and additional five minutes, respectively, and (b) the HZB sample H3HT-2 before and after annealing the device for one hour in ambient air. The assignment of sample IDs is given in Table 5.1.

Furthermore, the samples stem from different processes and manufacturers so that their sensitivity to air annealing may be generally different. Generally, the observation of air annealing effects is not self-evident, especially on sulfur-based devices: Annealing experiments performed on  $\text{CuInS}_2$  solar cells were already reported in [96] where changes in the defect structure were investigated by photoluminescence spectroscopy. No changes were found in the PL spectra after annealing the devices in ambient air or oxygen atmosphere. In contrast, annealing in  $\text{H}_2$  atmosphere revealed an increased donor acceptor transition which the authors ascribed to an increase of donor states  $V_S$  by removing oxygen from the interface states. Accordingly, a device may be insensitive to oxygenation because oxygen is already present within the material. The observation of air annealing effects on  $\text{Cu}(\text{In,Ga})\text{S}_2$  solar cells may additionally be hindered by the fact that the chalcopyrite of these devices is grown under Cu-rich conditions. Cahen and Noufi argued that in these devices  $\text{Cu}_{\text{In}}$  acceptors may appear which neutralize the  $V_S$  donors via Coulombic attraction [94].

### 6.3.3 Conclusions III

Based on its mapping within the Meyer-Neldel plot in Section 6.2.3, the signatures D1 and Q2 observed in Ga-doped HZB samples and Ga-free Soltecture samples, respectively, were considered as possibly related to the N1 signature in  $\text{Cu}(\text{In,Ga})\text{Se}_2$  devices.  $CV$  measurements at high and low frequencies with regard to the transition rate of these signatures revealed the following results:

- The D1 signature does presumably not originate from pure interface defects but rather from a minority bulk defect which is also present at or close to the buffer/absorber interface. Such an origin was also suggested for the N1 feature in

selenium-based compounds in [49, 76]. However, the result is not in accordance with the findings reported by Cwil *et al.* [20] so that the question if D1 is related to N1 remains open.

- The signature Q2 in Soltecture samples can be attributed to an interface defect. As the results are similar to those reported by Cwil *et al.* regarding N1, the assumption that Q2 may be related to N1 is supported.

The following conclusions can be drawn from the results of air annealing experiments on the samples SO-1 and H3HT-2:

- The shift in  $E_a$  of the signature Q2 in sample SO-1 corresponds to a typical effect which is known from N1 in Cu(In,Ga)Se<sub>2</sub> devices. This result complements the findings of N1 indicative properties of Q2 by means of the Meyer-Neldel mapping (Section 6.2.3) and *CV* profiling.
- The narrowed depletion region and the reduced fill factor observed for both samples are compatible with the oxygenation model which suggests the passivation of compensating donors.
- The absence of D1 within the TAS spectrum after annealing sample H3HT-2 in addition to the inconclusive results from the *CV* measurements hinders a clear assignment of this signature to N1.
- Nevertheless, the reduction of the depletion region and the fill factor are in qualitative conformance with the oxygenation model also for sample H3HT-2. Furthermore, the lowered  $V_{oc}$ ,  $J_{sc}$  and  $E_A$  values derived from (temperature-dependent) *IV* curves strengthen the assumption of a common mechanism of the air annealing effects on this Cu(In,Ga)S<sub>2</sub> sample and those observed on selenium-based devices.



## 7 Conclusions and Outlook

Cu(In,Ga)S<sub>2</sub> solar cells involving varied Ga depth profiles as a consequence of differently performed rapid thermal processing (RTP) of metallic precursors were investigated. The minimum band gap energy  $E_{g,min}$  determined via  $EQE$  measurements revealed that high temperatures are required during the sulfurization step to support diffusion of Ga from the back of the precursor film towards the absorber surface. Using  $E_{g,min}$  as an indicator for the Ga-concentration at the absorber surface, device characteristics obtained from (temperature-dependent) current-voltage  $IV(T)$  measurements and defect characteristics derived from thermal admittance spectroscopy (TAS) were analyzed with regard to the influence of the surface-near Ga-concentration.  $IV$  measurements revealed an increase of  $V_{oc}$  with increasing  $E_{g,min}$  but these values lie significantly below the trend of  $V_{oc}$  versus  $E_{g,min}$  reported for Cu(In,Ga)Se<sub>2</sub> devices in literature. A negative conduction band offset (cliff) at the buffer/absorber interface supports interface recombination as the predominant loss mechanism limiting the  $V_{oc}$  of sulfur-based devices. This could be confirmed by  $IVT$  measurements for the samples investigated in this work. However, due to the cliff-like band offset the increase in  $V_{oc}$  by incorporation of Ga is unlikely to result from an up-shift of the CBM in an analogous manner to the effect of Ga in Cu(In,Ga)Se<sub>2</sub> devices. From  $IVT$  measurements a linear increase of the activation energy of the recombination current  $E_A$  with  $E_{g,min}$  could be derived. This result provided a first indication that a down-shift of the VBM could be evoked with increasing Ga-concentration in sulfur-based chalcopyrites.

While the investigation of defects in selenide-devices revealed important information about  $V_{oc}$ -limiting recombination centers in the past, less effort was made to study defects in sulfur-based solar cells. This work therefore aimed at contributing new information about defects in Cu(In,Ga)S<sub>2</sub> devices with regard to the influence of Ga. Since recombination losses at the interface had been identified to limit the  $V_{oc}$  of the investigated samples, the identification of interface defects that may be involved appeared to be of high interest. Generally, TAS measurements do not allow for a direct assignment of the observed signatures to interface/bulk and majority/minority defects. However, the cliff-like conduction band offset enables such an assignment by taking correlations observed between the derived defect activation energies and the Ga-concentration at the heterojunction into account (see Table 7.1). A direct correlation was found between the  $E_{g,min}$  of HZB samples with widely varied Ga-depth distributions and the activation energy  $E_a$  of the signature D0. Based on this finding and the presence of a cliff, D0 could be assigned to a majority bulk defect. Simultaneously, Ga-induced lowering of the VBM in Cu(In,Ga)S<sub>2</sub> was confirmed. This key result is contradictory to the effect of Ga on the energy bands in Cu(In,Ga)Se<sub>2</sub> solar cells reported in literature and furthermore offers an explanation for the observed increase in  $V_{oc}$  with increasing Ga-concentration. As a consequence of the statements made for D0 and the effect of Ga

**Table 7.1:** Suggested assignment of defects and their respective activation energy  $E_a$  obtained by TAS to minority/majority, bulk/interface and N1/N2. The assignment of the defects to N1 and N2 is rated using the symbols ++ (very likely), + (likely), – (unlikely).

	signature	$E_a$ / meV	minority/	bulk/	assignment	
			majority	interface	N1	N2
HZB Cu(In,Ga)S <sub>2</sub>	D0	100 ... 250	majority	bulk	–	–
	D1	370	minority	bulk	+	–
	D2	380 ... 690		bulk	–	+
Soltecture CuInS <sub>2</sub>	Q1	130 ... 145			–	–
	Q2	300	minority	interface	++	–
Soltecture Cu(In,Ga)S <sub>2</sub>	P0	100 ... 115			–	–
	P1	270 ... 310			–	–
	P2	355 ... 420	minority		+	–

on the VBM, the signature D1 was interpreted as a minority defect at or close to the interface. Accordingly, D1 was considered to be possibly involved in the recombination losses at the interface. Another signature (D2) was observed in the TAS spectra of HZB samples. Since in most of the samples it occurred with an activation energy that is presumably too high to be covered by TAS, D2 could not be classified in this work. Nevertheless, D2 was found to be missing in samples stemming from a 3-step RTP process involving an especially high sulfurization temperature. Due to the fact that these samples also exhibit a higher  $V_{oc}$  compared to other samples of similar  $E_{g,min}$ , D2 was assumed to represent a  $V_{oc}$ -limiting defect.

In a Meyer-Neldel (MN) plot the defect characteristics of all signatures found in the investigated Cu(In,Ga)S<sub>2</sub> samples were compared to each other and to defects reported in literature for CuInS<sub>2</sub> and Cu(In,Ga)Se<sub>2</sub>, respectively. This mapping allowed to discuss also the origin of the signatures Q1 and Q2 (in CuInS<sub>2</sub>) as well as P0, P1 and P2 (in Cu(In,Ga)S<sub>2</sub>) obtained for Soltecture samples. According to the trend lines given by literature data on the prominent features N1 and N2 which are frequently observed in Cu(In,Ga)Se<sub>2</sub> devices, some of the signatures evaluated in this work could be related to N1 or N2, respectively (see Table 7.1). Since the discussion on N1 in literature

also involves the interpretation of N1 as an interface defect, signatures that could be related to N1 attracted special attention. Two of these candidates, Q2 and D1, were further investigated by means of  $CV$  measurements performed at different frequencies of the ac-voltage signal. From a comparison of the apparent doping profiles derived from high/low-frequency measurements, it could be concluded that the signature Q2 of Ga-free Solteature samples is evoked by an interface defect whereas the signature D1 of HZB samples was rather attributed to a bulk defect that is also present at the buffer/absorber interface. An air-annealing experiment was performed on a Ga-free Solteature sample and a HZB sample in order to investigate if changes in the defect spectra and the device characteristics occur which could be evoked by the oxygenation of interface defects. In both samples, a decreased width of the space charge region coming along with a decreased fill factor were found for both samples which is in qualitative correspondence to the oxygenation model proposed by Cahen *et al.* [94]. As the changes in the defect spectrum of the HZB sample were very drastic upon annealing the sample for one hour, a clear assignment between the signatures of the annealed and the as grown sample could not be made. However, an increase of  $E_a$  with increased annealing duration of the Solteature sample confirmed the assignment of Q2 to a minority interface defect and to N1. Accordingly, this interface defect could be responsible for the low  $V_{oc}$  values observed for the Ga-free Solteature samples.

The valuable information about defects and the influence of Ga on the energy bands in  $\text{Cu}(\text{In,Ga})\text{S}_2$  solar cells presented here could be extended by further investigations. Different  $V_{oc}$ -values were observed for some samples of similar  $E_{g,min}$  values. Besides the assumption that the deviations may be defect-related (as suggested in the context of D2), it was also discussed that inhomogeneities in the lateral Ga-distribution at the interface or a V-shape in the Ga-depth profile could exist in 3-step processed samples. Such a V-shape could not be verified by random EDX line scans in this work, but more comprehensive statistics would be needed to assess the interface-near Ga-profiles. Furthermore, a study on Ga-free samples could help to examine the influence of the sulfurization temperature on the defect contributions. It is imaginable that the high sulfurization temperature during the 3-step process leads to a reduced defect distribution at the interface which has to be regarded apart from the actual Ga depth profile.

As shown in this work, relations between defects obtained for the sulfur-based devices to those occurring in  $\text{Cu}(\text{In,Ga})\text{Se}_2$  solar cells are very likely. This can be considered as a chance to learn from the effects of defects in selenium-based devices. However, due to the differing recombination mechanisms observed in solar cells based on both absorber materials, the defects are expected to have a different impact on the performance of the respective solar cells. A systematic investigation of the signature D2 could clarify if this defect limits the  $V_{oc}$  in the HZB samples. In this respect, it is of particular interest, if D2 is related to an interface defect or if it is rather related to the bulk acceptor N2 in  $\text{Cu}(\text{In,Ga})\text{Se}_2$  as suggested by its mapping in the MN plot. This could be verified by processing the samples with different buffer materials or by characterization of appropriately prepared Schottky diodes. Changes in the TAS spectra with regard to D2 would suggest its interpretation as a defect at or close to the heterointerface. Such a study could furthermore verify the bulk/interface assignments of other defects as suggested in Table 7.1. As described in the beginning of Section 6.3.2 the air annealing

## 7 Conclusions and Outlook

experiments were restricted to two samples and few annealing cycles. However, an enhanced study with shortened dwell times may allow for a more systematic study of the oxygenation effects on the HZB samples. Additionally, it would be interesting to investigate if the observed annealing effects are reversible by means of annealing in H<sub>2</sub> atmosphere in accordance with results reported by Töpper *et al.* [96].

# List of Frequently Used Symbols

$\epsilon$ .....	relative permittivity
$\epsilon_0$ .....	permittivity of free space
$\langle x \rangle$ .....	depth coordinate, derived from low-frequency capacitance
$\omega$ .....	angular frequency $2\pi f$ of the applied ac voltage
$\omega_0$ .....	cutoff frequency of the low pass filter
$\overline{E}_{g,front}$ .....	average minimum band gap at the absorber surface
$\Phi_b^p$ .....	recombination barrier for holes at the buffer/absorber interface
$\rho$ .....	charge density
$\sigma_{n,p}$ .....	capture cross section for electrons, holes
$\xi$ .....	pre-exponential factor in the Arrhenius relation (Equation 3.18)
$\xi_0$ .....	pre-exponential factor in the Meyer-Neldel relation (Equations (4.10) and eq:MN-prefac)
$A$ .....	diode quality factor
$C$ .....	capacitance
$C_{geo}$ .....	geometrical capacitance
$c_{n,p}$ .....	capture rate for electrons, holes
$e$ .....	elementary electric charge
$E_A$ .....	activation energy of the saturation current density $J_0$
$E_a$ .....	defect activation energy
$E_g$ .....	band gap energy
$E_t$ .....	energy level of a deep defect state
$E_C$ .....	minimum conduction band energy
$E_F$ .....	Fermi energy
$E_{g,i}$ .....	interface band gap energy
$E_{g,min}$ .....	minimum band gap energy
$e_{n,p}$ .....	emission rate for electrons, holes
$E_{ph}$ .....	photon energy
$E_V$ .....	maximum valence band energy
$f$ .....	frequency of the applied ac voltage
$G$ .....	conductance
$I$ .....	current
$J$ .....	current density

## 7 Conclusions and Outlook

$J_0$ .....	saturation current density
$J_{sc}$ .....	short circuit current density
$k$ .....	Boltzmann constant
$N$ .....	charge density
$n$ .....	free electron concentration
$N_a$ .....	acceptor doping concentration
$N_d$ .....	donor doping concentration
$N_t$ .....	defect state density
$n_t$ .....	defect states occupied by electrons
$N_{C,V}$ .....	density of states of the conduction, valence band
$p$ .....	free hole concentration
$p_0$ .....	free hole concentration in neutral material on the p-side of a p-n junction
$R_P$ .....	diode parallel resistance
$R_S$ .....	diode series resistance
$T$ .....	temperature
$T_{sulf}$ .....	sulfurization temperature during RTP process
$V$ .....	band bending, $V = V_a + V_b$ , in Chapter 3
$V$ .....	voltage
$V_a$ .....	applied voltage bias
$V_b$ .....	built-in voltage
$V_{ac}$ .....	amplitude of the applied ac voltage
$v_{n,p}$ .....	thermal velocity of electrons, holes
$V_{oc}$ .....	open circuit voltage
$x_1$ .....	intersection of a deep trap level and the Fermi level
$x_d$ .....	width of the depletion region
$x_n$ .....	width of the depletion region on the n-side of the p-n junction
$x_p$ .....	width of the depletion region on the p-side of the p-n junction
$Y$ .....	complex admittance

# Bibliography

- [1] W. Shockley and H. J. Queisser, “Detailed Balance Limit of Efficiency of p-n Junction Solar Cells,” *Journal of Applied Physics*, vol. 32, no. 3, pp. 510–519, 1961.
- [2] I. Savova, “Europe 2020 Strategy - towards a smarter, greener and more inclusive EU economy?,” *Statistics in Focus (eurostat)*, vol. 39, 2012.
- [3] P. Würfel, *Physik der Solarzellen*. Spektrum Akademischer Verlag GmbH, 2 ed., 2000.
- [4] International Energy Agency, ed., *Key World Energy Statistics 2012*. IEA/OECD, 2012.
- [5] R. Scheer and H.-W. Schock, *Chalcogenide Photovoltaics - Physics, Technologies, and Thin Film Devices*. Wiley-VCH Verlag, 2011.
- [6] R. A. Mickelsen and W. S. Chen, “Development of a 9.4 % efficient thin-film CuInSe<sub>2</sub>/CdS solar cell,” *Proceedings of the 15th IEEE PVSC*, pp. 800–804, 1981.
- [7] A. Jager-Waldau, “Progress in chalcopyrite compound semiconductor research for photovoltaic applications and transfer of results into actual solar cell production,” *Solar Energy Materials and Solar Cells*, vol. 95, pp. 1509–1517, June 2011.
- [8] “Rekordwirkungsgrad von 20.4 % für flexible Solarzellen,” *Vakuum in Forschung und Praxis*, vol. 25, no. 2, 2013.
- [9] M. A. Green, K. Emery, Y. Hishikawa, W. Warta, and E. D. Dunlop, “Solar cell efficiency tables (version 40),” *Progress in Photovoltaics: Research and Applications*, vol. 20, pp. 606–614, 2012.
- [10] M. Contreras, L. Mansfield, B. Egaas, J. Li, M. Romero, S. Ag, E. Rudiger-voigt, and W. Mannstadt, “Improved Energy Conversion Efficiency in Wide-Bandgap Cu(In,Ga)Se<sub>2</sub> Solar Cells,” *Conference Paper of the 37th IEEE Photovoltaic Specialists Conference*, 2011.
- [11] M. R. Balboul, H. W. Schock, S. a. Fayak, a. A. El-Aal, J. H. Werner, and a. a. Ramadan, “Correlation of structure parameters of absorber layer with efficiency of Cu(In,Ga)Se<sub>2</sub> solar cell,” *Applied Physics A*, vol. 92, pp. 557–563, May 2008.
- [12] R. Klenk, J. Klaer, C. Köble, R. Mainz, S. Merdes, H. Rodriguez-Alvarez, R. Scheer, and H. Schock, “Development of CuInS<sub>2</sub>-based solar cells and modules,” *Solar Energy Materials and Solar Cells*, vol. 95, pp. 1441–1445, June 2011.
- [13] S. Merdes, R. Mainz, R. Klenk, M. C. Lux-steiner, and A. Meeder, “CdS/Cu (In,Ga)S<sub>2</sub> based solar cells with efficiencies reaching 12.9 % prepared by a rapid thermal process,” *Progress in Photovoltaics: Research and Applications*, 2012.

- [14] I. Hengel, A. Neisser, R. Klenk, and M. C. Lux-steiner, “Current transport in CuInS<sub>2</sub>:Ga/Cds/ZnO - solar cells,” *Thin Solid Films*, vol. 361-362, pp. 458–462, 2000.
- [15] U. Rau, “Tunneling-enhanced recombination in Cu(In,Ga)Se<sub>2</sub> heterojunction solar cells,” *Applied Physics Letters*, vol. 74, no. 1, p. 111, 1999.
- [16] J. E. Phillips, R. W. Birkmire, B. E. Mc Candless, P. V. Meyers, and W. N. Shafarmn, “Polycrystalline Heterojunction Solar Cells: A Device Perspective,” *Physica Status Solidi (b)*, vol. 194, no. 31, pp. 31–39, 1996.
- [17] R. Klenk, “Characterisation and modelling of chalcopyrite solar cells,” *Thin Solid Films*, vol. 387, pp. 135–140, May 2001.
- [18] M. Turcu, O. Pakma, and U. Rau, “Interdependence of absorber composition and recombination mechanism in Cu(In,Ga)(Se,S)<sub>2</sub> heterojunction solar cells,” *Applied Physics Letters*, vol. 80, no. 14, pp. 2598–2600, 2002.
- [19] K. Siemer, *Schichtwachstum und elektronische Defekteigenschaften von CuInS<sub>2</sub>-Absorberschichten aus dem sequentiellen Prozeß*. PhD thesis, FU Berlin, 2000.
- [20] M. Cwil, M. Igalson, P. Zabierowski, and S. Siebentritt, “Charge and doping distributions by capacitance profiling in Cu(In,Ga)Se<sub>2</sub> solar cells,” *Journal of Applied Physics*, vol. 103, 2008.
- [21] R. Herberholz, M. Igalson, and H. W. Schock, “Distinction between bulk and interface states in CuInSe<sub>2</sub>/CdS/ZnO by space charge spectroscopy,” *Journal of Applied Physics*, vol. 83, no. 1, pp. 318–325, 1998.
- [22] H. G. Grimm and A. Sommerfeld, “Über den Zusammenhang des Abschlusses der Elektronengruppen im Atom mit den chemischen Valenzzahlen,” *Zeitschrift für Physik*, vol. 36, no. 1, pp. 36–59, 1926.
- [23] L. Vegard, “Die Konstitution der Mischkristalle und die Raumfüllung der Atome,” *Zeitschrift für Physik*, vol. 5, no. 1, pp. 17–26, 1921.
- [24] G. L. Miller, D. V. Lang, and L. C. Kimerling, “Capacitance Transient Spectroscopy,” *Annual Review of Materials Science*, vol. 7, pp. 377–448, Aug. 1977.
- [25] H. Y. Ueng and H. L. Hwang, “Defect identification in undoped and phosphorus-doped CuInS<sub>2</sub> based on deviations from ideal chemical formula,” *Journal of Applied Physics*, vol. 62, no. 2, pp. 434–439, 1987.
- [26] S. Fiechter, Y. Tomm, K. Diesner, and T. Weiss, “Homogeneity Ranges, Defect Phases and Defect Formation Energies in A<sup>I</sup>B<sup>III</sup>C<sub>2</sub><sup>VI</sup> Chalcopyrites (A = Cu; B = Ga, In; C = S, Se),” *Japanese Journal of Applied Physics*, vol. 39, no. 1, pp. 123–126, 2000.
- [27] H. Y. Ueng and H. L. Hwang, “The Defect Structure of CuInS<sub>2</sub>. Part I: Intrinsic Defects,” *Journal of Physics and Chemistry of Solids*, vol. 50, no. 12, pp. 1297–1305, 1989.
- [28] H. Y. Ueng and H. L. Hwang, “The Defect Structure of CuInS<sub>2</sub>. Part II: Thermal Annealing Defects,” *Journal of Physics and Chemistry of Solids*, vol. 51, no. 1, pp. 1–10, 1990.

- [29] H. Neumann, "Vacancy Formation Enthalpies in  $A^I B^{III} C_2^{VI}$  Chalcopyrite Semiconductors," *Crystal Research and Technology*, vol. 18, no. 7, pp. 901–906, 1983.
- [30] R. Klenk, J. Klaer, R. Scheer, M. Lux-Steiner, I. Luck, N. Meyer, and U. Rühle, "Solar cells based on  $CuInS_2$  - an overview," *Thin Solid Films*, vol. 480-481, pp. 509–514, June 2005.
- [31] R. Klenk, T. Walter, D. Schmid, and H. W. Schock, "Growth Mechanisms and Diffusion in Multinary and Multilayer Chalcopyrite Thin Films," *Japanese Journal of Applied Physics*, vol. 32, no. 32-3, pp. 57–61, 1993.
- [32] H. J. Lewerenz and N. Dietz, "Defect identification in semiconductors by Brewster angle spectroscopy," *Journal of Applied Physics*, vol. 73, no. 10, pp. 4975–4987, 1993.
- [33] J. Kneisel, K. Siemer, I. Luck, and D. Bräunig, "Admittance spectroscopy of efficient  $CuInS_2$  thin film solar cells," *Journal of Applied Physics*, vol. 88, no. 9, pp. 5474–5481, 2000.
- [34] X. H. Liu, X. M. Dou, and M. Sugiyama, "Photoluminescence studies in  $CuInS_2$  thin films grown by sulfurization using ditertiarybutylsulfide," *Journal of Applied Physics*, vol. 112, no. 123521, pp. 1–9, 2012.
- [35] J. Binsma, L. Gilin, and J. Bloem, "Luminescence of  $CuInS_2$  - The Broad Band Emission and its Dependence on the Defect Chemistry," *Journal of Luminescence*, vol. 27, pp. 35–53, 1982.
- [36] J. Binsma, "Defect Chemistry of  $CuInS_2$ , Investigated by Electrical Measurements and Mössbauer Spectroscopy," *Journal of Physics and Chemistry of Solids*, vol. 44, no. 3, pp. 237–244, 1983.
- [37] M. Turcu, I. M. Kötschau, and U. Rau, "Composition dependence of defect energies and band alignments in the  $Cu(In_{1-x}Ga_x)(Se_{1-y}S_y)_2$  alloy system," *Journal of Applied Physics*, vol. 91, no. 3, pp. 1391–1399, 2002.
- [38] T. Walter, R. Herberholz, C. Müller, and H. W. Schock, "Determination of defect distributions from admittance measurements and application to  $Cu(In,Ga)Se_2$  based heterojunctions," *Journal of Applied Physics*, vol. 80, no. 8, pp. 4411–4420, 1996.
- [39] M. Igalson and H. W. Schock, "The metastable changes of the trap spectra of  $CuInSe_2$ -based photovoltaic devices," *Journal of Applied Physics*, vol. 80, no. 10, pp. 5765–5769, 1996.
- [40] U. Rau, M. Schmidt, A. Jasenek, G. Hanna, and H. W. Schock, "Electrical characterization of  $Cu(In,Ga)Se_2$  thin-film solar cells and the role of defects for the device performance," *Solar Energy Materials and Solar Cells*, vol. 67, pp. 137–143, 2001.
- [41] G. Hanna, A. Jasenek, U. Rau, and H. W. Schock, "Influence of the Ga-content on the bulk defect densities of  $Cu(In,Ga)Se_2$ ," *Thin Solid Films*, vol. 387, pp. 71–73, 2001.
- [42] A. Niemegeers, M. Burgelman, R. Herberholz, U. Rau, and D. Hariskos, "Model for Electronic Transport in  $Cu(In,Ga)Se_2$  Solar Cells," *Progress in Photovoltaics*:

- Research and Applications*, vol. 6, pp. 407–421, 1998.
- [43] M. Igalson, P. Zabierowski, A. Romeo, and L. Stolt, “Reverse-bias DLTS for investigation of the interface region in thin film solar cells,” *Opto-Electronics Review*, vol. 8, no. 4, pp. 346–349, 2000.
- [44] U. Rau, D. Braunger, R. Herberholz, and H. W. Schock, “Oxygenation and air-annealing effects on the electronic properties of Cu(In,Ga)Se<sub>2</sub> films and devices,” *Journal of Applied Physics*, vol. 86, no. 1, pp. 497–505, 1999.
- [45] J. T. Heath and J. D. Cohen, “Bulk and metastable defects in CuIn<sub>1-x</sub>Ga<sub>x</sub>Se<sub>2</sub> thin films using drive-level capacitance profiling,” *Journal of Applied Physics*, vol. 95, no. 3, pp. 1000–1010, 2004.
- [46] J. T. Heath, J. D. Cohen, and W. N. Shafarman, “Distinguishing metastable changes in bulk CIGS defect densities from interface effects,” *Thin Solid Films*, vol. 431-432, pp. 426–430, May 2003.
- [47] M. Igalson and M. Edoff, “Compensating donors in Cu(In,Ga)Se<sub>2</sub> absorbers of solar cells,” *Thin Solid Films*, vol. 480-481, pp. 322–326, 2005.
- [48] M. Igalson and A. Urbaniak, “Defect states in the CIGS solar cells by photocapacitance and deep level optical spectroscopy,” *Bulletin Of The Polish Academy Of Sciences Technical Sciences*, vol. 53, no. 2, pp. 157–161, 2005.
- [49] P. Zabierowski and M. Edoff, “Laplace-DLTS analysis of the minority carrier traps in the Cu(In,Ga)Se<sub>2</sub>-based solar cells,” *Thin Solid Films*, vol. 480-481, pp. 301–306, June 2005.
- [50] T. Eisenbarth, T. Unold, R. Caballero, C. A. Kaufmann, and H.-W. Schock, “Interpretation of admittance, capacitance-voltage, and current-voltage signatures in Cu(In,Ga)Se<sub>2</sub> thin film solar cells,” *Journal of Applied Physics*, vol. 107, no. 3, p. 034509, 2010.
- [51] U. Reislöhner, H. Metzner, and C. Ronning, “Hopping Conduction Observed in Thermal Admittance Spectroscopy,” *Physical Review Letters*, vol. 104, p. 226403, June 2010.
- [52] P. Zabierowski, K. Stankiewicz, A. Donmez, F. Couzinie-Devy, and N. Barreau, “Systematic study of the complex structure of N<sub>1</sub> Deep Level Transient Spectroscopy signal in Cu(In,Ga)Se<sub>2</sub> based heterojunctions,” *Thin Solid Films*, vol. 519, pp. 7485–7488, Aug. 2011.
- [53] I. Dirnstorfer, D. M. Hofmann, D. Meister, B. K. Meyer, W. Riedl, and F. Karg, “Postgrowth thermal treatment of CuIn(Ga)Se<sub>2</sub>: Characterization of doping levels in In-rich thin films,” *Journal of Applied Physics*, vol. 85, no. 3, pp. 1423–1428, 1999.
- [54] I. Dirnstorfer, W. Burkhardt, W. Kriegseis, I. Österreicher, H. Alves, D. Hofmann, O. Ka, A. Polity, B. K. Meyer, and D. Braunger, “Annealing studies on CuIn(Ga)Se<sub>2</sub>: the influence of gallium,” *Thin Solid Films*, vol. 361-362, pp. 400–405, 2000.
- [55] J. H. Schön, V. Alberts, and E. Bucher, “Control and passivation of V<sub>Se</sub> defect lev-

- els in H<sub>2</sub>Se-selenized CuInSe<sub>2</sub> thin films,” *Semiconductor Science and Technology*, vol. 14, pp. 657–659, 1999.
- [56] S. Siebentritt and U. Rau, *Wide-Gap Chalcopyrites*. Springer, 2006.
- [57] H.-W. Schock, U. Rau, T. Dullweber, G. Hanna, M. Balboul, T. Margorian-Friedlemeier, A. Jasenek, I. Kötschau, H. Kerber, and H. Wiesner, “High Efficiency, High Voltage Solar Cells by Band Gap and Defect Engineering in Cu(In,Ga)(S,Se)<sub>2</sub> Chalcopyrite Semiconductors,” *Proceedings of the 16th European Photovoltaic Solar Energy Conference*, pp. 301–305, 2000.
- [58] J. Malmström, M. Wennerberg, M. Bodegård, and L. Stolt, “Influence of Ga on the current transport in Cu(In,Ga)Se<sub>2</sub> thin film solar cells,” *Proceedings of the 17th European Photovoltaic Solar Energy Conference*, pp. 1–4, 2001.
- [59] R. Herberholz, V. Nadenau, U. Rühle, C. Köble, H. W. Schock, and B. Dimmler, “Prospects of wide-gap chalcopyrites for thin film photovoltaic modules,” *Solar Energy Materials and Solar Cells*, vol. 49, pp. 227–237, 1997.
- [60] S. Lany and A. Zunger, “Intrinsic DX Centers in Ternary Chalcopyrite Semiconductors,” *Physical Review Letters*, vol. 100, p. 016401, Jan. 2008.
- [61] V. Nadenau, U. Rau, A. Jasenek, and H. W. Schock, “Electronic properties of CuGaSe<sub>2</sub>-based heterojunction solar cells. Part I. Transport analysis,” *Journal of Applied Physics*, vol. 87, no. 1, pp. 584–593, 2000.
- [62] J. Reiß, Malmström J., A. Werner, I. Henge, R. Klenk, and M. C. Lux-Steiner, “Current Transport in CuInS<sub>2</sub> Solar Cells Depending on Absorber Preparation,” *MRS Proceedings*, vol. 668, no. H9.4, 2001.
- [63] S. Merdes, R. Saez-Araoz, A. Ennaoui, J. Klaer, M. C. Lux-Steiner, and R. Klenk, “Recombination mechanisms in highly efficient thin film Zn(S,O)/Cu(In,Ga)S<sub>2</sub> based solar cells,” *Applied Physics Letters*, vol. 95, no. 213502, 2009.
- [64] Y. Hashimoto, K. Takeuchi, and K. Ito, “Band alignment at CdS/CuInS<sub>2</sub> heterojunction,” *Applied Physics Letters*, vol. 67, no. 7, pp. 980–982, 1995.
- [65] L. Weinhardt, O. Fuchs, D. Groß, G. Storch, E. Umbach, N. G. Dhare, A. A. Kadam, S. S. Kulkarni, and C. Heske, “Band alignment at the CdS/Cu(In,Ga)S<sub>2</sub> interface in thin-film solar cells,” *Applied Physics Letters*, vol. 86, no. 062109, 2005.
- [66] B. E. Johnson, *The Role of Cd and Ga in the Cu(In,Ga)S<sub>2</sub>/CdS Heterojunction Studied with X-Ray Spectroscopic Methods*. PhD thesis, Helmholtz-Zentrum Berlin, 2010.
- [67] S. Merdes, B. Johnson, R. Sáez-Araoz, A. Ennaoui, J. Klaer, I. Lauermann, R. Mainz, A. Meeder, and R. Klenk, “Current Transport in Cu(In,Ga)S<sub>2</sub> Based Solar Cells with High Open Circuit Voltage - Bulk vs. Interface,” *Mater. Res. Soc. Symp. Proc.*, vol. 1165, no. 1165-M05-15, 2009.
- [68] I. Riedel, J. Riediger, J. Ohland, J. Keller, M. Knipper, J. Parisi, R. Mainz, and S. Merdes, “Photoelectric characterization of Cu(In,Ga)S<sub>2</sub> solar cells obtained from rapid thermal processing at different temperatures,” *Solar Energy Materials and Solar Cells*, vol. 95, pp. 270–273, Jan. 2011.

- [69] P. Blood and J. Orton, *The Electrical Characterization of Semiconductors: Majority Carriers and Electron States*. Academic Press Inc., 1992.
- [70] L. Kimerling, “Influence of deep traps on the measurement of free-carrier distributions in semiconductors by junction capacitance techniques,” *Journal of Applied Physics*, vol. 45, no. 4, pp. 1839–1845, 1974.
- [71] A. Goetzberger, J. Knobloch, and B. Voss, *Crystalline Silicon Solar Cells*. Wiley, 1998.
- [72] D. L. Losee, “Admittance spectroscopy of impurity levels in Schottky barriers,” *Journal of Applied Physics*, vol. 46, no. 5, pp. 2204–2214, 1975.
- [73] T. Eisenbarth, *Identifikation von Defekten und Metastabilitäten in Cu(In, Ga)Se<sub>2</sub>-Dünnschichtsolarzellen*. PhD thesis, FU Berlin, 2010.
- [74] W. Meyer and H. Neldel, “No Title,” *Zeitschrift für technische Physik*, vol. 12, no. 588, 1937.
- [75] A. Yelon, B. Movaghar, and H. M. Branz, “Origin and consequences of the compensation (Meyer-Neldel) law,” *Physical review. B*, vol. 46, pp. 12244–12250, Nov. 1992.
- [76] Z. Djebbour, A. Darga, A. Migandubois, D. Mencaraglia, N. Naghavi, J. Guillemoles, and D. Lincot, “Admittance spectroscopy of cadmium free CIGS solar cells heterointerfaces,” *Thin Solid Films*, vol. 511–512, pp. 320–324, July 2006.
- [77] A. Krysztopa, M. Igalson, Y. Aida, J. K. Larsen, L. Gutay, and S. Siebentritt, “Defect levels in the epitaxial and polycrystalline CuGaSe<sub>2</sub> by photocurrent and capacitance methods,” *Journal of Applied Physics*, vol. 110, no. 103711, 2011.
- [78] K. L. Narasimhan and B. Arora, “The capture cross-section and the Meyer-Neldel rule in III-V compound semiconductors,” *Solid State Communications*, vol. 55, no. 7, pp. 615–617, 1985.
- [79] F. R. Shapiro and J. R. Tuttle, “The Meyer-Neldel Rule in Emission Rates from Defects in Copper Indium Diselenide,” *Solid State Communications*, vol. 87, no. 3, pp. 199–202, 1993.
- [80] S. S. Hegedus and W. N. Shafarman, “Thin-Film Solar Cells: Device Measurements and Analysis,” *Progress in Photovoltaics: Research and Applications*, vol. 12, pp. 155–176, Mar. 2004.
- [81] D. Abou-Ras, R. Caballero, C.-H. Fischer, C. A. Kaufmann, I. Lauermann, R. Mainz, H. Mönig, A. Schöpke, C. Stephan, C. Streeck, S. Schorr, A. Eicke, M. Döbeli, B. Gade, J. Hinrichs, T. Nunnery, H. Dijkstra, V. Hoffmann, D. Klemm, V. Efimova, A. Bergmaier, G. Dollinger, T. Wirth, W. Unger, A. A. Rockett, A. Perez-Rodriguez, J. Alvarez-Garcia, V. Izquierdo-Roca, T. Schmid, P.-P. Choi, M. Müller, F. Bertram, J. Christen, H. Khatiri, R. W. Collins, S. Marsillac, and I. Kötschau, “Comprehensive Comparison of Various Techniques for the Analysis of Elemental Distributions in Thin Films,” *Microscopy and Microanalysis*, vol. 17, pp. 728–51, Oct. 2011.
- [82] U. Rau and H. W. Schock, “Electronic properties of Cu(In,Ga)Se<sub>2</sub> heterojunction

- solar cells - recent achievements, current understanding, and future challenges,” *Applied Physics A: Materials Science & Processing*, vol. 69, pp. 131–147, 1999.
- [83] M. Saad and A. Kassis, “Effect of interface recombination on solar cell parameters,” *Solar Energy Materials and Solar Cells*, vol. 79, pp. 507–517, Sept. 2003.
- [84] S. Merdes, R. Mainz, J. Klaer, A. Meeder, H. Rodriguez-Alvarez, H. Schock, M. Lux-Steiner, and R. Klenk, “12.6 % efficient CdS/Cu(In,Ga)S<sub>2</sub>-based solar cell with an open circuit voltage of 879 mV prepared by a rapid thermal process,” *Solar Energy Materials and Solar Cells*, vol. 95, pp. 864–869, Mar. 2011.
- [85] K. Siemer, J. Klaer, I. Luck, J. Bruns, R. Klenk, and D. Bräunig, “Efficient CuInS<sub>2</sub> solar cells from a rapid thermal process (RTP),” *Solar Energy Materials and Solar Cells*, vol. 67, pp. 159–166, 2001.
- [86] M. Bär, W. Bohne, J. Röhrich, E. Strub, S. Lindner, M. C. Lux-Steiner, C.-H. Fischer, T. P. Niesen, and F. Karg, “Determination of the band gap depth profile of the pentenary Cu(In<sub>1-x</sub>Ga<sub>x</sub>)(S<sub>y</sub>Se<sub>1-y</sub>)<sub>2</sub> chalcopyrite from its composition gradient,” *Journal of Applied Physics*, vol. 96, no. 7, pp. 3857–3860, 2004.
- [87] J. Song, S. S. Li, C. H. Huang, O. D. Crisalle, and T. J. Anderson, “Device Modeling and Simulation of the Performance of Cu(In<sub>1-x</sub>,Ga<sub>x</sub>)Se<sub>2</sub> Solar Cells,” *Solid State Electronics*, vol. 48, no. 1, pp. 73–79, 2004.
- [88] T. Dullweber, G. Hanna, W. Shams-Kolahi, A. Schwartzlander, M. A. Contreras, R. Noufi, and H. Schock, “Study of the effect of gallium grading in Cu(In,Ga)Se<sub>2</sub>,” *Thin Solid Films*, vol. 361-362, pp. 478–481, 2000.
- [89] J. R. Sites, J. Granata, and J. Hiltner, “Losses due to polycrystallinity in thin-film solar cells,” *Solar Energy Materials and Solar Cells*, vol. 55, pp. 43–50, July 1998.
- [90] L. Zhang, Q. He, W.-L. Jiang, F.-F. Liu, C.-J. Li, and Y. Sun, “Effects of substrate temperature on the structural and electrical properties of Cu(In,Ga)Se<sub>2</sub> thin films,” *Solar Energy Materials & Solar Cells*, vol. 93, pp. 114–118, Jan. 2009.
- [91] R. Scheer, “Activation energy of heterojunction diode currents in the limit of interface recombination,” *Journal of Applied Physics*, vol. 105, no. 104505, 2009.
- [92] P. K. Johnson, J. T. Heath, J. D. Cohen, K. Ramanathan, and J. R. Sites, “A Comparative Study of Defect States in Evaporated and Selenized CIGS(S) Solar Cells,” *Progress in Photovoltaics: Research and Applications*, vol. 13, pp. 1–8, Nov. 2005.
- [93] I. L. Repins, B. J. Stanbery, D. L. Young, S. S. Li, W. K. Metzger, C. L. Perkins, W. N. Shafarman, M. E. Beck, L. Chen, V. K. Kapur, D. Tarrant, M. D. Gonzalez, D. G. Jensen, T. J. Anderson, X. Wang, L. L. Kerr, B. Keyes, S. Asher, A. Delahoy, and B. Von Roedern, “Comparison of Device Performance and Measured Transport Parameters in Widely-Varying Cu(In,Ga)(Se,S) Solar Cells,” *Progress in Photovoltaics: Research and Applications*, vol. 14, pp. 25–43, Jan. 2006.
- [94] D. Cahen and R. Noufi, “Defect chemical explanation for the effect of air anneal on CdS/CuInSe<sub>2</sub> solar cell performance,” *Applied Physics Letters*, vol. 54, no. 6, pp. 558–560, 1989.

## Bibliography

- [95] M. S. Hammer, N. Neugebohrn, J. Riediger, J. Neerken, J. Ohland, I. Riedel, O. Kiowski, and W. Wischmann, “Defect-related electronic metastabilities in chalcopyrite compounds,” *Physica B: Condensed Matter, SACPM 2013 proceedings (submitted)*, 2013.
- [96] K. Töpfer, J. Bruns, R. Scheer, M. Weber, A. Weidinger, and D. Bräunig, “Photoluminescence of CuInS<sub>2</sub> thin films and solar cells modified by postdeposition treatments,” *Applied Physics Letters*, vol. 71, no. 4, pp. 482–484, 1997.

# Lebenslauf

## Julia Riediger

geboren am 02.04.1983 in Papenburg (Deutschland)

### Promotion und berufliche Tätigkeiten

---

- |                           |  |
|---------------------------|--|
| Januar 2009 – August 2013 | Promotion,<br>Arbeitsgruppe <i>Energie- und Halbleiterforschung</i> , Carl-von-Ossietzky Universität Oldenburg                             |
| Januar 2009 – Januar 2013 | Wissenschaftliche Mitarbeiterin in der<br>Arbeitsgruppe <i>Energie- und Halbleiterforschung</i> , Carl-von-Ossietzky Universität Oldenburg |

### Studium und Schulausbildung

---

- |                             |   |
|-----------------------------|---|
| Oktober 2002 – Oktober 2008 | Studium der Physik<br>Carl-von-Ossietzky Universität Oldenburg<br>Abschluss: Diplom       |
| Oktober 2007 – Oktober 2008 | Diplomarbeit<br>Thema: <i>Dosimetrische Charakterisierung eines Multileaf Kollimators</i> |
| April 2002                  | Abitur<br>Hümmling-Gymnasium, Sögel   |



# Acknowledgment

This thesis was realized with financial support of

- ... the Federal Ministry for the Environment, Nature Conservation and Nuclear Safety (BMU) on the basis of a resolution passed by the German Bundestag as a part of the projects HT-CIGS (support code: 0327589H) and KD-CIS (support code: 0327589A).
- ... the EWE AG (Oldenburg, Germany) due to funding the EWE Nachwuchsgruppe.

I would like to give sincere thanks to those persons who supported and accompanied me throughout my time as a PhD student at the Carl von Ossietzky Universität Oldenburg. Special thanks go to...

- ... Prof. Dr. Jürgen Parisi for the chance to prepare this thesis under his leadership in the working group Energie- und Halbleiterforschung (EHF) and for meeting me with a friendly and uncomplicated manner.
- ... The Helmholtz-Zentrum Berlin and the Soltecture GmbH for providing the samples and for the fruitful cooperation within the framework of the KD-CIS and the HT-CIGS project, especially to Roland Mainz und Alexander Meeder for technical discussions.
- ... Dr. Ingo Riedel for the supervision of my thesis, for encouragement and inspiring ideas. Even in very stressful times he managed to find some time to listen, to focus on my problems and to give me concrete advice.
- ... Maria Hammer for additional supervision and support as well as for correcting proofs. Not only her expertise and strategic competence but also her optimistic spirit pushed me on especially during the very important last months.
- ... Prof. Dr. Małgorzata Igalson for her cooperativeness and the evaluation of this thesis. I would also like to thank her and her team in Warsaw for their hospitality and open communication, for sharing their knowledge and time.
- ... Dr. Matthias Schmidt for the invitation to Leipzig and the friendly contact. Due to his great enthusiasm for defect spectroscopy and his valuable recommendations I won lots of new angles of view and motivation for my work.
- ... Janet Neerken for her help with experimental setups and measurement control and for good ideas regarding technical implementations. She often helped me to find forward-looking strategies not only for experimental work but also for general work organization. I am very grateful to her for encouragement in demanding situations, for moral support and for her careful and constructive proofreading.

## *Bibliography*

- ... Jörg Ohland for the patient support in technical questions, for his humor and empathy. Thanks to him also for sending me home in the evenings every now and then.
- ... Holger Koch, Matthias Macke, Ulf Mikolajczak, Dirk Otteken and Thomas Madena for technical support and providing their know-how regarding experimental implementations.
- ... all the former and present members of the EHF LCP (formerly DSPV) working group for time, discussions, professional help and for creating a great working atmosphere. Special thanks go to my office mates Jan Keller, Anton Werth, Robin Knecht and Michael Richter for the nice time with distracting jokes and stories.
- ... Jan Keller for taking his time for performing and analyzing the EDX measurements, the support in performing and analyzing the IVT-measurements and the discussions on all the other questions that I could ask him.
- ... Sven Burdorf und Sarah Falke: From the first to the last day of my time at the university they shared news, sorrows and humor with me. Going for lunch with best friends almost every day is a luxury that I will gladly remember.
- ... "The Girls" including Sarah, Doro, Jutta, Sabine and Mareike for all the Wednesday evenings where we tried our best not to discuss the principles of physics but to focus on other topics. Those evenings with them were a great medicine to forget about experimental problems and confusing data.
- ... My dear parents Uli and Gabi and my dear brother Mathias who believed in my success and strengthened me so continuously during all the time.
- ... Special thanks to Marco for his tolerance, optimism and patience. He encouraged me day after day and made me feel secure.

# Erklärung

Hiermit erkläre ich, dass ich die vorliegende Dissertation selbstständig verfasst und nur die angegebenen Hilfsmittel benutzt habe. Die Arbeit wurde weder in ihrer Gesamtheit noch in Teilen einer anderen wissenschaftlichen Hochschule zur Begutachtung in einem Promotionsverfahren vorgelegt.

Die in Abschnitt 6.1.1 gezeigten EDX Linienscans wurden von Dr. Jan Keller gemessen.

---

Unterschrift, Ort und Datum



# List of publications

- [1] I. Riedel, J. Riediger, J. Ohland, J. Keller, M. Knipper, J. Parisi, R. Mainz, S. Merdes, "Photoelectric characterization of Cu(In,Ga)S<sub>2</sub> solar cells obtained from rapid thermal processing at different temperatures" *Solar Energy Materials and Solar Cells* vol. 95, pp. 270-273, 2011